

# Integrated circuits for wearable systems based on flexible electronics

***Citation for published version (APA):***

Zulqarnain, M. (2020). *Integrated circuits for wearable systems based on flexible electronics*. [Phd Thesis 1 (Research TU/e / Graduation TU/e), Electrical Engineering]. Technische Universiteit Eindhoven.

***Document status and date:***

Published: 02/12/2020

***Document Version:***

Publisher's PDF, also known as Version of Record (includes final page, issue and volume numbers)

***Please check the document version of this publication:***

- A submitted manuscript is the version of the article upon submission and before peer-review. There can be important differences between the submitted version and the official published version of record. People interested in the research are advised to contact the author for the final version of the publication, or visit the DOI to the publisher's website.
- The final author version and the galley proof are versions of the publication after peer review.
- The final published version features the final layout of the paper including the volume, issue and page numbers.

[Link to publication](#)

***General rights***

Copyright and moral rights for the publications made accessible in the public portal are retained by the authors and/or other copyright owners and it is a condition of accessing publications that users recognise and abide by the legal requirements associated with these rights.

- Users may download and print one copy of any publication from the public portal for the purpose of private study or research.
- You may not further distribute the material or use it for any profit-making activity or commercial gain
- You may freely distribute the URL identifying the publication in the public portal.

If the publication is distributed under the terms of Article 25fa of the Dutch Copyright Act, indicated by the "Taverne" license above, please follow below link for the End User Agreement:

[www.tue.nl/taverne](http://www.tue.nl/taverne)

***Take down policy***

If you believe that this document breaches copyright please contact us at:

[openaccess@tue.nl](mailto:openaccess@tue.nl)

providing details and we will investigate your claim.

# Integrated Circuits for Wearable Systems based on Flexible Electronics

Mohammad Zulqarnain

The work in this thesis was carried out in the Integrated Circuits (IC) group of the Department of Electrical Engineering at the Eindhoven University of Technology in collaboration with imec-NL/Holst Centre under the framework of the project “Integrated Circuits for Conformal Wearable Systems”.

Integrated Circuits for Wearable Systems based on Flexible Electronics  
by Mohammad Zulqarnain.

Eindhoven: Technische Universiteit Eindhoven, 2020. Proefschrift.

This thesis was typeset using  $\text{\LaTeX}$ . Template adapted from Version 1.0  
by Joos Buijs, Eindhoven, 2014.

Front cover: Photo by Solen Feyissa on Unsplash including main picture  
by Mohammad Zulqarnain

Back cover: Photo by Ranurte on Unsplash

A catalogue record is available from the Eindhoven University of Technology  
Library

ISBN: 978-90-386-5163-7

Copyright © 2020 by Mohammad Zulqarnain.

All Rights Reserved.

Reproduction in whole or in part is prohibited  
without the written consent of the copyright owner.

# Integrated Circuits for Wearable Systems based on Flexible Electronics

PROEFSCHRIFT

ter verkrijging van de graad van doctor aan de Technische  
Universiteit Eindhoven, op gezag van de rector magnificus  
prof.dr.ir. F.P.T. Baaijens, voor een commissie aangewezen door het  
College voor Promoties, in het openbaar te verdedigen op woensdag  
2 december 2020 om 13:30 uur

door

Mohammad Zulqarnain

geboren te Aligarh, India

Dit proefschrift is goedgekeurd door de promotoren en de samenstelling van de promotiecommissie is als volgt:

voorzitter:	prof.dr.ir. S.M. Heemstra de Groot
1 <sup>e</sup> promotor:	prof.dr.ir. E. Cantatore
2 <sup>e</sup> promotor:	dr. ir. P.J.A. Harpe
co-promotor:	dr. M. Fattori
leden:	prof.dr.ir. J. Genoe (KU Leuven)
	prof.dr.ir. W. Dehaene (KU Leuven)
	prof.dr.ir. M. Mischi
adviseur:	dr. S. Stanzione (imec)

Het onderzoek of ontwerp dat in dit proefschrift wordt beschreven is uitgevoerd in overeenstemming met de TU/e Gedragscode Wetenschapsbeoefening.

## Declaration concerning the TU/e Code of Scientific Conduct for the PhD thesis

I have read the TU/e Code of Scientific Conduct<sup>i</sup>.

I hereby declare that my PhD thesis has been carried out in accordance with the rules of the TU/e Code of Scientific Conduct

Date

7<sup>th</sup> October, 2020.....

Name

Mohammad Zulqarnain.....

Signature

*Mohammad Zulqarnain*.....

<sup>i</sup> See: <http://www.tue.nl/en/university/about-the-university/integrity/scientific-integrity/>

The Netherlands Code of Conduct for Academic Practice of the VSNU can be found here also.

More information about scientific integrity is published on the websites of TU/e and VSNU



*To my beloved parents*



*“Hum to mā.il-ba-karam haiñ koī saa.il hī nahīñ  
Raah dikhlā.eñ kise rah-rav-e-manzil hī nahīñ  
Koī qābil ho to hum shān-e-ka.ī dete haiñ  
Dhūñdne vāloñ ko duniyā bhī na.ī dete haiñ”  
— Allama Iqbal*

*[Behold, my hands are full of gifts, but no one comes seeking here,  
And whom shall I show the right path, when there is no traveller,  
On him who merits well, I bestow the brightest diadem,  
And those who truly come questing, I unveil even a new world to them.]*



# Contents

<b>1</b>	<b>Introduction</b>	<b>1</b>
1.1	Introduction . . . . .	2
1.1.1	Flexible electronic technologies . . . . .	3
1.1.2	Design challenges . . . . .	5
1.1.3	Applications . . . . .	7
1.1.4	State-of-the-art flexible wearable biomedical sensors . . . . .	7
1.2	Problem statement . . . . .	9
1.3	Aim of the thesis . . . . .	10
1.4	Scope of the thesis . . . . .	11
1.5	Original contributions . . . . .	11
1.6	Outline of the thesis . . . . .	13
<b>2</b>	<b>a-IGZO TFT Technology</b>	<b>21</b>
2.1	Introduction . . . . .	22
2.2	Device stack . . . . .	22
2.3	Etch stop layer TFT technology . . . . .	22
2.4	Dual-gate self aligned TFT technology . . . . .	24
2.5	Device channel current modelling . . . . .	25
2.5.1	ESL channel current modelling . . . . .	25
2.5.2	DUGA channel current modelling . . . . .	28

2.6	Device noise modelling . . . . .	29
2.7	Conclusions . . . . .	30
<b>3</b>	<b>Design Trade-offs in a-IGZO TFT based Bio-signal Front-ends</b>	<b>33</b>
3.1	Introduction . . . . .	34
3.2	Design constraints for bio-signal front-ends . . . . .	35
3.3	Bio-signal front-end architectures . . . . .	37
3.4	Limitations of a-IGZO TFT technology . . . . .	41
3.5	Bio-signal front-ends based on a-IGZO TFTs . . . . .	43
3.5.1	FE-I and FE-II . . . . .	44
3.5.2	FE-III . . . . .	46
3.5.3	FE-IV . . . . .	46
3.6	Measurement results . . . . .	47
3.7	Conclusions . . . . .	54
<b>4</b>	<b>A Heart-Rate Measurement Interface on a Flexible Foil</b>	<b>59</b>
4.1	Introduction . . . . .	60
4.2	Single slope reset integrator . . . . .	62
4.2.1	Principle of operation . . . . .	62
4.2.2	Circuit characterization . . . . .	65
4.3	Heart-rate measurement interface . . . . .	67
4.3.1	System architecture . . . . .	67
4.3.2	Circuit design . . . . .	69
4.3.3	Experimental results . . . . .	72
4.4	Time based ECG interface . . . . .	78
4.4.1	Improved system architecture . . . . .	78
4.4.2	Principle of operation . . . . .	79
4.4.3	Simulation results . . . . .	81
4.5	Conclusions . . . . .	86

<b>5</b>	<b>A Flexible ECG Patch Compatible with NFC RF Communication</b>	<b>91</b>
5.1	Introduction . . . . .	92
5.2	System architecture . . . . .	95
5.3	Circuit design . . . . .	96
5.4	Measurement results . . . . .	100
5.4.1	Electrical characterization . . . . .	100
5.4.2	<i>In-vivo</i> characterization . . . . .	103
5.5	Conclusions . . . . .	106
<b>6</b>	<b>A Multichannel EOG Acquisition System based on Flexible TFTs and CMOS Technologies</b>	<b>113</b>
6.1	Introduction . . . . .	114
6.2	System architecture . . . . .	115
6.2.1	Hybrid high pass filter . . . . .	118
6.2.2	Frontend on flexible foil . . . . .	121
6.2.3	Silicon backend . . . . .	122
6.3	Measurement results . . . . .	127
6.3.1	Preamplifier chain characterization . . . . .	128
6.3.2	Full system characterization . . . . .	130
6.4	Conclusions . . . . .	132
<b>7</b>	<b>A Digitally Assisted Tunable High Pass Filter</b>	<b>137</b>
7.1	Introduction . . . . .	138
7.2	System architecture . . . . .	138
7.3	Circuit principle . . . . .	139
7.4	Simulation results . . . . .	142
7.5	Conclusions . . . . .	145
<b>8</b>	<b>Conclusions</b>	<b>149</b>
8.1	Conclusions . . . . .	150
8.2	Future work . . . . .	152



# List of Figures

2.1	Cross section of an a-IGZO TFT based on ESL flow. . . . .	23
2.2	Cross section of an a-IGZO TFT based on DUGA flow. . . . .	25
2.3	Schematic device model including a reverse biased Schottky-gated diode. . . . .	27
2.4	Measured transfer characteristics of ESL TFT (in hysteresis mode) compared to model simulations. . . . .	27
2.5	Measured transfer characteristics of DUGA TFT compared to model simulations when $V_{BG}$ is varied between -5 V to 5 V. Note that the points under $10^{-10}$ A are dominated by noise [8]. . . . .	29
3.1	Bio-signal front-ends implemented with (a) an open loop amplifier (b) an amplifier in capacitive feedback (c) an amplifier in capacitive feedback with additional impedance-boosting positive feedback loop. . . . .	38
3.2	Architectural schematics of the presented front-ends with structural details of the core amplifiers. . . . .	45
3.3	Foil micrograph of the fabricated front-ends (a) FE-I, (b) FE-II, (c) FE-III and (d) FE-IV. . . . .	48
3.4	Frequency response of the amplifiers (a) FE-I, (b) FE-II, (c) FE-III and (d) FE-IV. . . . .	48

3.5	Input referred noise density of the different front-ends (a) FE-I, (b) FE-II, (c) FE-III and (d) FE-IV. . . . .	49
3.6	Input impedance of the different front-ends (a) FE-I, (b) FE-II, (c) FE-III and (d) FE-IV. . . . .	51
3.7	Performance comparison of the presented front-ends. . . . .	52
4.1	General bio-signal acquisition system architecture. . . . .	60
4.2	(a) Architecture of the single slope reset integrator, (b) Circuit schematic of the single slope reset integrator, (c) Functionality of the reset integrator in terms of signal processing operations, (d) Principle of operation. . . . .	62
4.3	Comparison of sinc LPF response with RC LPF response. . . . .	64
4.4	Micrograph of the single slope reset integrator on foil. . . . .	66
4.5	DC transfer characteristics. . . . .	67
4.6	Residual error in measured $T_{out}$ with respect to linear fit. . . . .	67
4.7	Variation of gain with $V_{ref}$ . . . . .	68
4.8	Measured output jitter. . . . .	68
4.9	General system architecture. . . . .	69
4.10	Principle of operation. . . . .	70
4.11	Micrograph of the preamplifier and reset Integrator on foil. . . . .	73
4.12	Measured preamplifier frequency response and input-referred noise. . . . .	74
4.13	Measured CMRR of the preamplifier. . . . .	74
4.14	Measured input impedance of the preamplifier. . . . .	75
4.15	Measured frequency response of the full chain. . . . .	75
4.16	Measured output jitter in absence of an input signal. . . . .	76
4.17	Response of the measurement interface to an ECG signal provided by a signal generator. . . . .	76
4.18	Reconstructed signal from PWM waveform showing heartbeat from <i>in-vivo</i> measurement. . . . .	77

4.19 System architecture of the improved version of the system shown in Figure 4.9. . . . .	79
4.20 Schematics of (a) the preamplifier, (b) the reset integrator, (c) pseudo CMOS inverter and (d) working principle of the reset integrator. . .	79
4.21 Principle of system level CDS. . . . .	80
4.22 Simulated frequency response of the preamplifier. . . . .	82
4.23 Simulated noise spectrum of the proposed system. . . . .	82
4.24 Simulated DC transfer curve of the inverter with cascading three pseudo-CMOS inverters. . . . .	83
4.25 Simulated response of the full system to an ECG source signal. . . .	83
5.1 Representative application scenario of the presented ECG patch. . .	93
5.2 System architecture. (a) Conventional bio-potential acquisition system, (b) System-level diagram of the presented ECG acquisition system, (c) Detailed architecture of the presented system. . . . .	94
5.3 Circuit schematics and working principle. (a) Schematic of each of the two cascaded diode-load amplifiers in the preamplifier, (b) Reset integrator, (c) Reset integrator working principle. . . . .	99
5.4 Timing diagram of the clock phases. . . . .	101
5.5 Measured frequency response and input-referred noise of the cascaded preamplifier. . . . .	102
5.6 Measured transfer function of the full analogue chain (from input to output PWM). . . . .	102
5.7 (Top panel) <i>In-vivo</i> ECG measured signal reconstructed from the output PWM, (Bottom panel) <i>In-vivo</i> ECG measured signal reconstructed from Manchester encoded output. . . . .	103
5.8 Manchester encoded output corresponding to three samples of the <i>in-vivo</i> measurement and a zoom-in of the Manchester encoding of the output bits. . . . .	104
5.9 Foil micrograph of the presented system. . . . .	105

6.1	Representative integration of the flexible hybrid system. . . . .	116
6.2	System architecture of the flexible hybrid system. . . . .	117
6.3	Architecture of the flexible hybrid HPF. . . . .	120
6.4	Circuit schematic of analogue frontend (a) Schematic of the diode-connected load amplifier, (b) Reset integrator, (c) Clock boosting circuit. . . . .	121
6.5	Timing diagram of the frontend on flexible foil. . . . .	123
6.6	Circuit schematic of the current reference. . . . .	123
6.7	(a) Circuit schematic of the I/V conversion (single ended version shown for illustration), (b) Circuit schematic of the ring oscillator. . .	125
6.8	Circuit schematics of the PWM generator, counter and serializer. . .	126
6.9	Timing diagram for the PWM generator block. . . . .	127
6.10	Timing diagram for the Silicon backend. . . . .	128
6.11	Micrograph of the full system including frontend on flexible foil and Silicon backend. . . . .	129
6.12	Measured frequency response and input-referred noise of the preamplifier chain ( $A_{1-3}$ ). . . . .	129
6.13	Measured transfer function of the full system. . . . .	131
6.14	Measured input referred noise of the full system. . . . .	131
6.15	Measured crosstalk of the full system. . . . .	132
7.1	(a) General system architecture and (b) General high pass filter response. . . . .	139
7.2	Circuit schematic of the proposed system. . . . .	140
7.3	Waveforms at different nodes of the system depicting operation of the system. To show more clearly how the system works, an 8 bit counter and DAC are used to generate this figure. . . . .	141
7.4	The effect of threshold voltage variation on the relative error in $f_p$ . .	143
7.5	The effect of $V_{DD}$ variation on the relative error in $f_p$ . . . . .	143
7.6	The effect of $f_{ref}$ variation on $f_p$ and the relative error in $f_p$ . . . .	144

- 7.7 The effect of  $A_{ref}/A_p$  ratio variation on  $f_p$  and the relative error in  $f_p$ . 145
- 7.8 The effect of  $A_p$  variation in  $f_p$  (keeping the  $A_{ref}/A_p$  ratio constant). 145



# List of Tables

3.1	Relevant design parameters of the presented front-ends. . . . .	47
3.2	Performance comparison of the presented front-ends with the state-of-the-art. . . . .	55
4.1	Circuit parameters of the single slope reset integrator . . . . .	66
4.2	Optimized design parameters of the system shown in Figure 4.9 . . .	72
4.3	Comparison to the state-of-the-art . . . . .	78
4.4	Comparison to prior literature . . . . .	85
5.1	Specifications of ECG recording systems as dictated by the ANSI AAMI standard . . . . .	96
5.2	Comparison with the state-of-the-art . . . . .	107
6.1	Comparison with the state-of-the-art . . . . .	134



# Chapter 1

## Introduction

## 1.1 Introduction

The electronics field has witnessed a transformation phase in the recent years, due to the rapid rise of wearables and ubiquitous sensors, thanks to the advent of the Internet of Things (IoT). There are applications which do not suit traditional electronics such as displays, imagers, photovoltaic cells, NFC tags, wearable sensors for biomedical signals monitoring etc.

Indeed, applications that require a large surface to be covered with electronics are difficult or costly to achieve with conventional Silicon-based Integrated Circuits (ICs). However, advancements in the technology of thin-film transistors (TFTs) have paved the way to fabricate devices over large areas and have opened the possibility, thanks to a low process temperature budget, to use plastic foils as flexible substrates, enabling what is called "flexible and large area electronics". This type of devices not only result in electronics distributed over a large area, but also leads to lower cost per unit area compared to conventional ICs. The inherent flexible nature of the substrates in these technologies can be leveraged in applications requiring conformability, bendability, foldability and stretchability. A specific category of applications that can strongly benefit from flexible electronics is the domain of flexible and comfortable wearable devices for wellness and healthcare monitoring.

The dimensions of the transistors in flexible technologies are in micrometre regime, that leads to low cost solutions. Although these devices do not perform on par with conventional Silicon technologies, these devices are useful in the applications where high performance is not required. Thus, the driving requirements are flexible form factor, large surface area and reduced system cost. The ultimate purpose of flexible electronics is to enable electronic platforms that are not feasible and/or not cost-efficient with existing Silicon-based technologies. Besides, it should be noted here that the goal of flexible electronics is not to replace mainstream Silicon technologies, but rather to implement those functions that are not well addressed by conventional Silicon technologies. The main enablers of flexible

electronics include its mechanical flexibility, large-area manufacturing and potential low-cost in volume. Hence, the focus of flexible electronics is on those applications where properties such as flexibility, conformability and light weight are demanded, or for applications where a large area is required.

### 1.1.1 Flexible electronic technologies

Flexible electronic technologies can be divided in the following categories depending on the nature of the semiconductor material used.

#### Amorphous Silicon

Amorphous Silicon (a-Si:H or a-Si) is the most well-known thin-film semiconductor [1], generally used in display backplanes. The fabrication process of a-Si based TFTs requires only 4-5 mask steps and it results in n-type only devices. The standard process temperature for a-Si is about 250°C-350°C. The amorphous nature of a-Si gives it a good uniformity but the charge carrier mobility is very low ranging between 0.5-1  $\text{cm}^2\text{V}^{-1}\text{s}^{-1}$ . Moreover, the electrical stability of a-Si based devices is poor, which results in threshold voltage shifts of as large as 10 V [2, 3].

#### Low temperature polycrystalline Silicon

Low temperature polycrystalline Silicon (LTPS) can be used as an alternative semiconductor for high-performance display backplanes. LTPS transistors exhibit mobility in the range of 50-100  $\text{cm}^2\text{V}^{-1}\text{s}^{-1}$  due to the polycrystalline nature of the semiconductor, with the additional possibility of fabrication of both p-type and n-type transistors. However, the small crystals give rise to grain boundaries resulting in device-to-device non-uniformity. A higher process temperature (around 500°C) is one other drawback while the more complex process flow with additional mask steps [4] results in larger cost and lower yield compared to a-Si.

### Organic semiconductors

Organic semiconductors have been explored to overcome the limitations, concerning the processing temperature, of a-Si and LTPS [5, 6, 7, 8]. The maximum processing temperature for organic semiconductor based TFTs is about 100°C. Typical mobility values for organic semiconductors lie in the range of 1-10  $\text{cm}^2\text{V}^{-1}\text{s}^{-1}$ . The organic semiconductors are mostly p-type, but n-type organic materials are also available nowadays. Environmental factors affect organic semiconductors much more than a-Si or LTPS due to their chemical nature, which makes proper encapsulation necessary for standard use, as it has been shown, for instance, in organic light emitting diodes (OLED) displays.

### Metal-oxide semiconductors

Metal-oxide semiconductors are a class of materials exhibiting excellent semiconducting behaviour at low processing temperature (around 250°C). Although, the first metal-oxide transistor was reported in 1964 [9] using semiconducting  $\text{SnO}_2$ , it was the work by Hosono's group that gave a fundamental contribution to the field of flexible TFTs demonstrating for the first time amorphous Indium Gallium Zinc Oxide (a-IGZO) TFTs deposited on a flexible substrate at room temperature [10]. The most prominent metal-oxides are oxides of In, Zn, Ga and Sn. These semiconductors exhibit comparatively high electron mobility in the range of 1-50  $\text{cm}^2\text{V}^{-1}\text{s}^{-1}$ . The amorphous nature of these oxides give them good uniformity. These metal oxides show good operational stability as well, making them an attractive choice for a variety of applications. Generally, metal oxides are electron-conducting semiconductors, hence, resulting in n-type TFTs.

It is clear from the ongoing discussion that amorphous metal-oxide TFTs exhibit overall a better performance trade-off compared to other semiconducting materials in terms electron carrier mobility, operational stability and low thermal budget. For these reasons, from now on, our focus in this thesis will be limited to a-IGZO tech-

nology which is available at imec-NL/TNO (Holst Centre), Eindhoven and imec, Leuven.

### 1.1.2 Design challenges

The physical properties of flexible electronic materials and their processing give rise to many design challenges at circuit and system level, which are summarized below:

#### Low frequency noise

The low quality interface between dielectric and semiconductor, together with mobility fluctuation results in large low-frequency noise ( $1/f$  or flicker noise) in thin film transistors [11]. Moreover, the  $1/f$  noise component is the dominant noise contribution for bio-signal acquisition front-ends owing to the low frequency content of biomedical signals. Hence, low-frequency noise mitigation is the foremost challenge in designing bio-signal acquisition front-ends. Flicker noise can be suppressed by using chopping [12], but at the cost of larger bandwidth requirements. It can be decreased by increasing device area as well, which exacerbates the negative role of the amplifier input parasitic capacitance, reducing input impedance. Discrete time circuit techniques such as auto-zeroing and correlated double sampling can also be exploited to mitigate  $1/f$  noise [12]. However, such techniques require large capacitors which are difficult to integrate in TFT technologies with acceptable yield, at the state-of-the-art.

#### Low efficiency

One of the main limitations of TFTs is their mobility, which is one to two orders of magnitude smaller than mainstream Silicon field effect transistors. Low mobility results in low transconductance ( $g_m$ ) of the devices, which consequently limits the small-signal intrinsic gain ( $g_m r_o$ ) and transition frequency ( $f_T$ ). Moreover, the large oxide thickness typically available in TFTs results in limited electrostatic control

over the channel, which ultimately leads to larger supply voltages. From the circuit design perspective, this results in low gain-bandwidth product (GBW) and low efficiency in terms of speed versus needed power.

### **Variability**

The low process temperature and low-cost manufacturing of TFTs result in large parameter variability. Apart from that, the low process temperature, which is the enabler of mechanical flexibility, is also responsible for limited control of device characteristics, resulting in poor intrinsic matching between identical neighbouring devices [13]. For instance, analogue to digital conversion in presence of variability and poor matching becomes extremely challenging.

### **Unipolar nature of devices**

The unipolar nature of the devices in a-IGZO technology makes it impossible to use well-known CMOS circuit techniques. Consequently, active loads with simple configuration and low transistor count are not available in unipolar technologies. The low intrinsic gain and the absence of complementary devices limit the gain attainable with unipolar flexible TFT based amplifiers, which makes structures based on feedback less useful in stabilizing the closed-loop performance compared to standard CMOS solutions.

### **Interfacing with Silicon**

Circuits consisting of TFTs generally require a high supply voltage in the range of 10-20 V due to thicker dielectrics used in flexible TFTs, while state-of-the-art Silicon based circuits are operated at supply voltages around 1 V. This inherent difference in supply voltage domains makes interfacing of flexible circuits with Silicon based circuits in hybrid systems quite challenging.

### 1.1.3 Applications

The research in the field of flexible electronics, in its nascent phase, focused primarily on applications related to digital circuits, due to considerable challenges in realizing analogue functions. There has been an immense research and industrial effort in applications related to large area displays, Radio Frequency Identification (RFID) and Near Field Communication (NFC) tags in the last decade. However, in recent years, there has been a paradigm shift, thanks to advancements in the processing technology. Now, many novel applications are being envisioned using flexible electronics including: physiological monitoring by wearable flexible health patches, epidermal electronics, flexible implants, flexible e-tattoos and wearable electronics for wellness. With the advent of IoT, flexible electronics is expected to make an even bigger impact in many diverse fields.

### 1.1.4 State-of-the-art flexible wearable biomedical sensors

Wearable biomedical devices have witnessed a growing interest in the recent years. Biomedical wearables typically aim at measuring vital signs of different organs, such as the brain, the muscles and the heart. Biomedical signal monitoring requires wearable devices to be conformable to the shape of the body, in order to improve the quality of signal monitoring and to ensure maximum comfort of use. Advancements in fabrication techniques and new materials that make it possible to build flexible and conformal electronics are thus an important enabler to build wearables for biomedical applications [14, 15, 16]. In the last few years, many research groups have focused on system integration. These efforts have resulted in the development of hybrid flexible electronics systems consisting of flexible electronics systems integrated with rigid conventional Silicon based systems, as well as the realization of fully flexible platforms.

Present flexible wearable biomedical sensors can be broadly classified in three categories:

1. Wearable devices in which all active components are rigid Silicon ICs. These devices are built by encapsulation and packaging techniques exploiting flexible or elastic layers, by integration in fabrics and/or by using flexible interconnects. These wearables can implement complex electronic functionality thanks to the Silicon ICs, at the cost of a reduced comfort level for the user, due to the presence of many rigid parts. Examples of such IC-based wearables include electrocardiogram (ECG) sensors with electrodes integrated into a cotton T-shirt [17], cardiac sensors where a rigid IC is encapsulated in elastic layers [18, 19], stretchable “e-tattoos” for ECG and temperature monitoring [20], and a portable electrocorticography (ECoG) system with a flexible microelectrodes array [21]. Multimodal bio-signal acquisition has been demonstrated too, with stretchable sensors capable of monitoring several combinations of electroencephalography (EEG), ECG, electromyography (EMG), electrooculography (EOG) and photoplethysmography (PPG) [22, 23, 24].
2. Wearable devices in which sensors and/or front end elements are based on flexible materials/substrates while the rest of the system is implemented with rigid Silicon ICs. In this type of hybrid solutions, flexible electronic devices and sensors are used for interfacing with the human body, while rigid electronics (conventional Silicon ICs) are used for signal processing and communication functions such as amplification, filtering, digitization and data transmission. In this way, the flexibility and conformability of the flexible substrate are combined with the good signal acquisition and processing capability of rigid components. In this approach, however, the manufacturing steps and costs increase, due to the processing required to integrate flexible and rigid parts. Besides, the rigid components may result in reduced patient comfort and disturbance to the measurements due to movements. Examples of this category of wearable sensors include screen-printed electrodes for ECG [25, 26], electrophysiological sensing arrays [27], self-powered ultra-flexible electronics using organic electrochemical transistors [28], implantable sen-

sors for the brain [29], flexible printed electrodes for EEG [30], a pulse oximeter based on organic materials compatible with flexible substrates [31], an ultrasonic device conformable to the skin and capable of monitoring blood pressure [32] and epidermal electronics for multimodal physiological monitoring [33].

3. Wearable devices in which all components are built using flexible electronics. The materials exploited in these flexible devices are lightweight and fully conformable to the human body, ensuring at least in principle maximum user comfort. Examples of such wearable sensors include flexible ECG monitoring devices [32, 34, 35], a prosthetic skin with stretchable multi-electrode arrays for nerve stimulation [36], organic electrochemical transistors for ECoG monitoring [37], large-area flexible or stretchable sensors able to detect arterial pulses [32, 38] and an epidermal electronic system capable of monitoring ECG and EMG [39]. Although, all these examples show the feasibility of flexible or conformable wearable devices, the inherently poor electric performance of flexible TFT technologies results in limited electronic functionality for this class of wearables. For instance, all smart bio-signal sensors based only on flexible components, at the state-of-the-art lack digitization of the measured signals and data transmission capability.

## 1.2 Problem statement

There are many challenges, as discussed in Section 1.1.2, in realizing flexible wearable devices. Therefore, simple, innovative and non-conventional approaches at circuit and system level, along with exploring the integration and form factor possibilities, need to be researched to come up with solutions, where conformable wearable devices provide sufficient performance to be used in real case applications.

## 1.3 Aim of the thesis

The aim of this thesis is to advance the state-of-the-art of flexible electronics with specific focus on wearable bio-signal measurement systems. The research described in this thesis is carried out mainly focusing on the following aspects:

- Design of analogue and mixed signal building blocks in flexible TFT technologies
  - Design single stage and multi stage amplifiers with different topologies to get an insight into performance trade-offs and maximum gain architectures in unipolar flexible technologies.
  - Design of voltage-to-time converters, to translate voltage-domain signals to the time domain, in order to provide a robust method for quantization in the presence of variability.
- Design of wearable bio-signal measurement systems using only flexible electronics
  - Design wearable bio-signal measurement systems composed of flexible electronics only, enhancing user comfort due to the conformability of flexible foil and reducing cost due to low cost of large area electronics.
- Design of a multichannel wearable bio-signal measurement system using flexible hybrid electronics integrating flexible TFTs on foil and a Silicon IC
  - Design a multichannel wearable hybrid flexible electronics system exploiting together the large area character of flexible technologies and the better performance/efficiency of Si ICs, with emphasis on system partitioning and on interfacing of different supply voltage domains of Silicon and flexible technologies.

## 1.4 Scope of the thesis

The work presented in this thesis focuses on the design and characterization of wearable bio-potential systems, manufactured using a-IGZO TFTs fabricated at imec-NL/TNO (Holst Centre), Eindhoven and imec, Leuven. The specific applications targeted are given below:

- Wearable bio-signal measurement systems based exclusively on flexible electronics
  - A heart-rate readout patch manufactured with flexible a-IGZO TFTs
  - A flexible ECG patch compatible with NFC RF communication

In the above application cases, the full signal chain has been chosen to be implemented by flexible TFTs, as the ultimate goal is to develop an NFC enabled health patch that can be read by a smart phone, which will lead to an ultra-low cost solution.

- Flexible hybrid wearable multichannel bio-potential system
  - A multichannel hybrid flexible electronics EOG patch consisting of front ends on flexible foil and data processing using custom Silicon IC

In this application case, the hybrid system approach has been chosen, as the goal is to explore the large area character of flexible TFTs with a more generic radio option which ultimately would require a Silicon based custom IC at the state-of-the-art.

## 1.5 Original contributions

The work presented in this manuscript advances the state-of-the-art in flexible unipolar technologies for bio-potential systems by introducing novel configurations at circuit and system level. The author's main contributions are highlighted as follows:

- In Chapter 3, the key design metrics in bio-signal front-end architectures, highlighting the trade-offs that are specifically relevant to a-IGZO TFT circuits, are discussed. Different front-ends for bio-signal sensing systems are designed and fabricated using a-IGZO TFT technology. The front-ends are characterized and compared in terms of different performance metrics, including power efficiency factor (PEF) (noise and power), input impedance and area. Based on this comparison, an insight into performance trade-offs in bio-signal front-ends in flexible technologies is obtained and optimum front-end architectures for different specific applications are highlighted.
- In Chapter 4, a novel idea of voltage to pulse width conversion with a simple and power minimalistic implementation is presented. A switched capacitor load has been exploited, in a modified single slope reset integrator circuit. The idea is further elaborated by implementing a heart-rate measurement interface for wearable applications, fabricated on a flexible foil with a-IGZO TFTs.
- In Chapter 5, we report for the first time (to the best of the authors' knowledge) a flexible ECG sensor which exploits TFT-based circuits on a flexible foil for the full chain of signal acquisition, amplification and digitization, and is capable to measure ECG signals. Additionally, a 105.9 kb/s Manchester encoded bit stream compatible with the NFC standard is generated at the output. The reported noise efficiency factor (NEF) and PEF are 109.81 and  $1.20 \times 10^5$  respectively, which are the best values reported in literature for a-IGZO TFT circuits to date.
- In Chapter 6, a multichannel acquisition system for EOG is presented. The system, consisting of a frontend based on a-IGZO TFTs manufactured on flexible substrate, is interfaced with a Silicon based custom IC for digitization of the acquired signal. In this way the low cost, flexible form factor and the large area character of the flexible TFT technology are leveraged, while

utilising the complex computational capabilities of Si IC with low power dissipation. A tunable hybrid HPF has been integrated in the system which is used to block DC electrode offset and allows low high-pass cut-off frequency. The system is designed in a novel way to reduce the number of interconnects from the flexible system to the Silicon IC. There is basically only one differential signal and a reference interconnect required between TFT and Si IC, which reduces the area needed for interconnections on the Si chip, and thus cost.

- In Chapter 7, a novel digitally assisted tunable high pass filter for biomedical applications, using unipolar a-IGZO TFTs is presented. The proposed system is based on a master-slave approach. It takes advantage of the signal attenuation experienced in a high pass filter when a reference sinusoidal signal with a frequency lower than the cut off frequency is applied. The signal attenuation is monitored and a feedback loop automatically controls the small-signal resistance in the master and slave filters to obtain a specific signal attenuation, which in turn sets the passband frequency of the high pass filter. The presented approach is not only useful for setting a sub Hz cut off frequency but it is shown to be effective in counteracting parameter and supply voltage variations. The presented method can also be applied to Silicon-based circuits.

## 1.6 Outline of the thesis

The manuscript is organized in the following fashion: Chapter 2 presents the description of the technology with detailed TFT device structure, fabrication steps and device modelling. In Chapter 3, the design trade-offs in bio-signal sensing front-ends based on a-IGZO TFTs are presented. The front-ends are characterized and compared in terms of different performance metrics, giving insight into performance trade-offs in bio-signal front-ends in flexible technologies. Chapter

4 presents the design and characterization of a heart-rate measurement interface for wearable applications using a time domain reset integrator circuit. Chapter 5 focuses on the design and characterization of a flexible ECG patch implemented completely on foil, which is capable to acquire the ECG signals, amplify them and convert them to a sequence of bits. Chapter 6 shows the design and characterization of an EOG hybrid system composed of multichannel acquisition system on flexible foil, while digitization is done using a Silicon IC. In Chapter 7, a digitally assisted tunable high pass filter for biomedical applications, implemented using unipolar a-IGZO TFTs is presented. Finally, Chapter 8 draws the main conclusions of the thesis.

## Bibliography

- [1] W. Spear and P. L. Comber, "Substitutional doping of amorphous Silicon," *Solid State Communications*, vol. 17, pp. 1193–1196, Nov. 1975.
- [2] S. M. Jahinuzzaman, A. Sultana, K. Sakariya, P. Servati, and A. Nathan, "Threshold voltage instability of amorphous Silicon thin-film transistors under constant current stress," *Applied Physics Letters*, vol. 87, p. 023502, July 2005.
- [3] D. Zhou, M. Wang, and S. Zhang, "Degradation of amorphous Silicon thin film transistors under negative gate bias stress," *IEEE Transactions on Electron Devices*, vol. 58, pp. 3422–3427, Oct. 2011.
- [4] J. Y. Yang, S. H. Kim, Y. I. Park, J. S. Yoo, D. Y. Lee, J. Y. Oh, S. J. Hong, J. I. Lee, K. M. Oh, S. W. Lee, H. C. Kang, K. M. Lim, C. D. Kim, M. S. Yang, and I. J. Chung, "27.1: A novel structure of AMLCD panel using poly-si CMOS TFT," *SID Symposium Digest of Technical Papers*, vol. 36, no. 1, p. 1149, 2005.
- [5] C. D. Dimitrakopoulos and D. J. Masearo, "Organic thin-film transistors: A review of recent advances," *IBM Journal of Research and Development*, vol. 45, pp. 11–27, Jan. 2001.
- [6] C. Dimitrakopoulos and P. Malenfant, "Organic thin film transistors for large area electronics," *Advanced Materials*, vol. 14, no. 2, pp. 99–117, 2002.
- [7] Y. Zhao, Y. Guo, and Y. Liu, "25th anniversary article: Recent advances in n-type and ambipolar organic field-effect transistors," *Advanced Materials*, vol. 25, pp. 5372–5391, Aug. 2013.
- [8] H. Sirringhaus, "25th anniversary article: Organic field-effect transistors: The path beyond amorphous Silicon," *Advanced Materials*, vol. 26, pp. 1319–1335, Jan. 2014.
- [9] H. Klansens and H. Koelmans, "A tin oxide field-effect transistor," *Solid-State Electronics*, vol. 7, pp. 701–702, Sept. 1964.
- [10] K. Nomura, H. Ohta, A. Takagi, T. Kamiya, M. Hirano, and H. Hosono, "Room-temperature fabrication of transparent flexible thin-film transistors using amorphous oxide semiconductors," *Nature*, vol. 432, pp. 488–492, Nov. 2004.

- [11] T.-C. Fung, G. Baek, and J. Kanicki, "Low frequency noise in long channel amorphous In-Ga-Zn-O thin film transistors," *Journal of Applied Physics*, vol. 108, p. 074518, Oct. 2010.
- [12] C. Enz and G. Temes, "Circuit techniques for reducing the effects of op-amp imperfections: autozeroing, correlated double sampling, and chopper stabilization," *Proceedings of the IEEE*, vol. 84, no. 11, pp. 1584–1614, 1996.
- [13] D. Tu, K. Takimiya, U. Zschieschang, H. Klauk, and R. Forchheimer, "Modeling of drain current mismatch in organic thin-film transistors," *Journal of Display Technology*, vol. 11, pp. 559–563, June 2015.
- [14] Y. Khan, A. E. Ostfeld, C. M. Lochner, A. Pierre, and A. C. Arias, "Monitoring of vital signs with flexible and wearable medical devices," *Advanced Materials*, vol. 28, no. 22, pp. 4373–4395, 2016.
- [15] Y. Khan, M. Garg, Q. Gui, M. Schadt, A. Gaikwad, D. Han, N. A. D. Yamamoto, P. Hart, R. Welte, W. Wilson, S. Czarnecki, M. Poliks, Z. Jin, K. Ghose, F. Egitto, J. Turner, and A. C. Arias, "Flexible hybrid electronics: Direct interfacing of soft and hard electronics for wearable health monitoring," *Advanced Functional Materials*, vol. 26, no. 47, pp. 8764–8775, 2016.
- [16] J. C. Costa, F. Spina, P. Lugoda, L. Garcia-Garcia, D. Roggen, and N. Münzenrieder, "Flexible sensors—from materials to applications," *Technologies*, vol. 7, p. 35, Apr. 2019.
- [17] E. Nemati, M. Deen, and T. Mondal, "A wireless wearable ECG sensor for long-term applications," *IEEE Communications Magazine*, vol. 50, pp. 36–43, Jan. 2012.
- [18] S. P. Lee, G. Ha, D. E. Wright, Y. Ma, E. Sen-Gupta, N. R. Haubrich, P. C. Branche, W. Li, G. L. Huppert, M. Johnson, H. B. Mutlu, K. Li, N. Sheth, J. A. Wright, Y. Huang, M. Mansour, J. A. Rogers, and R. Ghaffari, "Highly flexible, wearable, and disposable cardiac biosensors for remote and ambulatory monitoring," *npj Digital Medicine*, vol. 1, p. 2, Jan. 2018.
- [19] Y. Li, Y. Luo, S. Nayak, Z. Liu, O. Chichvarina, E. Zamburg, X. Zhang, Y. Liu, C. H. Heng, and A. V.-Y. Thean, "A stretchable-hybrid low-power monolithic ECG patch with

- microfluidic liquid-metal interconnects and stretchable Carbon-black nanocomposite electrodes for wearable heart monitoring,” *Advanced Electronic Materials*, vol. 5, no. 2, p. 1800463, 2019.
- [20] H. Jeong, L. Wang, T. Ha, R. Mitbander, X. Yang, Z. Dai, S. Qiao, L. Shen, N. Sun, and N. Lu, “Modular and reconfigurable wireless e-tattoos for personalized sensing,” *Advanced Materials Technologies*, vol. 4, no. 8, p. 1900117, 2019.
- [21] K. Xie, S. Zhang, S. Dong, S. Li, C. Yu, K. Xu, W. Chen, W. guo, J. Luo, and Z. Wu, “Portable wireless electrocorticography system with a flexible microelectrodes array for epilepsy treatment,” *Scientific Reports*, vol. 7, Aug. 2017.
- [22] S. Xu, Y. Zhang, L. Jia, K. E. Mathewson, K.-I. Jang, J. Kim, H. Fu, X. Huang, P. Chava, R. Wang, S. Bhole, L. Wang, Y. J. Na, Y. Guan, M. Flavin, Z. Han, Y. Huang, and J. A. Rogers, “Soft microfluidic assemblies of sensors, circuits, and radios for the skin,” *Science*, vol. 344, no. 6179, pp. 70–74, 2014.
- [23] K.-I. Jang, K. Li, H. U. Chung, S. Xu, H. N. Jung, Y. Yang, J. W. Kwak, H. H. Jung, J. Song, C. Yang, A. Wang, Z. Liu, J. Y. Lee, B. H. Kim, J.-H. Kim, J. Lee, Y. Yu, B. J. Kim, H. Jang, K. J. Yu, J. Kim, J. W. Lee, J.-W. Jeong, Y. M. Song, Y. Huang, Y. Zhang, and J. A. Rogers, “Self-assembled three dimensional network designs for soft electronics,” *Nature Communications*, vol. 8, p. 15894, June 2017.
- [24] H. U. Chung, B. H. Kim, J. Y. Lee, J. Lee, Z. Xie, E. M. Ibler, K. Lee, A. Banks, J. Y. Jeong, J. Kim, C. Ogle, D. Grande, Y. Yu, H. Jang, P. Assem, D. Ryu, J. W. Kwak, M. Namkoong, J. B. Park, Y. Lee, D. H. Kim, A. Ryu, J. Jeong, K. You, B. Ji, Z. Liu, Q. Huo, X. Feng, Y. Deng, Y. Xu, K.-I. Jang, J. Kim, Y. Zhang, R. Ghaffari, C. M. Rand, M. Schau, A. Hamvas, D. E. Weese-Mayer, Y. Huang, S. M. Lee, C. H. Lee, N. R. Shanbhag, A. S. Paller, S. Xu, and J. A. Rogers, “Binodal, wireless epidermal electronic systems with in-sensor analytics for neonatal intensive care,” *Science*, vol. 363, no. 6430, 2019.
- [25] S. Imani, A. J. Bandodkar, A. M. V. Mohan, R. Kumar, S. Yu, J. Wang, and P. P. Mercier, “A wearable chemical-electrophysiological hybrid biosensing system for real-time health and fitness monitoring,” *Nature Communications*, vol. 7, p. 11650, May 2016.

- [26] D. Son, J. Kang, O. Vardoulis, Y. Kim, N. Matsuhisa, J. Y. Oh, J. W. F. To, J. Mun, T. Katsumata, Y. Liu, A. F. McGuire, M. Krason, F. Molina-Lopez, J. Ham, U. Kraft, Y. Lee, Y. Yun, J. B.-H. Tok, and Z. Bao, "An integrated self-healable electronic skin system fabricated via dynamic reconstruction of a nanostructured conducting network," *Nature Nanotechnology*, vol. 13, pp. 1057–1065, Nov. 2018.
- [27] H. Fang, K. J. Yu, C. Gloschat, Z. Yang, E. Song, C.-H. Chiang, J. Zhao, S. M. Won, S. Xu, M. Trumpis, Y. Zhong, S. W. Han, Y. Xue, D. Xu, S. W. Choi, G. Cauwenberghs, M. Kay, Y. Huang, J. Viventi, I. R. Efimov, and J. A. Rogers, "Capacitively coupled arrays of multiplexed flexible Silicon transistors for long-term cardiac electrophysiology," *Nature Biomedical Engineering*, vol. 1, p. 0038, Mar. 2017.
- [28] S. Park, S. W. Heo, W. Lee, D. Inoue, Z. Jiang, K. Yu, H. Jinno, D. Hashizume, M. Sekino, T. Yokota, K. Fukuda, K. Tajima, and T. Someya, "Self powered ultraflexible electronics via nano grating patterned organic photovoltaics," *Nature*, vol. 561, pp. 516–521, Sept. 2018.
- [29] S.-K. Kang, R. K. J. Murphy, S.-W. Hwang, S. M. Lee, D. V. Harburg, N. A. Krueger, J. Shin, P. Gamble, H. Cheng, S. Yu, Z. Liu, J. G. McCall, M. Stephen, H. Ying, J. Kim, G. Park, R. C. Webb, C. H. Lee, S. Chung, D. S. Wie, A. D. Gujar, B. Vemulapalli, A. H. Kim, K.-M. Lee, J. Cheng, Y. Huang, S. H. Lee, P. V. Braun, W. Z. Ray, and J. A. Rogers, "Bioresorbable Silicon electronic sensors for the brain," *Nature*, vol. 530, pp. 71–76, Feb. 2016.
- [30] S. Debener, R. Emkes, M. De Vos, and M. Bleichner, "Unobtrusive ambulatory EEG using a smartphone and flexible printed electrodes around the ear," *Scientific Reports*, vol. 5, p. 16743, Nov. 2015.
- [31] C. M. Lochner, Y. Khan, A. Pierre, and A. C. Arias, "All-organic optoelectronic sensor for pulse oximetry," *Nature Communications*, vol. 5, p. 5745, Dec. 2014.
- [32] Y. Wang, Y. Qiu, S. K. Ameri, H. Jang, Z. Dai, Y. Huang, and N. Lu, "Low-cost,  $\mu\text{m}$ -thick, tape-free electronic tattoo sensors with minimized motion and sweat artifacts," *npj Flexible Electronics*, vol. 2, p. 6, Feb. 2018.

- [33] Y. Zhang and T. H. Tao, "Skin-friendly electronics for acquiring human physiological signatures," *Advanced Materials*, vol. 31, no. 49, p. 1905767, 2019.
- [34] T. Sekitani, T. Yokota, K. Kuribara, M. Kaltenbrunner, T. Fukushima, Y. Inoue, M. Sekino, T. Isoyama, Y. Abe, H. Onodera, and T. Someya, "Ultraflexible organic amplifier with biocompatible gel electrodes," *Nature Communications*, vol. 7, p. 11425, Apr. 2016.
- [35] J. H. Koo, S. Jeong, H. J. Shim, D. Son, J. Kim, D. C. Kim, S. Choi, J.-I. Hong, and D.-H. Kim, "Wearable electrocardiogram monitor using Carbon nanotube electronics and color-tunable organic light-emitting diodes," *ACS Nano*, vol. 11, pp. 10032–10041, Oct. 2017.
- [36] J. Kim, M. Lee, H. J. Shim, R. Ghaffari, H. R. Cho, D. Son, Y. H. Jung, M. Soh, C. Choi, S. Jung, K. Chu, D. Jeon, S.-T. Lee, J. H. Kim, S. H. Choi, T. Hyeon, and D.-H. Kim, "Stretchable Silicon nanoribbon electronics for skin prosthesis," *Nature Communications*, vol. 5, p. 5747, Dec. 2014.
- [37] D. Khodagholy, T. Doublet, P. Quilichini, M. Gurfinkel, P. Leleux, A. Ghestem, E. Ismailova, T. Hervé, S. Sanaur, C. Bernard, and G. G. Malliaras, "In vivo recordings of brain activity using organic transistors," *Nature Communications*, vol. 4, p. 1575, Mar. 2013.
- [38] X. Wang, Y. Gu, Z. Xiong, Z. Cui, and T. Zhang, "Silk-molded flexible, ultrasensitive, and highly stable electronic skin for monitoring human physiological signals," *Advanced Materials*, vol. 26, no. 9, pp. 1336–1342, 2014.
- [39] W.-H. Yeo, Y.-S. Kim, J. Lee, A. Ameen, L. Shi, M. Li, S. Wang, R. Ma, S. H. Jin, Z. Kang, Y. Huang, and J. A. Rogers, "Multifunctional epidermal electronics printed directly onto the skin," *Advanced Materials*, vol. 25, no. 20, pp. 2773–2778, 2013.



# Chapter 2

## a-IGZO TFT Technology

*In this Chapter, the a-IGZO TFT fabrication process developed at imec-NL/TNO (Holst Centre), Eindhoven and imec, Leuven, used in this thesis, is presented. Further, the details about the device stack of the TFTs are described. Finally, a brief overview of the physical-based compact models, used to describe channel current and noise of the TFTs, is given.*

## 2.1 Introduction

The chosen technology in the work described in this thesis, uses TFTs fabricated with a-IGZO as semiconductor. Amorphous IGZO is a relatively new semiconducting material, which got international recognition from Hosono's work [1] in 2004. Since then, it has been extensively used in commercial applications such as active-matrix displays etc.

## 2.2 Device stack

The device stack here refers to the order in which different thin film layers are processed to fabricate a device. During the entire course of the work presented in this thesis, many variants of a-IGZO TFTs evolved in imec-NL/TNO (Holst Centre), Eindhoven and imec, Leuven. Out of those variants, depending on the availability, Etch-Stop Layer (ESL) TFTs and Dual-Gate Self Aligned (DUGA) TFTs were used for this work and will be discussed in detail below.

## 2.3 Etch stop layer TFT technology

The cross section of a typical device based on Etch Stop Layer (ESL) technology [2] is shown in Figure 2.1. It can be seen from the cross section that it has a staggered bottom-gate top-contact structure. All the layers are processed on top of a flexible polyimide substrate, with a maximum temperature of 250°C.

In this device, a 100 nm Molybdenum-Chromium (MoCr) metal film, which acts as the gate layer (M1), is sputtered on top of the substrate. Next, a 200 nm SiO<sub>2</sub> gate dielectric is deposited by a plasma enhanced chemical vapor deposition (PECVD) process, which is followed by DC sputtering of a 12 nm thick IGZO layer. This is followed by spin coating a photoresist layer on top.

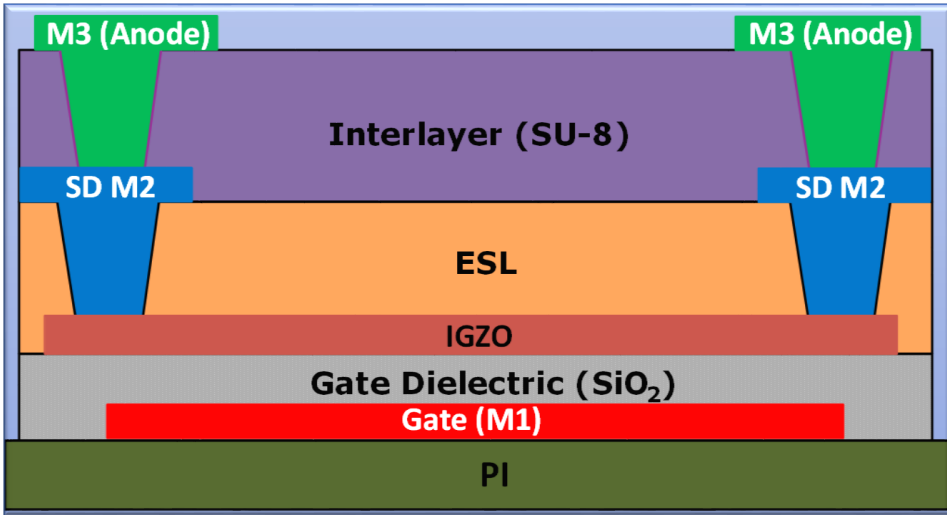


*Figure 2.1: Cross section of an a-IGZO TFT based on ESL flow.*

Next, a 100 nm  $\text{SiO}_2$  layer is patterned on top of the semiconductor, using PECVD at  $200^\circ\text{C}$ . This layer, known as ESL, prevents damage of the semiconductor when processing the other layers. The contact openings are created using dry etching in the ESL layer, which is followed by sputtering of a second metal layer (M2) using MoCr target, resulting in formation of the source drain (SD) contacts. The next step is the deposition of a  $2\text{ }\mu\text{m}$  thick SU-8 passivation layer (interlayer) on top of the second metal layer. This layer provides a low-capacitance insulation for the third metal, planarization and some protection from environmental influence.

Finally, a third metal layer (M3) (anode) can be optionally sputtered. This third metal layer can be very useful in wearables, e.g. to form integrated electrodes that pick up bio-potential signals on the surface of the TFT stack.

The TFTs based on the ESL technology suffer from two major drawbacks. Firstly, the accuracy in the processing steps necessitates margin between the transistor contact holes in the ESL layer and the source drain/metal layer, which results in a minimum channel length of  $15\text{ }\mu\text{m}$  for single gate devices, whereas the minimum

feature size of this technology is 5  $\mu\text{m}$ . The other drawback is the added parasitic capacitance due to the large overlap between gate and source/drain.

## 2.4 Dual-gate self aligned TFT technology

To achieve better speed performance and to solve the problems associated with the ESL TFT technology, the Dual-Gate Self Aligned (DUGA) stack [3] was developed. The cross-sectional view of a DUGA a-IGZO TFT is shown in Figure 2.2. The layer stack consists of a plastic substrate, a barrier layer, back gate (BG) metal M0, back gate dielectric, a-IGZO, top gate dielectric  $\text{SiO}_2$ , top gate (TG) metal M1, interlayer dielectric and source drain (SD) metal M2. The fabrication process starts with the deposition of a buffer layer on a polyimide plastic substrate. Then a BG metal (MoCr) is deposited by physical vapor deposition (PVD). This step is followed by deposition of the back gate dielectric ( $\text{SiO}_2$ ) by PECVD at 350°C. The next step involves the deposition of the a-IGZO layer (20 nm with 10% ratio of  $\text{O}_2/\text{Ar}$ ) by DC sputtering and patterning with wet etching.

After that, the top gate dielectric ( $\text{SiO}_2$ ) is deposited using PECVD at 250°C, which is followed by TG metal (Mo) layer deposition. Afterwards, the top gate stack including metal layer and dielectric is patterned using wet and dry etch in a combined step. Then an interlayer dielectric ( $\text{SiN}_x$ ) is deposited by PECVD at 250°C. Patterning of contact vias using dry etch follows. In the same step BG, TG and SD are contacted. The last step involves the deposition of SD (Ti-Al-Ti) metal using PVD and patterning by dry etching. Finally, annealing of the samples takes place at 240°C in  $\text{N}_2$  for 1 hour.

The flexible polyimide substrate for the TFT process is hold on glass during manufacturing and released afterwards. The circuits realized in this way can be bent without significantly modifying their electrical characteristics [2].

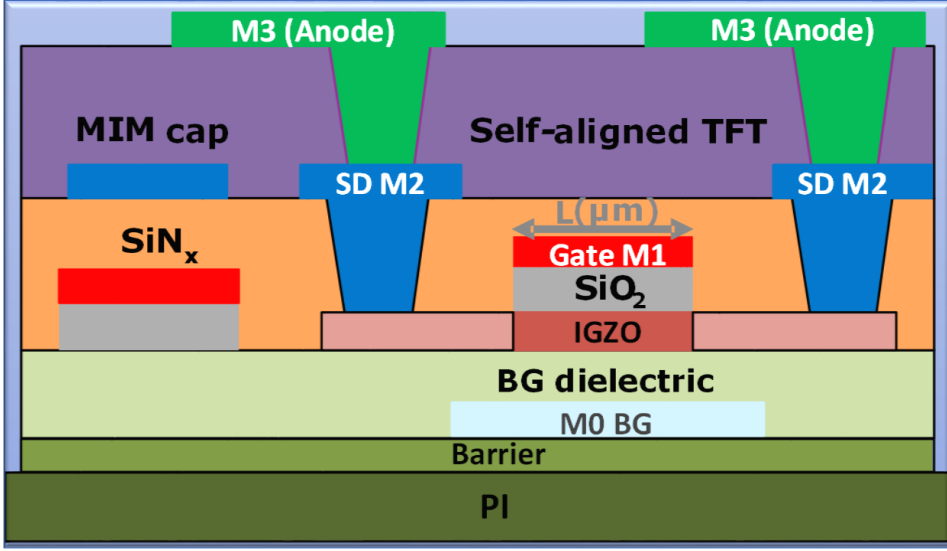


Figure 2.2: Cross section of an a-IGZO TFT based on DUGA flow.

## 2.5 Device channel current modelling

### 2.5.1 ESL channel current modelling

The analytical physical-based model described in [4] has been used to model channel current in ESL TFTs. The drift-diffusion drain current integral [5, 6] in the TFT can be modelled as

$$I_{DS} = \frac{W}{L} \int_{V_S}^{V_D} \int_0^{\phi_s} \frac{q\mu_b n_b(\phi, V_{ch})}{\sqrt{F_{xt}^2(\phi, V_{ch}) + F_{xb}^2(\phi, V_{ch})}} d\phi dV_{ch} \quad (2.1)$$

where  $W$  is the channel width,  $L$  is the channel length,  $V_S$  and  $V_D$  are the source and the drain voltages, respectively,  $V_{ch}$  is the channel potential,  $\phi$  is the electrostatic potential,  $\phi_s$  is the surface potential at the insulator-semiconductor interface,  $n_b$  is the free charge carrier concentration,  $\mu_b$  is the band mobility,  $F_{xt}$  and  $F_{xb}$ , are the electric fields calculated accounting for the trapped and the free charges, respectively. Solving Equation 2.1, taking into account both conduction regimes, the

drain current can be written as:

$$I_{DS} = \frac{W}{L} \frac{\Gamma_t \Psi_t \times \Gamma_b \Psi_b}{\Gamma_t \Psi_t + \Gamma_b \Psi_b} \quad (2.2)$$

where:

$$\Gamma_t = \frac{\varepsilon_s \mu_b N_b}{C_{ox}} k_B T \frac{T}{2T_t - T} \left[ \frac{C_{ox}^2}{2\varepsilon_s N_t \theta_t k_B T_t} \right]^{\frac{T_t}{T}} \quad (2.3)$$

$$\Gamma_b = \frac{\mu_b C_{ox}}{2} \quad (2.4)$$

$$\Psi_t = \left[ \phi_{GS}^{\frac{2T_t}{T}} - \phi_{GD}^{\frac{2T_t}{T}} \right] \quad (2.5)$$

$$\Psi_b = [\phi_{GS}^2 - \phi_{GD}^2] \quad (2.6)$$

$$\phi_{GX} = V_G - V_{fb} - \phi_{sX} \quad (2.7)$$

where  $\mu_b$  is the band mobility,  $\varepsilon_s$  is the a-IGZO permittivity,  $N_b$  is the total number of delocalized (band) states,  $N_t$  is the total number of localized (trapped) states,  $T_t$  is the characteristic temperature of the localized states,  $\theta_t$  accounts for the dependence of free and trapped charge concentrations on both  $T$  and  $T_t$ ,  $V_G$  and  $V_{fb}$  are the gate and the flatband voltage, respectively,  $C_{ox}$  is the gate capacitance per unit area,  $\phi_{sX}$ , with  $X \in \{S, D\}$  is the surface potential at the source or drain.

Furthermore, it has been observed that the model overestimates the drain current due to contact effects. Hence, the contact model presented in [7] has been added to the model, which describes the contact effect as a reverse biased Schottky-gated diode as shown in Figure 2.3, and can be written as:

$$I_c = W \times I_0 \times \exp\left(\sqrt[4]{\frac{V_c}{V_0}}\right) \times \left[ \exp\left(-\frac{qV_c}{\eta k_B T}\right) - 1 \right] \quad (2.8)$$

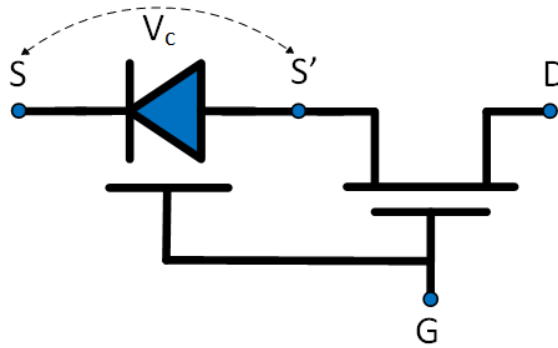


**Figure 2.3:** Schematic device model including a reverse biased Schottky-gated diode.

$$I_0 = I_{00} \times \left\{ \log \left[ 1 + \exp \left( \frac{V_G - V_{fb}}{V_{00}} \right) \right] \right\}^\gamma \quad (2.9)$$

where  $V_0$  accounts for the Schottky barrier lowering effect,  $\eta$  is the quality factor,  $I_{00}$  is the reverse current prefactor,  $V_{00} = 1$  and it is introduced to keep the dimensionality of the pre-factor  $I_{00}$  and  $\gamma$  is a fitting parameter.

Figure 2.4 shows the typical transfer characteristics of an ESL TFT with comparison between the model and the measurements. It can be seen that the model is in good agreement with the measurements.

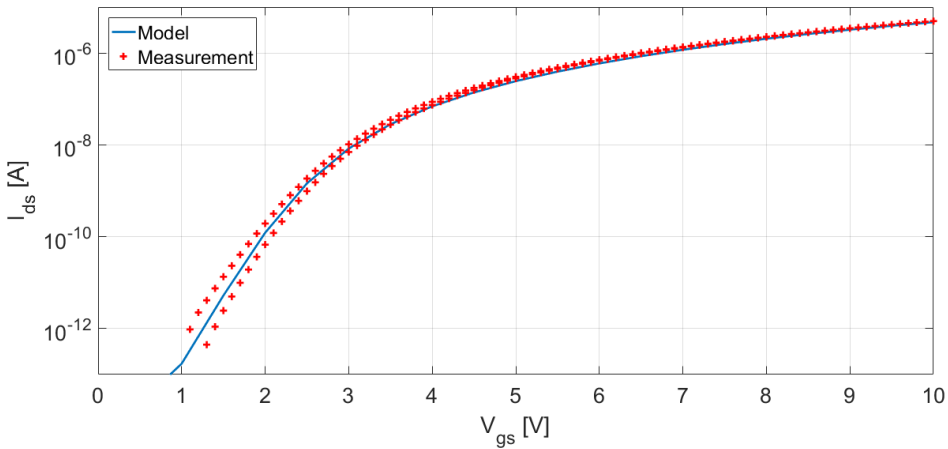


**Figure 2.4:** Measured transfer characteristics of ESL TFT (in hysteresis mode) compared to model simulations.

### 2.5.2 DUGA channel current modelling

The channel current model for DUGA TFTs developed by the Large Area Electronics group of imec, Leuven has been used in this thesis [8]. The channel current for a single TFT can be described as [9]:

$$I_{DS} = \frac{\mu_0 C_{ox}}{2} \frac{W}{L} (V_{GS} - V_T)^{2+\gamma} \quad (2.10)$$

Equation 2.10 can be further written as:

$$I_{DS} = \frac{\mu_0 C_{ox}}{2} \frac{W}{L} [(V_{GS} - V_T)^{2+\gamma_S} - (V_{GD} - V_T)^{2+\gamma_D}] \quad (2.11)$$

The model represented by Equation 2.11 is further modified to incorporate sub-threshold behaviour and back gate model to finally obtain a complete DC model, described by the following Equations :

$$I_{DS} = \frac{\mu_{0S} C_{ox}}{2} \frac{W}{L} V_{GSTe}^{2+\gamma_S} - \frac{\mu_{0D} C_{ox}}{2} \frac{W}{L} V_{GDTe}^{2+\gamma_D} \quad (2.12)$$

$$V_{GXTe} = (2 + \gamma_X) SS_X \log_{10} \left( 1 + 10^{\left( \frac{V_G - V_X - V_{TX}}{(2 + \gamma_X) SS_X} \right)} \right) \quad (2.13)$$

$$V_{TX} = V_{T0} - \zeta (V_{BG} - V_X) \quad (2.14)$$

$$\gamma_X = \gamma_0 + \gamma_1 (V_{BG} - V_X) \quad (2.15)$$

$$\mu_{0X} = \mu_{00} + \mu_{01} (V_{BG} - V_X) + \mu_{02} (V_{BG} - V_X)^2 \quad (2.16)$$

$$SS_X = SS_0 + SS_1 (V_{BG} - V_X) \quad (2.17)$$

Equation 2.12 represents channel current behavior, Equation 2.13 describes subthreshold behavior while Equations 2.14, 2.15, 2.16 and 2.17 represents the shift caused by the backgate in  $V_T$ ,  $\gamma$ ,  $\mu_0$  and subthreshold slope (SS) respectively.

Figure 2.5 shows the transfer characteristics of a DUGA TFT with a comparison between the model and the measurements, when  $V_{BG}$  is varied between -5 V to 5 V. Also in this case, a good fit between the measurements and the model of the TFT is observed.

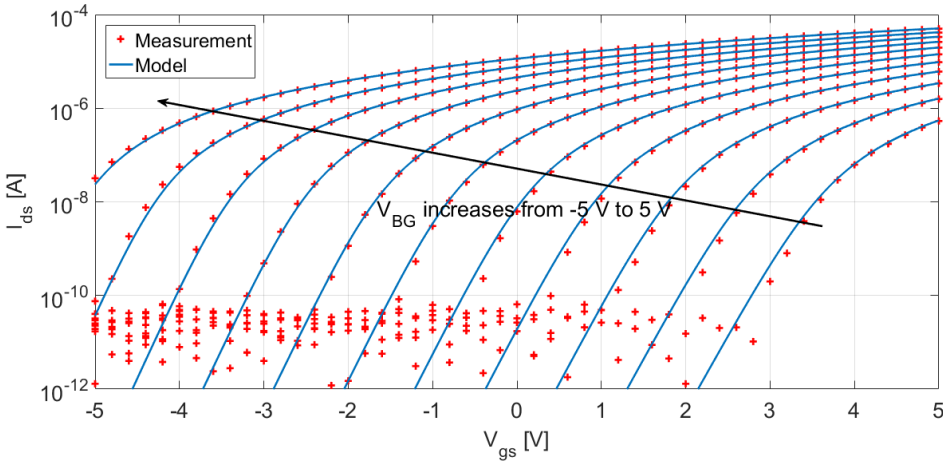


**Figure 2.5:** Measured transfer characteristics of DUGA TFT compared to model simulations when  $V_{BG}$  is varied between -5 V to 5 V. Note that the points under  $10^{-10}$  A are dominated by noise [8].

## 2.6 Device noise modelling

The current noise behavior in field effect transistors can be modelled with two main contributions, which are related to the thermal and flicker noise. The power spectral density (PSD) of the drain current associated to the thermal noise contribution can be written as:

$$S_{I_D,thermal}(f) = 4k_B T \left( \frac{2}{3} \right) g_m \quad (2.18)$$

where  $k_B$  is the Boltzmann constant,  $T$  is the temperature, and  $g_m$  is the transconductance of the device.

However, the noise contribution in a-IGZO TFTs is generally dominated by flicker noise [10]. It has been shown in [10] that the mobility fluctuation model describes well the noise behaviour of a-IGZO TFTs. The flicker noise PSD in the a-IGZO TFTs' current can be modelled [11] as:

$$S_{I_D, flicker}(f) = \frac{\alpha_H q I_D^2}{f W L C_{ox} (V_{GS} - V_T)} \quad (2.19)$$

where  $\alpha_H$  is the Hooge coefficient,  $I_D$  is the bias current,  $WL$  is the area of the device,  $C_{ox}$  is the channel capacitance per unit area and  $V_{GS} - V_T$  is the overdrive voltage.

## 2.7 Conclusions

The a-IGZO TFT fabrication process used in this thesis has been presented in this Chapter. Furthermore, the a-IGZO TFTs based on etch stop layer and self aligned dual-gate stacks have been shown. Finally, compact models used to describe channel current and noise of the TFTs are described. The channel current models have been shown to be in good agreement with measurements.

## Bibliography

- [1] K. Nomura, H. Ohta, A. Takagi, T. Kamiya, M. Hirano, and H. Hosono, "Room-temperature fabrication of transparent flexible thin-film transistors using amorphous oxide semiconductors," *Nature*, vol. 432, pp. 488–492, Nov. 2004.
- [2] A. K. Tripathi, K. Myny, B. Hou, K. Wezenberg, and G. H. Gelinck, "Electrical characterization of flexible InGaZnO transistors and 8-b transponder chip down to a bending radius of 2 mm," *IEEE Transactions on Electron Devices*, vol. 62, pp. 4063–4068, Dec. 2015.
- [3] M. Nag, F. D. Roose, K. Myny, S. Steudel, J. Genoe, G. Groeseneken, and P. Heremans, "Characteristics improvement of top-gate self-aligned amorphous indium gallium zinc oxide thin-film transistors using a dual-gate control," *Journal of the Society for Information Display*, vol. 25, pp. 349–355, June 2017.
- [4] M. Ghittorelli, F. Torricelli, J.-L. V. D. Steen, C. Garripoli, A. Tripathi, G. H. Gelinck, E. Cantatore, and Z. M. Kovacs-Vajna, "Physical-based analytical model of flexible a-IGZO TFTs accounting for both charge injection and transport," in *2015 IEEE International Electron Devices Meeting (IEDM)*, pp. 28.2.1–28.2.4, IEEE, Dec. 2015.
- [5] F. Torricelli, J. R. Meijboom, E. Smits, A. K. Tripathi, M. Ferroni, S. Federici, G. H. Gelinck, L. Colalongo, Z. M. Kovacs-Vajna, D. de Leeuw, and E. Cantatore, "Transport physics and device modeling of zinc oxide thin-film transistors part I: Long-channel devices," *IEEE Transactions on Electron Devices*, vol. 58, pp. 2610–2619, Aug. 2011.
- [6] F. Torricelli, E. C. P. Smits, J. R. Meijboom, A. K. Tripathi, G. H. Gelinck, L. Colalongo, Z. M. Kovacs-Vajna, D. M. de Leeuw, and E. Cantatore, "Transport physics and device modeling of zinc oxide thin-film transistors part II: Contact resistance in short channel devices," *IEEE Transactions on Electron Devices*, vol. 58, pp. 3025–3033, Sept. 2011.
- [7] A. Valletta, A. Daami, M. Benwadih, R. Coppard, G. Fortunato, M. Rapisarda, F. Torricelli, and L. Mariucci, "Contact effects in high performance fully printed p-channel organic thin film transistors," *Applied Physics Letters*, vol. 99, p. 233309, Dec. 2011.
- [8] F. D. Roose, H. Celiker, J. Genoe, W. Dehaene, and K. Myny, "Dual-gate self-aligned a-

- InGaZnO transistor model for flexible circuit applications,” in *2019 Design, Automation & Test in Europe Conference & Exhibition (DATE)*, pp. 25–29, IEEE, Mar. 2019.
- [9] O. Marinov, M. J. Deen, U. Zschieschang, and H. Klauk, “Organic thin-film transistors: Part I compact DC modeling,” *IEEE Transactions on Electron Devices*, vol. 56, pp. 2952–2961, Dec. 2009.
- [10] T.-C. Fung, G. Baek, and J. Kanicki, “Low frequency noise in long channel amorphous In–Ga–Zn–O thin film transistors,” *Journal of Applied Physics*, vol. 108, p. 074518, Oct. 2010.
- [11] J.-M. Lee, W.-S. Cheong, C.-S. Hwang, I.-T. Cho, H.-I. Kwon, and J.-H. Lee, “Low-frequency noise in amorphous indium–gallium–zinc-oxide thin-film transistors,” *IEEE Electron Device Letters*, vol. 30, pp. 505–507, May 2009.

# Chapter 3

## Design Trade-offs in a-IGZO TFT based Bio-signal Front-ends

*In this Chapter, four different bio-signal front-end circuits based on a-IGZO TFTs are designed, fabricated, measured and compared, focusing on three performance indicators which are in a trade-off: power efficiency factor (PEF), area occupation and input impedance.*

*The contents of this Chapter have been published in Flexible and Printed Electronics [1].*

### 3.1 Introduction

A typical implementation of a bio-signal acquisition system requires sensors/electrodes, amplifiers, analogue signal processing blocks and analog-to-digital converter circuits in the full acquisition chain. The front-end amplifier is probably the most fundamental analogue building block that is inevitably present in every system. This Chapter deals with front-end amplifiers manufactured with a-IGZO TFTs on a flexible substrate.

As discussed in detail in Chapter 1, bio-signal acquisition systems on flexible substrates are inferior to mainstream Silicon technology in terms of performance, due to the low intrinsic gain, large parasitics and high flicker noise typical of flexible TFTs. However, it has been shown that bio-signal acquisition systems using TFTs on flexible substrate can achieve the accuracy required even for demanding biomedical applications such as electroencephalography (EEG) [2]. To implement bio-signal front-ends using flexible technologies, a technology-aware circuit design approach that takes into account the technology's peculiar characteristics, optimizing circuit functionality, is a must.

In this Chapter, we first discuss the key metrics in bio-signal front-end architectures, highlighting the trade-offs that become especially important when a-IGZO TFTs are used. We then discuss the realization of different front-ends for bio-signal sensing systems, designed and fabricated using a-IGZO TFT technology. The front-ends are characterized and compared in terms of different performance metrics, including noise, power, input impedance and area. Based on this comparison, we get insight into performance trade-offs in bio-signal front-ends in flexible technologies and highlight optimum front-end architectures for different specific applications.

The Chapter is organized as follows: in Section 3.2 design constraints for bio-signal front-ends are discussed together with the relevant trade-offs. Section 3.3 presents several bio-signal front-end architectures based on representative state-of-the-art designs, discussing their advantages and disadvantages. Section 3.4 gives a brief overview of the limitations of a-IGZO TFTs and the impact of their properties

on the design of bio-signal front-ends. Section 3.5 presents the chosen front-end topologies implemented with a-IGZO TFTs. Measurement results are presented and discussed in Section 3.6, and Section 3.7 gives the conclusions.

## 3.2 Design constraints for bio-signal front-ends

Bio-signal front-ends are mostly used to amplify weak bio-signals generated by muscular and neural tissues, in the typical range of  $10\ \mu\text{V}$ – $10\ \text{mV}$ , in the presence of DC electrode offset which may be as large as  $\pm 300\ \text{mV}$ , as well as motion artefacts. The bandwidth of bio-signals typically lies in the range of  $0.5\ \text{Hz}$ – $5\ \text{kHz}$  [3]. The bio-signal front-ends should meet many challenging requirements to extract the weak bio-signals with such a large DC offset. These requirements can be listed as follows:

- sufficient signal to noise ratio;
- low power dissipation for longer battery life;
- high input impedance to minimize signal attenuation from electrode to front-end;
- reduced area occupation for low cost and high spatial resolution depending upon the bio-signal monitoring application;
- removal of DC electrode offset to prevent saturation of the front-end;
- high common mode rejection ratio (CMRR) to reject interferers.

Low noise is required for an accurate measurement. In the low-frequency bio-signal band,  $1/f$  noise is dominant, and thus circuit techniques such as chopping are used to suppress it below the thermal noise level. Consequently, the main noise contribution in Silicon front-end circuits becomes thermal noise. The input referred

spectral density of thermal noise in a transistor is given by:

$$\overline{v_n^2} = 4kT\gamma/g_m \quad (3.1)$$

where parameter  $\gamma$  depends on the bias point of the transistor and is typically assumed to be 2/3 in a transistor above threshold and in saturation. It can be seen from Equation 3.1 that the thermal noise spectral density in a transistor is inversely proportional to its transconductance  $g_m$ . The transconductance increases with a larger bias current. For this reason, a fundamental trade-off exists between noise and bias current, which is especially relevant to biomedical front-ends. This trade-off is typically characterized in amplifiers by a figure of merit called the noise efficiency factor (NEF) [4]:

$$\text{NEF} = V_{ni,rms} \sqrt{\frac{2I_{tot}}{\pi \cdot U_T \cdot 4kT \cdot \text{BW}}}, \quad (3.2)$$

where  $V_{ni,rms}$  is the total input referred noise,  $I_{tot}$  is the total supply current of the amplifier, BW is the amplifier –3 dB bandwidth, and  $U_T$  is the thermal voltage. As it can be seen from Equation 3.2, the NEF does not take into account the supply voltage. For this reason, to compare circuits having a different supply voltage  $V_{DD}$ , the power efficiency factor (PEF) was introduced in [5]:

$$\text{PEF} = \text{NEF}^2 V_{DD}, \quad (3.3)$$

The PEF can be used to characterize the trade-off between noise and power consumption, and will be used in the later Sections of this Chapter to compare different a-IGZO front-ends. Another important requirement is that bio-signal front-ends should have a large input impedance  $Z_{in}$ , to minimize the signal attenuation from the electrodes to the front-end. Indeed, the input signal is partitioned between the electrode impedance and  $Z_{in}$ , and thus a large input impedance is desired, especially in ambulatory applications. We will use  $Z_{in}$  as a second figure of merit

to compare different a-IGZO front-ends. A third important parameter in the design of biomedical front-ends is their area occupation: a compact front-end may be cheaper to fabricate and enables higher spatial resolution, which in applications like e.g. electromyography (EMG), EEG and recordings of the neural cortex can be useful to improve diagnostic accuracy [6, 7]. The large DC electrode offset is another pressing problem often encountered in bio-signal front-ends. One obvious solution is to use AC coupled architectures, which inherently removes offset at the cost of large area to implement the input capacitors. CMRR is another important parameter in the design of bio-signal front-ends. It should be as large as possible to suppress coupling from the mains and other sources of interference.

From the above discussion, it is clear that PEF, input impedance and area are important parameters when designing biomedical front-ends. From now on in this Chapter, we will focus on these three parameters to compare different circuits for bio-signal sensing. The DC offset and CMRR are not considered to simplify the comparison. Section 3.3 will present a few typical biomedical front-end architectures, while Section 3.4 will discuss the trade-offs existing between these parameters when designing bio-signal front-ends using a-IGZO TFTs.

### 3.3 Bio-signal front-end architectures

Three most representative power efficient approaches for the design of biomedical front-ends in the recent literature, are illustrated in Figure 3.1. The architecture in Figure 3.1(a) uses an open-loop amplifier,  $A_1$ , to amplify the input signal. Given the low frequency range of biomedical signals (as low as 0.5 Hz), a very low high-pass corner ( $1/(2\pi R_{in}C_{in})$ ) is required, implying the need for a large  $R_{in}C_{in}$ . In addition, thanks to the low frequencies of bio-signals, chopping is a widely used technique to modulate the signal at higher frequencies and suppress the amplifier flicker noise and offset. In Figure 3.1, this is shown with  $CH_{in}$  and  $CH_{out}$  representing input and output chopper, respectively. In Figure 3.1(a),  $CH_{in}$  is placed

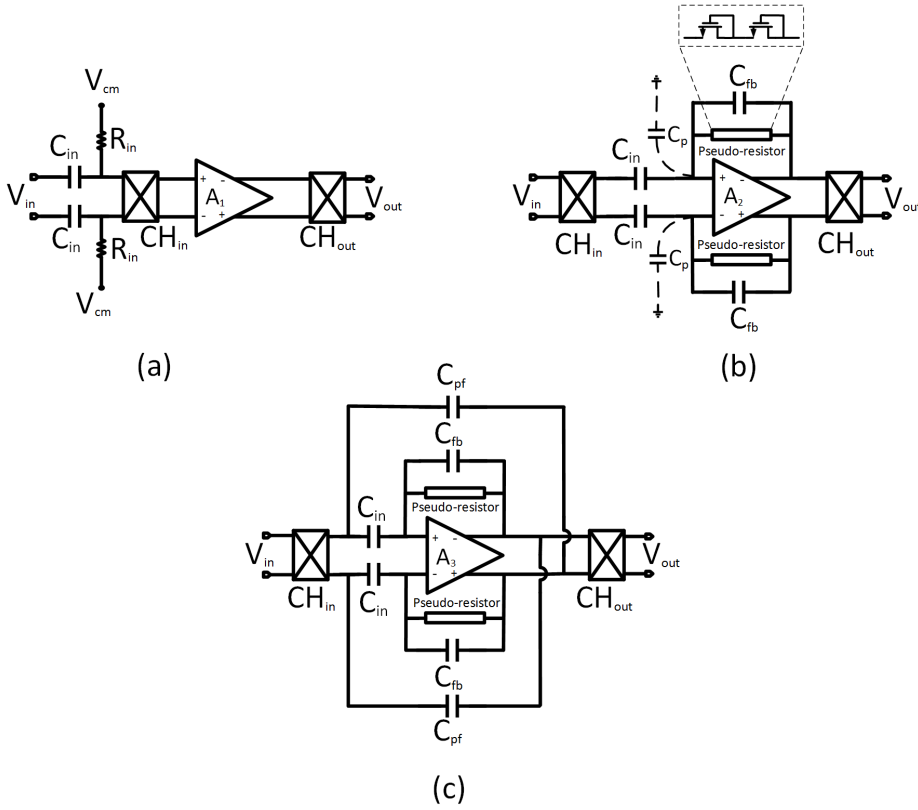


**Figure 3.1:** Bio-signal front-ends implemented with (a) an open loop amplifier (b) an amplifier in capacitive feedback (c) an amplifier in capacitive feedback with additional impedance-boosting positive feedback loop.

after the high-pass filter, to ensure the effectiveness of electrode offset blocking. However, using this approach, any mismatch in the capacitors  $C_{in}$  will affect the CMRR. In addition, this circuit exacerbates the negative role of the amplifier input parasitic capacitance  $C_p$ . Calling the chopping frequency  $f_{chop}$  and the input signal frequency  $f_{in}$ , the switched-capacitor resistor seen at the input of the amplifier due to the chopping of its input parasitic capacitance is  $1/(2f_{chop}C_p)$  and, assuming that  $R_{in}$  is very large, the amount of input signal  $V_{in}$  coupled to the input of the amplifier can be approximated to be  $V_{Ain} = \frac{j2\pi f_{in}C_{in}}{j2\pi f_{in}C_{in} + 2f_{chop}C_p} V_{in}$ . One should notice that typically  $f_{chop} \gg f_{in}$ . According to this equation thus, a very large  $C_{in}$  is needed to ensure negligible signal attenuation. To provide a numerical example, assuming

that  $f_{in} = 0.1$  Hz,  $f_{chop} = 1$  kHz, and  $C_p = 100$  pF, to ensure 10% attenuation one would need  $C_{in} = 664$  nF. This capacitance is so large that it cannot be integrated on foil with acceptable yield, at the state-of-the-art, and needs to be implemented using a discrete capacitor. In addition, the in-band input impedance of the overall front-end using chopping,  $Z_{in} \approx 1 / (2f_{chop}C_p)$ , is limited due to the relatively high chopping frequency needed to ensure noise suppression. Discrete capacitors are often used in state-of-the-art reports of bio-signal front-ends implemented with TFTs [2]. Considering for example commercial ceramic SMD solutions, a  $1 \mu\text{F}$  capacitor rated up to 50 V DC can be implemented in a  $1.6 \times 0.8 \text{ mm}^2$  footprint, with 0.8 mm height. These dimensions might still be compatible with flexible wearable solutions, provided that the capacitors are covered with a suitable e.g. silicone layer that covers the discrete components, smoothening the foil surface. Monolithic solutions, which are obviously more attractive from an integration and user-comfort perspective, would require adding a dedicated dielectric to the technology stack, which should offer a capacitance density significantly higher than the  $\sim 10 \text{ nF mm}^{-2}$  presently available with our technology.

Figure 3.1(b) depicts the use of an amplifier ( $A_2$ ) in capacitive feedback, resulting in an accurate gain set by the ratio of passive elements  $C_{in}/C_{fb}$  [8, 9, 10]. Capacitors are preferred to resistors to realize the feedback because they do not introduce additional noise sources to the circuit. As the input capacitors in this case are behind the input chopper, their mismatch does not contribute to loss of CMRR. However, this architectural choice results in a DC-coupled amplifier, which is affected by a large output signal due to the input offset up-converted to the chopping frequency and amplified. This might jeopardize the linearity of the front-end. The effect of the electrode offset can be suppressed at the cost of increased circuit complexity using DC servo-loops (DSL), as proposed in [9, 10]. The highly resistive pseudo-resistors shown the inset of Figure 3.1(b) ensure biasing of the amplifier input pair. They should be large enough to ensure that the chopped signal is in the band pass of the closed-loop amplifier. The use of pseudo-resistors, which are

largely variable and bias dependant, results in a very inaccurate high-pass pole. Besides, the linearity of this stage might be jeopardized by the bias sensitivity of the pseudo-resistors. Instead of exploiting pseudo-resistors, a DSL can be used to implement the high-pass response in the closed-loop amplifier [9].

Obviously, noise and gain considerations are very important in determining the size of the capacitors. The input referred noise of the bio-signal front-end in Figure 3.1(b) is given by:

$$\overline{v_{ni}^2} = \left( \frac{C_{in} + C_{fb} + C_p}{C_{in}} \right)^2 \overline{v_{ni,A_2}^2} \quad (3.4)$$

where  $C_p$  is the input parasitic capacitance and  $\overline{v_{ni,A_2}^2}$  the input referred noise of the main amplifier  $A_2$ . Equation 3.4 shows that the input referred noise of this front-end is an amplified version of the input referred noise of the amplifier. To minimize the total input referred noise,  $C_p$  must be minimized, and the mid-band gain, given by  $C_{in}/C_{fb}$ , should be as large as possible. For the front-end depicted in Figure 3.1(b),  $C_{in}$  can typically be integrated on foil, but still, according to Equation 3.4, it must be much larger than  $C_p$  and  $C_{fb}$ , resulting in large area occupancy and a limited input resistance. Indeed, the switching of  $C_{in}$  between positive and negative input every clock cycle requires a charging and discharging current from the signal source. Thus, the combination of input chopper and capacitors  $C_{in}$  results in the formation of a switched capacitor resistor offering an input impedance:

$$Z_{in} = \frac{1}{2f_{chop}C_{in}} \quad (3.5)$$

In the architecture of Figure 3.1(c), the input impedance is increased using a positive feedback loop (PFL) [10], realized by  $C_{pf}$ . The PFL supplies part of the current needed to charge the input capacitors at the chopping frequency. This current does not need to flow anymore from the input port, and thus the input impedance is increased. A drawback of this approach is that implementing the PFL results in area overhead due to the capacitors  $C_{pf}$ . Moreover, stability concerns in

the presence of parametric variability must be taken into account in this circuit. The condition for infinite input impedance [10] can be found to be:

$$C_{pf} = \frac{C_{in}}{G-1}, \quad (3.6)$$

where

$$G = \frac{A_3}{1 + A_3 \frac{C_{fb}}{C_{in}}}, \quad (3.7)$$

where  $A_3$  is the open loop gain of the op-amp. Hence, the condition for stability from Equation 3.6 is:

$$C_{pf} < \frac{C_{in}}{G-1}, \quad (3.8)$$

Considering the analysis of the circuit in Figure 3.1(c), it can be observed that when  $A_3$  is strongly variable and is not very large (as it will be the case in a-IGZO front-ends), a trade-off exists between improving input impedance and the risk of instability.

### 3.4 Limitations of a-IGZO TFT technology

In this Section, we discuss some of the limitations of a-IGZO TFTs and their impact on bio-signal measurement front-ends, with special focus on the trade-offs between PEF, input impedance and area occupation.

Considering the PEF, the fundamental difference between standard Silicon front-ends and a-IGZO TFT based front-ends is the noise corner frequency. In standard Silicon implementations, the noise corner frequency is lower than the bandwidth of the core amplifier and thus chopping frequencies larger than the noise corner frequency ( $f_c$ ) can be used i.e.  $f_{chop} > f_c$ . This results in a front-end noise being defined by the thermal contribution only, and in an effective cancellation of the flicker noise. In contrast, a-IGZO TFT based front-ends have a noise corner frequency which is generally larger than the bandwidth of the amplifier. As a consequence, a-IGZO front-ends can only be chopped with  $f_{chop} < f_c$ , which means that

a-IGZO front-ends are 1/f noise dominated at the state-of-the-art: this additional flicker contribution to noise greatly degrades the PEF.

The input referred flicker noise voltage spectral density for a single TFT can be written as:

$$S_{n,in}(f) = \frac{2\alpha_H q}{C_i(\gamma+2)^2 W^{\frac{\gamma+3}{\gamma+2}} L^{\frac{\gamma+1}{\gamma+2}} f} \gamma+2 \sqrt{\frac{I_{DS}}{\beta}} \quad (3.9)$$

The factor  $\gamma+2$  is typically higher than 3 [11], which implies that a change in  $I_{DS}$  will not result in large change in 1/f noise, while an increase in device area will result in significant noise reduction. As the most effective strategy to alleviate 1/f noise in a-IGZO amplifiers is to increase the area of the input devices, a trade-off exists between noise level (thus PEF) and area. Another important point in a-IGZO TFT based front-ends is the fact that most a-IGZO technologies currently do not offer a self-aligned TFT stack, and thus a-IGZO TFTs are characterized by a large gate-drain overlap capacitance  $C_{gd}$ . In a gain stage as the ones depicted in Figure 3.1, the  $C_{gd}$  of the input TFTs will create Miller effect. This means that the actual parasitic capacitance from the input node to ground can be found to be:

$$C_p \approx (1+a)C_{gd} \quad (3.10)$$

where  $a$  is the gain between gate and drain of the input TFTs. In a single-stage amplifier the gain  $a$  will be equal to the total amplifier gain  $A_i$ , introduced in Section 3.3.

When using an amplifier in a closed-loop bio-signal front-end of the type introduced in Figures 3.1(b) and (c), according to Equation 3.4, the input equivalent noise increases due to the large  $C_p$ , and this effect must be counteracted by an increase of  $C_{in}$  (and  $C_{fb}$ ), aggravating the trade-off between noise and area. On top of this, increasing  $C_{in}$  results in a decreased input impedance according to Equation 3.5, causing a trade-off between noise (and thus PEF) and input impedance.

To alleviate this trade-off, circuit techniques like impedance boosting introduced in Section 3.3 (Figure 3.1(c)) can be used, but this results in a consider-

able additional area overhead, in order to implement the capacitor banks needed to provide an accurate input impedance compensation. In summary, focusing on the main performance indicators PEF, area and input impedance, we can conclude that in bio-signal front-ends based on non-self-aligned a-IGZO TFTs the following trade-offs exist :

1. A trade-off between noise (PEF) and area due to:
  - the large TFTs needed to counteract  $1/f$  noise;
  - the detrimental effect on noise of the large TFT parasitic capacitances  $C_p$  (exacerbated by the Miller effect) which can only be alleviated by larger  $C_{in}$ .
2. A trade-off between noise (PEF) and input impedance, due to the need to select large input capacitors  $C_{in}$  in the presence of a large parasitic TFT input capacitance  $C_p$  to ensure good noise performance.
3. A trade-off between input impedance and area, due to the area overhead needed to implement impedance boosting techniques such as the positive feedback described in Section 3.3.

As discussed before, the a-IGZO technology is unipolar. For this reason, specific amplifiers topologies must be used, taking inspiration from the work done in Silicon technology in the late 1970s when only NMOS devices were available. In the next Section, a set of bio-signal front-ends based on a-IGZO TFTs will be presented and analysed.

### 3.5 Bio-signal front-ends based on a-IGZO TFTs

Four biomedical front-ends exploiting the architectures shown in Figures 3.1(a) and (c) have been designed and implemented using a-IGZO TFTs. The first front-end (FE) uses a typical robust core amplifier architecture, the second one uses a

core amplifier similar to the first, but optimized for lower  $1/f$  noise. The third and fourth FEs exploit amplifiers with a larger gain per stage. We explore three variants of core amplifiers using the open loop front-end architecture (Figure 3.1(a)), obtaining front-ends FE-I, FE-II and FE-III; and one topology of the core amplifier using the capacitive feedback front-end with impedance boosting (Figure 3.1(c)), obtaining FE-IV. The front-end schematics, including the topologies of the core amplifiers and the most relevant design parameters, are summarized in Figure 3.2 and Table 3.1 respectively. All front-ends are described in detail in the next Section. One should notice that all open-loop front-ends (FE-I, II and III) use discrete components to embody  $C_{in}$  and  $R_{in}$  ( $R_{in} = 1\text{ M}\Omega$  and  $C_{in} = 4.7\text{ }\mu\text{F}$ ). The bias current ( $I_{bias}$ ) in FE-I, FE-II and FE-IV is implemented using n-type a-IGZO TFT based current mirror with an external current source.

### 3.5.1 FE-I and FE-II

As a first option for the implementation of a biomedical front-end, we explore the open-loop architecture of Figure 3.1(a) with a core amplifier  $A_1$  based on a diode-connected load topology, as shown in Figure 3.2. As the gain of one stage is not sufficient for most of the applications, two stages are cascaded to obtain higher gain. Due to the moderate total gain and the fact that the gain is defined by a ratio of transconductances of matched devices ( $A = \frac{g_{m1}}{g_{m3}}$ ), this architecture is rather insensitive to general parameter variability, which is especially useful in the context of large area electronics due to its large variability. Two variants of the cascaded diode-connected load amplifier are considered: in the first front-end (FE-I), the input TFT pair is  $\frac{500\text{ }\mu\text{m}}{15\text{ }\mu\text{m}}$ , where the length is the minimum available in our technology to enable double-gate, and the width is chosen relatively small, to minimize  $C_p$  and its negative impact on input impedance. In the second front-end (FE-II), the input pair is made larger,  $\frac{4000\text{ }\mu\text{m}}{15\text{ }\mu\text{m}}$ , in order to reduce  $1/f$  noise at the cost of increased  $C_p$ , resulting in  $< 100\text{ }\mu\text{V}_{rms}$  simulated integrated noise in the bio-signal frequency band.

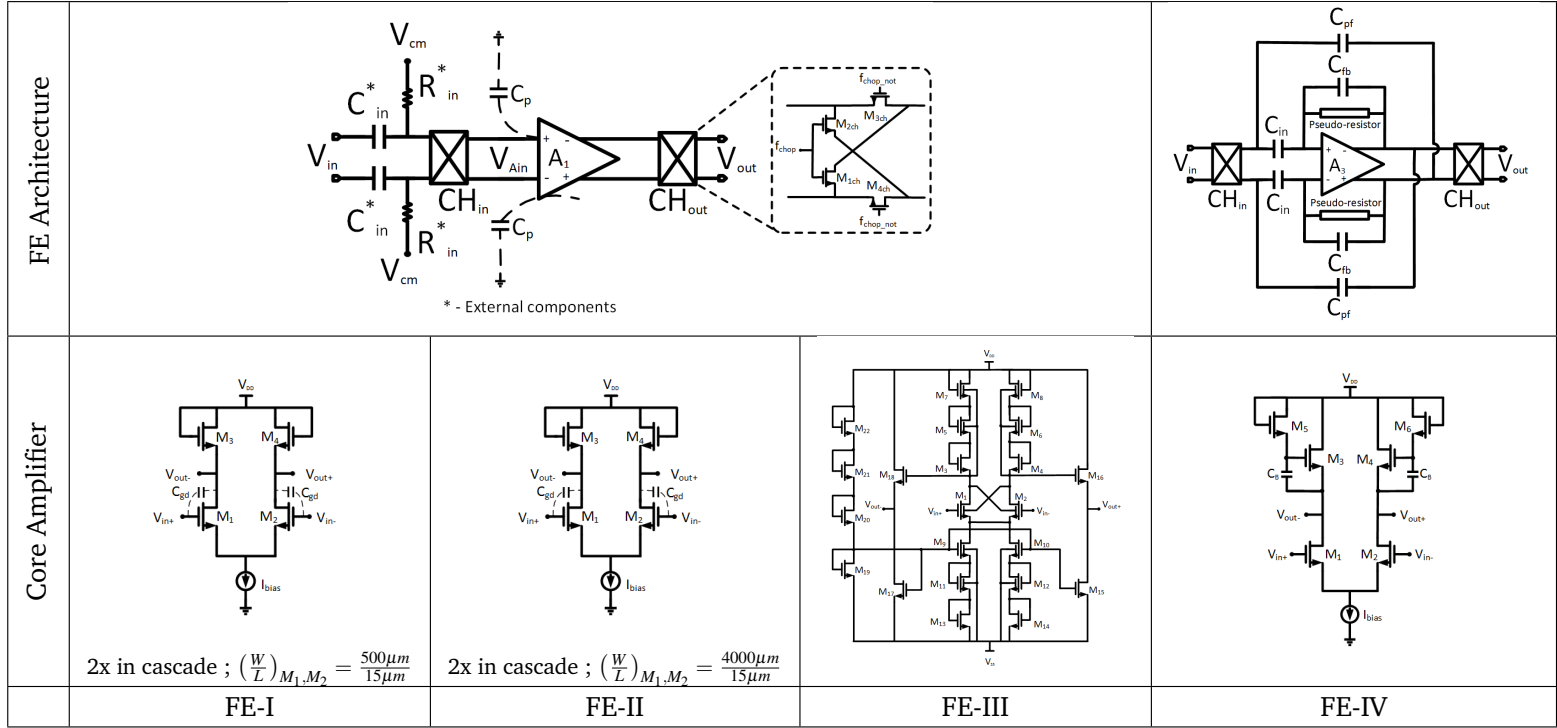


Figure 3.2: Architectural schematics of the presented front-ends with structural details of the core amplifiers.

### 3.5.2 FE-III

The next front-end is still an open-loop topology, where the core amplifier  $A_1$  is based on an enhanced diode-connected load and positive feedback techniques to increase the amplifier gain, according to the topology reported in [11] and shown in Figure 3.2. This amplifier uses a modified diode-connected load consisting of series diodes  $M_3$ ,  $M_5$  and  $M_7$  with the top gate of diode  $M_5$  and  $M_7$  connected to the source of  $M_3$ . In this configuration, the output resistance of  $M_5$  is increased by a factor of  $(1 + \eta)$  and the output resistance of  $M_3$  is increased by  $(1 + \eta)^2$  where  $\eta$  is the threshold modulation coefficient due to the presence of the top gate [11], which is typically larger than 2 for this technology. As the output resistance increases with this load arrangement, the DC gain also increases. The top gates of input transistors  $M_1$  and  $M_2$  are cross-coupled, creating a partial positive feedback which increases transconductance and, thus, gain.

At the output stage, a buffer, implemented with a source follower configuration ( $M_{16}$  and  $M_{18}$ ), is used to interface the amplifier with the measurement setup. The supply voltage is divided by four through a voltage divider composed of  $M_{19}$  to  $M_{22}$ . This voltage is then used to bias the gates of  $M_9$ ,  $M_{10}$ ,  $M_{15}$  and  $M_{17}$ , which are used as tail current source for the amplifier stage and the buffers.

Although this topology effectively enhances gain, it is sensitive to mismatch and variations. Indeed, the introduction of positive feedback in presence of large mismatch and variability may result in instability. Besides, as this amplifier has a low-pass response and large gain, the input DC offset of the amplifier, due to the large mismatch present in a-IGZO TFT technology can be amplified enough to saturate the stage. Another drawback of this architecture is limited available output swing which often necessitates higher supply voltages.

### 3.5.3 FE-IV

The last front-end is designed according to the impedance-boosting capacitive feedback architecture of Figure 3.1(c). The core amplifier  $A_3$  is implemented with the

*Table 3.1: Relevant design parameters of the presented front-ends.*

	FE-I	FE-II	FE-III	FE-IV
$C_{in}$ [pF]	$4.7 \times 10^6^a$	$4.7 \times 10^6^a$	$4.7 \times 10^6^a$	10
$C_{fb}$ [pF]	-	-	-	1
$C_{pf}$ [pF]	-	-	-	0.8
$C_B$ [nF]	-	-	-	1
$W_1/L_1$ [ $\mu m/\mu m$ ]	500/15	4000/15	5000/15	500/15

<sup>a</sup>These capacitors are implemented using discrete components.

bootstrapped load amplifier shown in Figure 3.2. This topology, proposed in [12] uses a load consisting of  $M_3$  and  $M_5$  with a bootstrapping capacitor  $C_B$ . At low frequencies,  $M_3$  behaves as a diode-connected load which is less sensitive to threshold variations due to its low gain, while at high frequencies it behaves as a zero- $V_{GS}$  load which provides higher gain. This topology has, thus, a characteristic band pass response, which is desirable to avoid saturation of the core amplifier due to the TFT mismatch.

### 3.6 Measurement results

The front-ends presented in the previous Section have been designed and fabricated using a-IGZO TFTs on foil. The foil micrographs of the presented circuits are shown in Figure 3.3.

In this Section, the measurements of these circuits are discussed. Figure 3.4 shows the measured frequency response of the bio-signal front-ends, using the whole FE architectures as shown in Figure 3.2, keeping the chopping off. Figures 3.4(a) and (b) show the gain plots of the two-stage cascaded diode-connected load amplifier in FE-I and FE-II respectively. The gain of the amplifier in FE-I is 22.9 dB with a  $-3$  dB frequency of 6.8 kHz, while for the amplifier with larger input TFTs, the gain is 26.9 dB with a  $-3$  dB frequency of 4 kHz. Figure 3.4(c) plots the frequency response of the enhanced diode-connected load amplifier. It shows a gain of 25.2 dB in a single stage, with a  $-3$  dB frequency of 400 Hz. The GBW

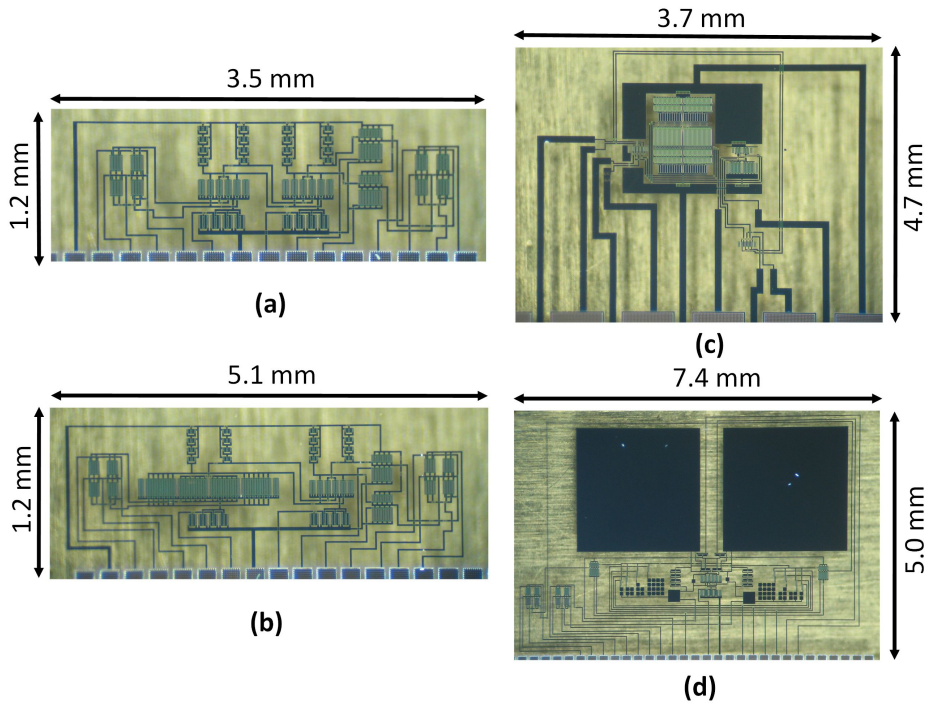


**Figure 3.3:** Foil micrograph of the fabricated front-ends (a) FE-I, (b) FE-II, (c) FE-III and (d) FE-IV.

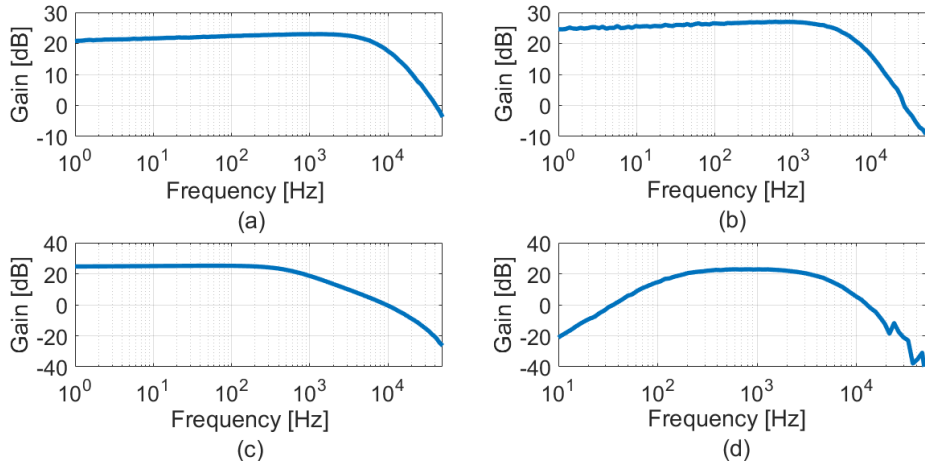
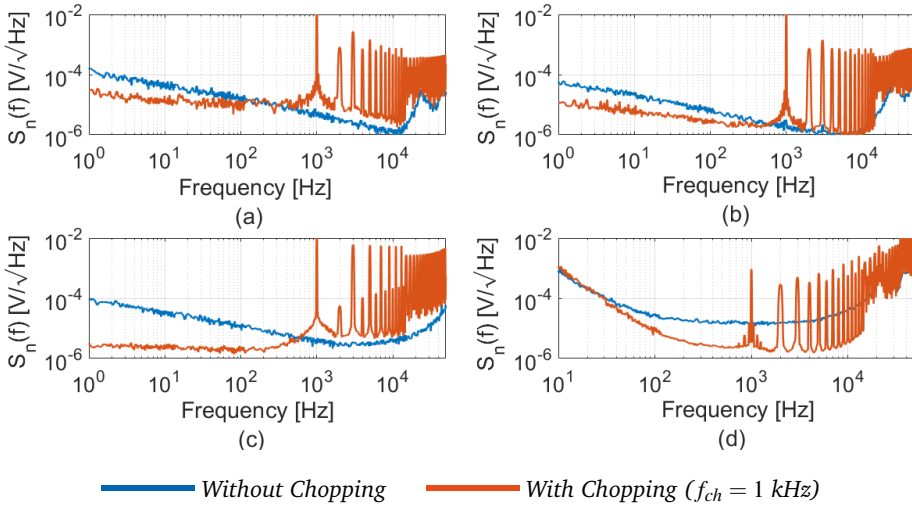


**Figure 3.4:** Frequency response of the amplifiers (a) FE-I, (b) FE-II, (c) FE-III and (d) FE-IV.

is reduced compared to the conventional diode-connected load due to the stronger Miller effect on the input devices observed in this single-stage topology. The last

plot of Figure 3.4(d) shows the frequency response of the bootstrapped amplifier with feedback network again without chopping. The lower and upper cut off frequency are 185 Hz and 3.3 kHz respectively with a mid-band gain of 22.8 dB. This value is slightly different from the theoretical one,  $C_{in}/C_{fb}$ , due to the parasitic TFT capacitances. Owing to the rather small capacitances  $C_B$  (1 nF) used in the design and the limited output resistance of the diode-connected devices  $M_5$  and  $M_6$ , the high-pass corner of the bootstrapped amplifier is at a rather high frequency (185 Hz). Such a high-pass is not compatible with low frequency biomedical signals like EMG and ECG. To cope with these signals, larger  $C_B$  capacitors, and/or a biasing of  $M_{5/6}$  ensuring higher output resistance should be used.

As mentioned earlier, it should also be noted that the first two amplifiers are two-stage while the last two are single stage. Besides, the last front-end is measured in closed-loop and thus its bandwidth is enhanced at the expense of gain.



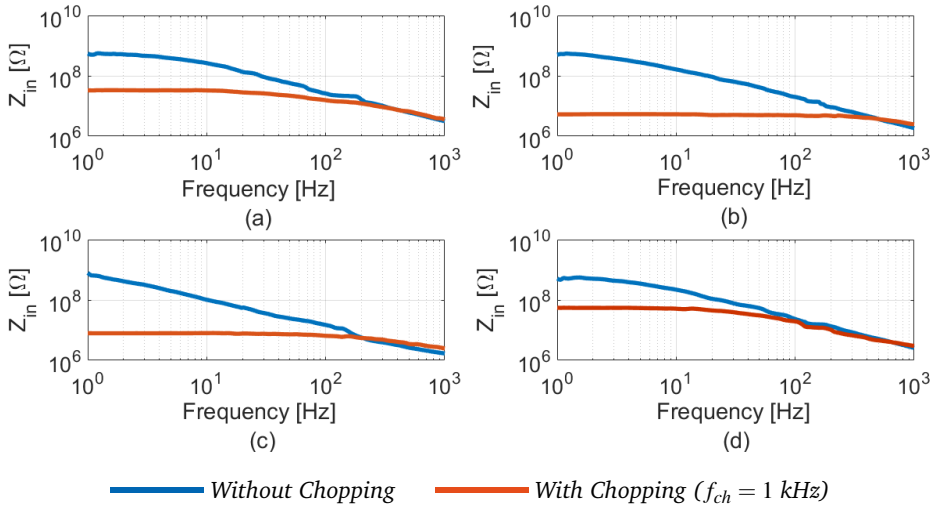
**Figure 3.5:** Input referred noise density of the different front-ends (a) FE-I, (b) FE-II, (c) FE-III and (d) FE-IV.

Figure 3.5 represents the input referred noise spectral density of the front-ends discussed, with choppers deactivated (in blue), and activated (in red). Figure 3.5(a) shows the input noise density of FE-I (based on the diode-connected load amplifier). The input noise density without chopping shows a  $1/f$  behaviour start-

ing from  $147 \mu\text{V}/\sqrt{\text{Hz}}$  at 1 Hz and reaching  $5 \mu\text{V}/\sqrt{\text{Hz}}$  at 1 kHz. When chopping at 1 kHz is applied, the noise spectral density becomes almost flat with a floor of around  $14 \mu\text{V}\sqrt{\text{Hz}}$  until 1 kHz (Figure 3.5(a), red line). The total equivalent input referred integrated noise in a bandwidth of 1–200 Hz with chopping at 1 kHz is  $176.9 \mu\text{V}_{rms}$ . Figure 3.5(b) shows the input noise density of FE-II (based on a diode-connected load amplifier with large input devices). As expected, the noise density without chopping (blue line) follows the same trend as in the previous case, but with a 2.5x reduction in the noise, thanks to increased area of the input pair. In this case, the input noise density without chopping is  $58 \mu\text{V}/\sqrt{\text{Hz}}$  at 1 Hz reducing to around  $2 \mu\text{V}/\sqrt{\text{Hz}}$  at 1 kHz. The total equivalent input referred integrated noise of FE-II in a bandwidth of 1–200 Hz with chopping at 1 kHz is  $51.2 \mu\text{V}_{rms}$  (Figure 3.5(b), red line).

Figure 3.5(c) shows the input noise spectral density of FE-III, built with the modified diode-connected load amplifier. The noise spectral density at 1 Hz is  $92.4 \mu\text{V}/\sqrt{\text{Hz}}$ . The application of 1 kHz chopping results in a total equivalent input referred integrated noise of  $29.2 \mu\text{V}_{rms}$  in a bandwidth of 1–200 Hz. The improved noise behaviour offered by the modified diode-connected load amplifier compared to the normal diode-connected load amplifiers is due to the 10x larger size of the input pair. The last plot, Figure 3.5(d), shows the input noise spectral density of FE-IV, based on the bootstrapped load amplifier. The measurement without chopping shows a trend decreasing in frequency until the lower cut off frequency of 185 Hz and almost a flat floor of  $15 \mu\text{V}/\sqrt{\text{Hz}}$  till the upper cut off frequency of 3.3 kHz. The total equivalent input referred noise integrated in a bandwidth of 400–600 Hz (a 200 Hz bandwidth in the maximum gain region for comparison with the other FEs), applying chopping at 1 kHz, is  $34.7 \mu\text{V}_{rms}$ .

Figure 3.6 shows the input impedance vs frequency for the presented front-ends with (red line) and without (blue line) chopping. Figures 3.6(a) and (b) show the input impedance plots of FE-I and FE-II, respectively. The input impedance of the version 1 diode-connected load amplifier at 1 Hz in absence of chopping is 540



**Figure 3.6:** Input impedance of the different front-ends (a) FE-I, (b) FE-II, (c) FE-III and (d) FE-IV.

$M\Omega$  while application of 1 kHz chopping reduces the input impedance to  $33.1 M\Omega$ . In case of the version 2 diode-connected load amplifier, the input impedance at 1 Hz reduces from  $499 M\Omega$  to  $5.3 M\Omega$  with the application of chopping at 1 kHz, which is expected due to the large input pair and its large parasitic capacitance. Figure 3.6(c) shows the input impedance vs frequency plot of the modified diode-connected load FE-III. In this case, the input impedance at 1 Hz reduces from  $791 M\Omega$  to  $7.9 M\Omega$  with the application of chopping at 1 kHz, owing to the large parasitic capacitance due to Miller effect and due to the large input pair. The last plot of Figure 3.6(d) shows the input impedance versus frequency for FE-IV. The input impedance at 1 Hz without chopping is  $508 M\Omega$ , which decreases to  $55.3 M\Omega$  when chopping at 1 kHz is applied. In this front-end, the input impedance after chopping is better compared to the other cases thanks to the PFL impedance boosting.

All the parameters measured in the front-ends presented in this work are summarized in Table 3.2 along with a comparison with the state-of-the-art bio-signal front-ends in similar flexible technologies, where the three main performance indicators: PEF, area, and input impedance are highlighted. These three parameters

which, as explained in Section 3.4, are in trade-off, are also shown in a radar plot in Figure 3.7 for the front-ends discussed here. As the best PEF is the lowest, the PEF axis is plotted in inverse order, so that the best front-end would cover the largest surface in the radar plot. For the sake of comparison, one should remember that FE-I, FE-II and FE-III use external discrete capacitors.

Clearly, FE-I with the cascaded diode-connected load amplifier version 1 has the worst PEF performance, while FE-II and FE-III, with diode-connected load version 2 and modified diode-connected load amplifier respectively, are similar. In fact, the former has a higher noise (due to the fact that its gain is divided in two cascaded stages and thus more TFTs contribute to noise) but lower power consumption compared to the latter (which stacks many TFTs between the rails and thus needs larger supply voltage).

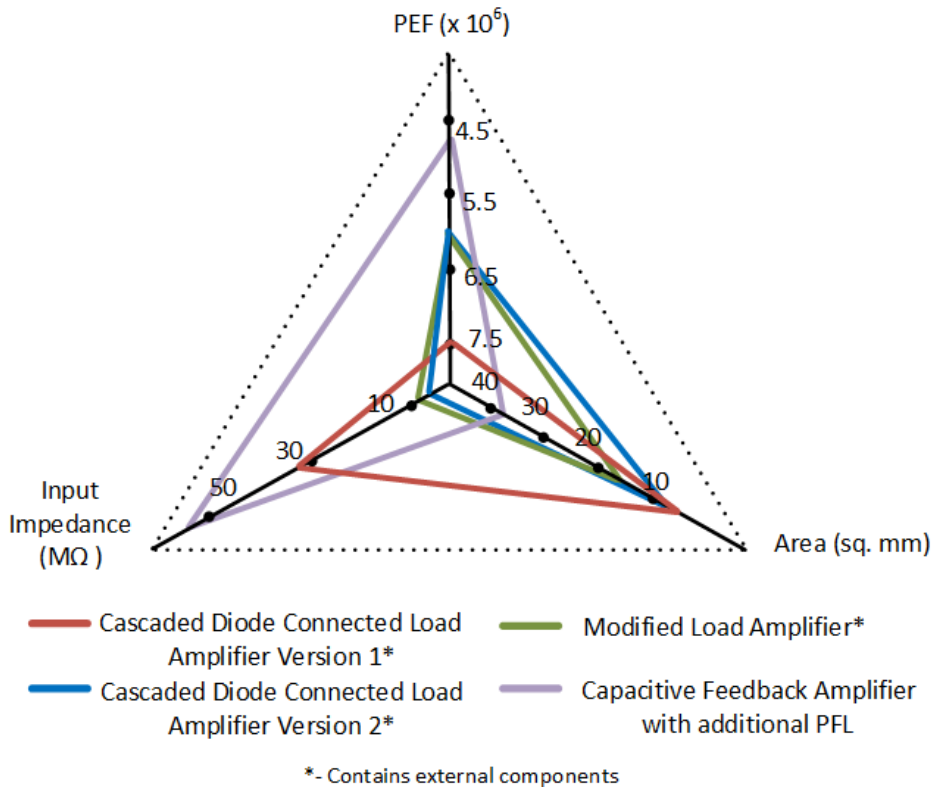


**Figure 3.7:** Performance comparison of the presented front-ends.

The capacitive feedback FE-IV with input impedance boosting and bootstrapped amplifier achieves the best PEF. This is due to the fact that the bootstrapped amplifier provides high maximum gain in one stage (minimizing the noise contributions of the TFTs after the input pair) using only two stacked TFTs, and thus with no need for a high voltage supply. When it comes to input impedance, FE-IV with the capacitive feedback amplifier with impedance boosting again demonstrates the best performance, thanks to the impedance-boosting positive feedback technique employed, albeit, at the expense of area for the positive feedback network. It should be noted that the use of positive feedback in a technology that suffers from high parametric variability requires extra attention to stability issues. The area consumption of FE-IV is exacerbated by the use of the bootstrapped amplifier, which needs large capacitors  $C_B$  (1 nF) to shorten gate and source of the load TFT at the signal frequency. Still, this FE is the only one which is fully integrated on foil. The other FEs need external discrete capacitors to implement  $C_{in}$ . Finally, our work is compared to relevant the state-of-the-art bio-signal measurement solutions implemented on foil [2, 13, 14, 15] and listed in Table 3.2. The NEF measured in our front-ends is in line with other a-IGZO references, while the NEF of [2] is better thanks to the lower  $1/f$  noise offered by that technology. The PEF of our front-ends is actually lower than the one reported in all previous art. FE-III achieves this result exploiting a moderate supply voltage and a design that reduces  $1/f$  noise by increasing the size of the input devices. FE-II and FE-IV use an even lower power supply (enabled by the simple structure of the amplifiers used in these FEs) and a noise-optimized sizing of the input TFTs. Also, all our FEs use a limited bias current, as their thermal noise is not dominant, and benefit from the better mobility of a-IGZO compared to the technologies used in [2] and [13].

### 3.7 Conclusions

For applications where area is not a critical factor because only few bio-signal measurement channels are required, the capacitive feedback architecture with impedance boosting based on the bootstrapped load amplifier represents an attractive solution, due to better PEF and high input impedance. One of the obvious disadvantages of this solution is guaranteeing stability of the front-end in presence of variability and mismatch. However, when high resolution electrode matrices are necessary, the minimum required electrode pitch sets a strict requirement on area. In such applications, e.g. high resolution surface EMG, other options should be explored, like the front-ends II and III discussed in this Chapter. These front-ends, based on diode-connected load amplifiers with and without output impedance enhancement, should be carefully optimized for the noise, power and input impedance requirements, based on the characteristics of the flexible technology employed and based on the specifications of the envisaged application. Also, they need two discrete capacitors each, which might add to the cost and decrease the flexibility of the final solution. In conclusion, the diode-connected load amplifiers with cascaded stages offer a good compromise between performance and robustness. Hence, this topology has been chosen to be implemented in full system architectures, presented in the following Chapters of this thesis.

**Table 3.2:** Performance comparison of the presented front-ends with the state-of-the-art.

Parameter	This work				[2]	[13]	[14]	[15]
	FE- I	FE-II	FE-III	FE-IV				
Technology			a-IGZO		a-Si	DNTT	a-IGZO	a-IGZO
Amplifier maximum gain [dB]	22.9	26.9	25.2	22.8	20	27	22	24.9-23.1
Amplifier bandwidth	6.8 kHz	4 kHz	400 Hz	185 Hz-3.3 kHz	200 Hz	90 Hz	3 kHz	5.4 kHz-5.2 kHz
Chopping frequency [kHz]	1	1	1	1	5	-	0.5	5-8
Input referred noise [ $\mu V_{rms}$ ] with chopping (BW)	176.9 (1–200 Hz)	51.9 (1–200 Hz)	29.2(1–200 Hz)	34.7(400–600 Hz)	2.3(1–100 Hz)	-	92.5(1–200 Hz)	125–31.4 (1–500 Hz)
$Z_{in}$ with chopping [ $M\Omega$ ]	33.1	5.3	7.9	55.3	-	-	-	29.6-23
Bias current [ $\mu A$ ]	3.2	2.6	3.1	5.2	200	15	3.2	50
Supply voltage [V]	10	10	$\pm 13$	10	55	2	10	$\pm 13$
NEF	868.8	226.6	141.1	217.2	126.3	-	454.3	385.5 <sup>a</sup>
PEF	$7.5 \times 10^6$	$5.1 \times 10^5$	$5.1 \times 10^5$	$4.7 \times 10^5$	$8.7 \times 10^5$	-	$2.0 \times 10^6$	$3.8 \times 10^{6a}$
Area [ $mm^2$ ]	4.2	6.1	17.4	37.0	-	100.0	5.4	11.2
External components required	Yes	Yes	Yes	No	Yes	Yes	Yes	No

<sup>a</sup> Considering 31.4  $\mu V_{rms}$  in 500 Hz bandwidth.

## Bibliography

- [1] M. Zulqarnain, S. Stanzione, J.-L. P. J. van der Steen, G. H. Gelinck, S. Abdinia, and E. Cantatore, "Design trade-offs in amorphous indium gallium zinc oxide thin film transistor based bio-signal sensing front-ends," *Flexible and Printed Electronics*, vol. 4, p. 014001, Jan. 2019.
- [2] T. Moy, L. Huang, W. Rieutort-Louis, C. Wu, P. Cuff, S. Wagner, J. C. Sturm, and N. Verma, "An EEG acquisition and biomarker-extraction system using low-noise amplifier and compressive-sensing circuits based on flexible, thin-film electronics," *IEEE Journal of Solid-State Circuits*, vol. 52, pp. 309–321, Jan. 2017.
- [3] J. G. Webster, *Medical Instrumentation: Application and Design*. New York: John Wiley & Sons, 4th ed., 2009.
- [4] M. Steyaert, W. Sansen, and C. Zhongyuan, "A micropower low-noise monolithic instrumentation amplifier for medical purposes," *IEEE Journal of Solid-State Circuits*, vol. 22, pp. 1163–1168, Dec. 1987.
- [5] R. Muller, S. Gambini, and J. M. Rabaey, "A 0.013 mm<sup>2</sup>, 5  $\mu$ W, DC-coupled neural signal acquisition IC with 0.5 V supply," in *2011 IEEE International Solid-State Circuits Conference*, IEEE, Feb. 2011.
- [6] M. Rojas-Martínez, M. A. Mañanas, and J. F. Alonso, "High-density surface EMG maps from upper-arm and forearm muscles," *Journal of NeuroEngineering and Rehabilitation*, vol. 9, no. 1, p. 85, 2012.
- [7] M. Gavaret, L. Maillard, and J. Jung, "High-resolution EEG (HR-EEG) and magnetoencephalography (MEG)," *Neurophysiologie Clinique/Clinical Neurophysiology*, vol. 45, pp. 105–111, Mar. 2015.
- [8] R. Harrison and C. Charles, "A low-power low-noise CMOS amplifier for neural recording applications," *IEEE Journal of Solid-State Circuits*, vol. 38, pp. 958–965, June 2003.
- [9] T. Denison, K. Consoer, W. Santa, A.-T. Avestruz, J. Cooley, and A. Kelly, "A 2  $\mu$ W 100 nV/ $\sqrt{Hz}$  chopper-stabilized instrumentation amplifier for chronic measurement

- of neural field potentials,” *IEEE Journal of Solid-State Circuits*, vol. 42, pp. 2934–2945, Dec. 2007.
- [10] Q. Fan, F. Sebastiano, J. H. Huijsing, and K. A. A. Makinwa, “A 1.8  $\mu\text{W}$  60 nV/ $\sqrt{\text{Hz}}$  capacitively-coupled chopper instrumentation amplifier in 65 nm CMOS for wireless sensor nodes,” *IEEE Journal of Solid-State Circuits*, vol. 46, pp. 1534–1543, July 2011.
- [11] C. Garripoli, J.-L. P. van der Steen, F. Torricelli, M. Ghittorelli, G. H. Gelinck, A. H. V. Roermund, and E. Cantatore, “Analogue frontend amplifiers for bio-potential measurements manufactured with a-IGZO TFTs on flexible substrate,” *IEEE Journal on Emerging and Selected Topics in Circuits and Systems*, vol. 7, pp. 60–70, Mar. 2017.
- [12] H. Marien, M. S. J. Steyaert, E. van Veenendaal, and P. Heremans, “A fully integrated delta sigma ADC in organic thin-film transistor technology on flexible plastic foil,” *IEEE Journal of Solid-State Circuits*, vol. 46, pp. 276–284, Jan. 2011.
- [13] H. Fuketa, K. Yoshioka, Y. Shinozuka, K. Ishida, T. Yokota, N. Matsuhisa, Y. Inoue, M. Sekino, T. Sekitani, M. Takamiya, T. Someya, and T. Sakurai, “1  $\mu\text{m}$ -thickness ultra-flexible and high electrode-density surface electromyogram measurement sheet with 2 V organic transistors for prosthetic hand control,” *IEEE Transactions on Biomedical Circuits and Systems*, vol. 8, pp. 824–833, Dec. 2014.
- [14] M. Zulqarnain, S. Stanzione, J.-L. P. V. D. Steen, G. H. Gelinck, K. Myny, S. Abdinia, and E. Cantatore, “A 52  $\mu\text{W}$  heart-rate measurement interface fabricated on a flexible foil with a-IGZO TFTs,” in *ESSCIRC 2018 - IEEE 44th European Solid State Circuits Conference (ESSCIRC)*, IEEE, Sept. 2018.
- [15] C. Garripoli, S. Abdinia, J.-L. J. P. van der Steen, G. H. Gelinck, and E. Cantatore, “A fully integrated 11.2 mm<sup>2</sup> a-IGZO EMG front-end circuit on flexible substrate achieving up to 41 dB SNR and 29 M $\Omega$  input impedance,” *IEEE Solid-State Circuits Letters*, vol. 1, pp. 142–145, June 2018.



# Chapter 4

## A Heart-Rate Measurement Interface on a Flexible Foil

*This Chapter deals with two time based interfaces based on a reset integrator, for bio-signal acquisition using a-IGZO TFTs. The initial part of the Chapter presents a heart-rate measurement interface for wearable applications, fabricated on a flexible foil, that requires a moderate SNR (as low as 6 dB). The output is provided as a PWM waveform. Voltage to pulse-width conversion is achieved with a simple and power minimalistic approach, using a reset integrator.*

*This approach can be further refined to serve applications that are more demanding in terms of SNR. In the later part of this Chapter, SNR is improved by applying correlated double sampling (CDS) to enable ECG monitoring. A low power flexible ECG interface incorporating CDS has been studied in simulations.*

*The contents of this Chapter have been published in ESSCIRC 2018 [1] and IWASI 2019 [2] conference proceedings.*

## 4.1 Introduction

Wearable electronic devices are gaining a growing research interest and popularity. Wearable devices should be flexible and conformable to the human body, to increase user comfort. Amorphous Indium Gallium Zinc Oxide (a-IGZO) Thin Film Transistors (TFTs) technologies are very suitable platforms to develop electronic devices for these kind of applications due their flexibility, robustness to mechanical stress and low manufacturing cost.

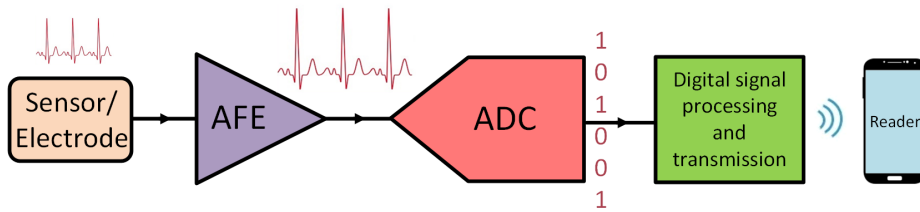


*Figure 4.1: General bio-signal acquisition system architecture.*

Figure 4.1 shows the general architecture of a bio-signal acquisition system. The system typically consists of a sensor/electrode, an analogue front-end (AFE), an analogue to digital converter (ADC), a digital signal processing and transmission block, and a reader. The sensor/electrode converts an external analogue quantity into either a current or a voltage signal. The output signal of the sensor/electrode is generally low in amplitude, hence, it is amplified through an AFE. Conversion to digital representation is essential before transmitting signals to a reader device (e.g. smart phone), to increase noise immunity during transmission. This analogue-to-digital conversion and transmission process is performed by an ADC and a digital signal processing and transmission block.

In Chapter 3, we have already discussed analogue front-ends. This Chapter deals with conversion of an input signal to a binary pulse width modulated (PWM) representation, which can further be quantised in time to get a digital representation (to be discussed in Chapter 5). In Silicon-based bio-signal acquisition systems, the digitization of the input data is generally done in the voltage domain, as stable

voltage references are available. But, it is difficult to make a voltage reference in a-IGZO at the state-of-the-art. Hence, we prefer to digitize the input data in time domain, as a time reference can be easily generated in a-IGZO [3], for instance based on a received NFC carrier. Besides, in this technology, the time domain conversion of an analogue signal to the digital representation is much simpler to implement than the voltage domain conversion. Thus, after the AFE, a reset integrator is used to transform the signal amplitude in duty cycle information i.e. PWM representation. The binary PWM representation can be transformed to a digital representation by counting the number of clock cycles the integrator output is high every period (to be discussed in Chapter 5).

Bio-signal acquisition systems designed and fabricated using flexible TFT technologies have been presented in [4, 5] but the signals in these works are not digitized within the system on foil. Moreover, the power consumption reported in [4] is 11 mW, which is quite high for wearable applications. The input signal is transformed to analogue PWM representation in [6] but power consumption is still 2 mW, and the circuit does not provide a voltage, but a current input, making it inconvenient to measure bio-potentials. In this Chapter, the analogue output from a voltage-sensitive front-end is converted to an analogue PWM representation with low power consumption and using a hardware minimalistic approach.

The rest of the Chapter is organized as follows: In Section 4.2, an introduction to the reset integrator is provided, together with the experimental characterization of a first implementation. Section 4.3 discusses the system architecture and circuit design of the heart-rate measurement interface on flexible foil, that is based on the reset integrator circuit, and presents its experimental measurement results including *in-vivo* characterization. Section 4.4 presents an improved version of the previous system with better noise performance, analyzing its performance through simulations. Finally, Section 4.5 concludes the Chapter.

## 4.2 Single slope reset integrator

### 4.2.1 Principle of operation

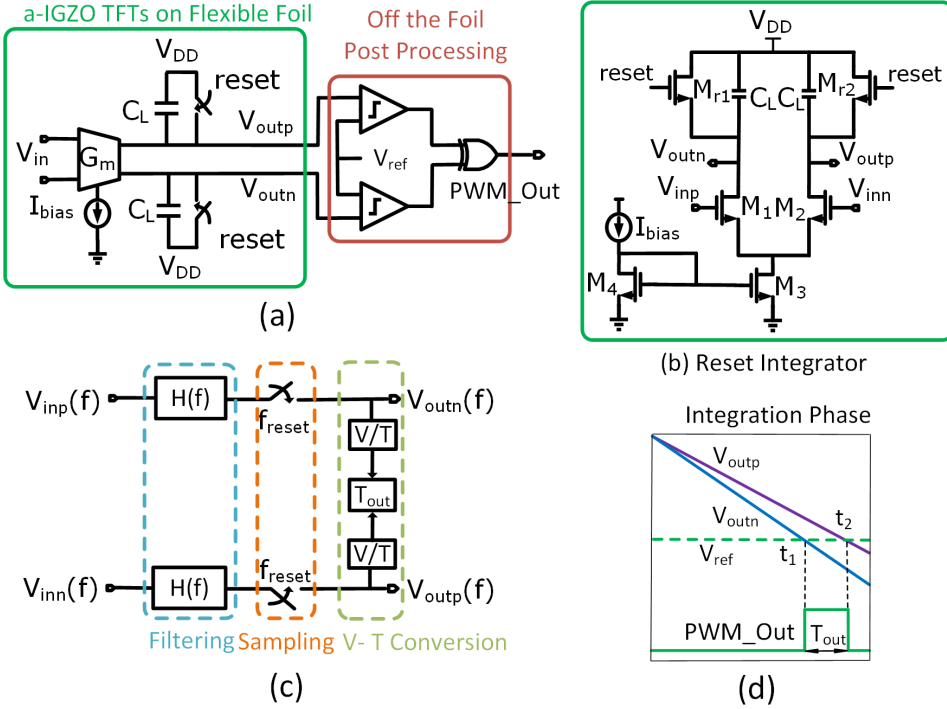


**Figure 4.2:** (a) Architecture of the single slope reset integrator, (b) Circuit schematic of the single slope reset integrator, (c) Functionality of the reset integrator in terms of signal processing operations, (d) Principle of operation.

The unavailability of active loads in unipolar technologies, as discussed in Chapter 1, motivated us to investigate a switched capacitor load in this technology. The basic idea is shown in Figure 4.2. Figure 4.2(a) shows the conceptual schematic of a reset integrator, which uses a switched capacitor load. The circuit schematic is presented in Figure 4.2(b), while the principle of operation is shown in Figure 4.2(d). The output drain currents are integrated on load capacitors  $C_L$  during the integration phase. The moments in which the integrator outputs ( $V_{outn}$ ,  $V_{outp}$ ) are discharged below a given threshold  $V_{ref}$  can be detected by comparators. The integrator outputs are periodically reset to  $V_{DD}$ . The time delay in threshold crossing

between both branches of the integrator output,  $T_{out}$ , is proportional to the input signal. Thus, the reset integrator circuit transforms a voltage input signal ( $V_{in}$ ) to a PWM output signal ( $T_{out}$ ).

The voltage to pulse width conversion produces a PWM waveform which can have variable pulse widths depending on the sampled input signal with a fixed sampling frequency. Hence, the output PWM representation is a continuous-amplitude version of the input signal, but sampled in time. So, the output PWM representation discussed in this Chapter is still not a digital representation. The sampling in the integrator will result in aliasing but, as there is no digitization, there will be no quantization noise.

The basic operation of the reset integrator can be represented by three subsequent signal processing operations as shown in Figure 4.2(c): filtering due to integration of the signal current within a integration period, followed by output voltage sampling at a rate  $f_{reset}$  and finally voltage to time conversion.

Assuming ideal integration of the input currents on the load capacitors ( $C_L$ ), the time-domain output voltage of the reset integrator at the  $n^{th}$  sampling moment (considering  $G_m$  as the transconductance,  $f_{reset} = f_s = 1/T_s$  and integration time =  $T_{int}$ ) can be written as:

$$V_{out}(t = nT_s) = V_{DD} - \frac{1}{C_L} \cdot \int_{nT_s - T_{int}}^{nT_s} I_{int}(\tau) d\tau = V_{DD} - \frac{G_m}{C_L} \cdot \int_{nT_s - T_{int}}^{nT_s} V_{in}(\tau) d\tau \quad (4.1)$$

The integration of current samples within an integration window results in a sinc LPF response as shown in Figure 4.3. The ideal magnitude transfer function of this response can be expressed as:

$$H(f) = \left| \frac{V_{out}(f)}{V_{in}(f)} \right| = \frac{G_m}{C_L} \left| \frac{\sin(\pi f T_{int})}{\pi f} \right| \quad (4.2)$$

As shown in Figure 4.3, the periodic integration of the current produces notches in the frequency response, which are at multiples of the inverse of the integration

period ( $1/T_{int}$ ). It can be seen that with equal -3 dB bandwidths and equal voltage gains, the sinc lowpass response attenuates out of band frequency components more than a first order RC lowpass response. The ideal -3 dB bandwidth of the low-pass sinc response is approximately  $0.44/T_{int}$  [7]. It should be noted that the -3 dB bandwidth in this case is ideally determined only by  $T_{int}$ .

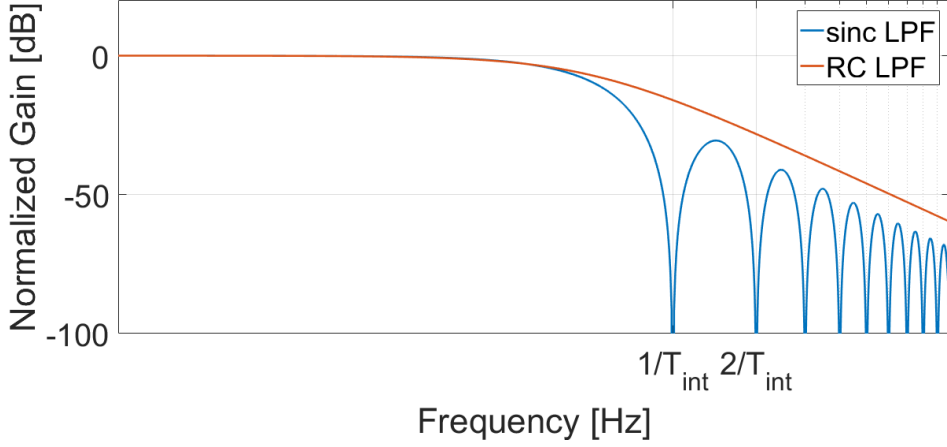


**Figure 4.3:** Comparison of sinc LPF response with RC LPF response.

The relationship between  $T_{out}$  and  $V_{in}$  can be obtained as (Figure 4.2(d)):

$$V_{outn} = V_{DD} - \frac{\frac{I_{bias}}{2} + \frac{g_m V_{in}}{2}}{C_L} t_1 \quad (4.3)$$

$$V_{outp} = V_{DD} - \frac{\frac{I_{bias}}{2} - \frac{g_m V_{in}}{2}}{C_L} t_2 \quad (4.4)$$

$$\text{At } V_{ref} : V_{outn} = V_{outp} = V_{ref} \quad (4.5)$$

$$V_{DD} - \frac{\frac{I_{bias}}{2} + \frac{g_m V_{in}}{2}}{C_L} t_1 = V_{DD} - \frac{\frac{I_{bias}}{2} - \frac{g_m V_{in}}{2}}{C_L} t_2 \quad (4.6)$$

$$\frac{I_{bias}}{2} (t_2 - t_1) = \frac{g_m V_{in}}{2} (t_1 + t_2) \quad (4.7)$$

Considering,  $CV = It$  and taking the average of  $t_1$  and  $t_2$ , we obtain:

$$C_L (V_{DD} - V_{ref}) = \frac{I_{bias}}{2} \left( \frac{t_1 + t_2}{2} \right) \quad (4.8)$$

$$t_1 + t_2 = \frac{4C_L}{I_{bias}} (V_{DD} - V_{ref}) \quad (4.9)$$

Using the value of  $t_1 + t_2$  from Equation 4.9 in Equation 4.7, we can write:

$$\frac{T_{out}}{V_{in}} = \frac{4g_m C_L (V_{DD} - V_{ref})}{I_{bias}^2} \quad [\text{s/V}] \quad (\text{where, } T_{out} = t_2 - t_1) \quad (4.10)$$

where  $T_{out}$  is the output pulse width,  $V_{in}$  is the differential input signal,  $g_m$  is the transconductance of the input transistor in the integrator,  $C_L$  is the load capacitor,  $V_{DD}$  is the supply voltage of the integrator and  $I_{bias}$  is the tail bias current in the integrator. It should be noted that Equation 4.10 is only valid in pass-band, as the input is assumed to be constant.

The presented idea is inspired by the integrating amplifier (dynamic amplifier) introduced in [8], which has become very popular in the last 10 years especially in the application as a residue amplifier for ADCs. A differential dynamic amplifier using a common-mode voltage detection technique is proposed in [9], with further improvements in [10, 11, 12, 13, 14, 15]. However, all of the mentioned approaches used the dynamic amplifier in the voltage domain only, while we use it as a voltage to pulse width converter.

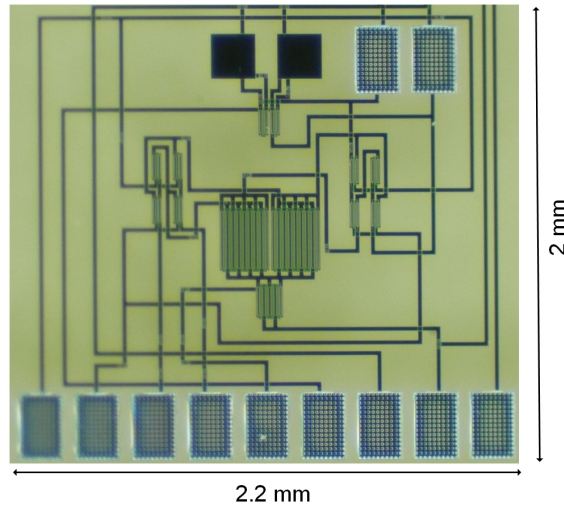
### 4.2.2 Circuit characterization

This Section presents measured results of the single slope reset integrator. Figure 4.4 shows the micrograph of the single slope reset integrator. The total area of the circuit on foil is 4.4 mm<sup>2</sup>. Table 4.1 depicts some design parameters of the circuit shown in Figure 4.2(b). Figure 4.5 shows the linear relationship between  $T_{out}$  and  $V_{in}$ . Figure 4.6 shows the residual error in  $T_{out}$  with respect to a linear fit.

**Table 4.1:** Circuit parameters of the single slope reset integrator

Parameter	Value
$\left(\frac{W}{L}\right)_{M_1, M_2} \left[\frac{\mu m}{\mu m}\right]$	$\frac{2000}{15}$
$\left(\frac{W}{L}\right)_{M_{r1}, M_{r2}} \left[\frac{\mu m}{\mu m}\right]$	$\frac{100}{15}$
$\left(\frac{W}{L}\right)_{M_3} \left[\frac{\mu m}{\mu m}\right]$	$\frac{500}{15}$
$V_{DD}$ [V]	10
$C_L$ [pF]	10
$I_{bias}$ [ $\mu A$ ]	5.5

It can be observed that this error is less than  $\pm 2 \mu s$  in a  $\pm 150 mV$  input range. The time domain gain as expressed in Equation 4.10 is  $0.59 ms/V$ , while the measured gain is  $0.5 ms/V$ . Figure 4.7 shows the variation of gain with change in  $V_{ref}$ . It can be observed that the analytical variation in gain with change in  $V_{ref}$  closely matches with the measured variation in gain with change in  $V_{ref}$ . Figure 4.8 shows the histogram of the output jitter measured from the circuit in absence of an input signal. The total output rms jitter is  $0.76 \mu s$ , which translates to  $1.5 mV_{rms}$  input referred noise. As, it can be seen, this integrated noise is not suitable for practical applications, thus, gain stages should be added before the reset integrator.

**Figure 4.4:** Micrograph of the single slope reset integrator on foil.

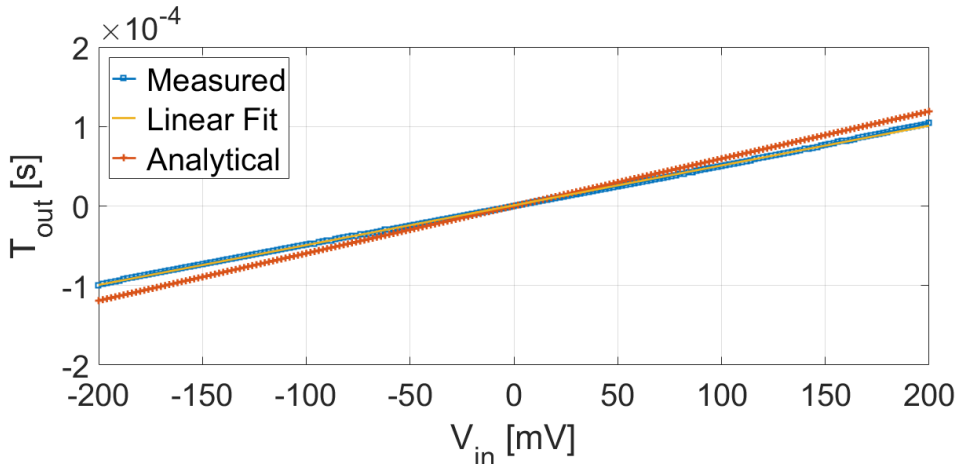


*Figure 4.5: DC transfer characteristics.*

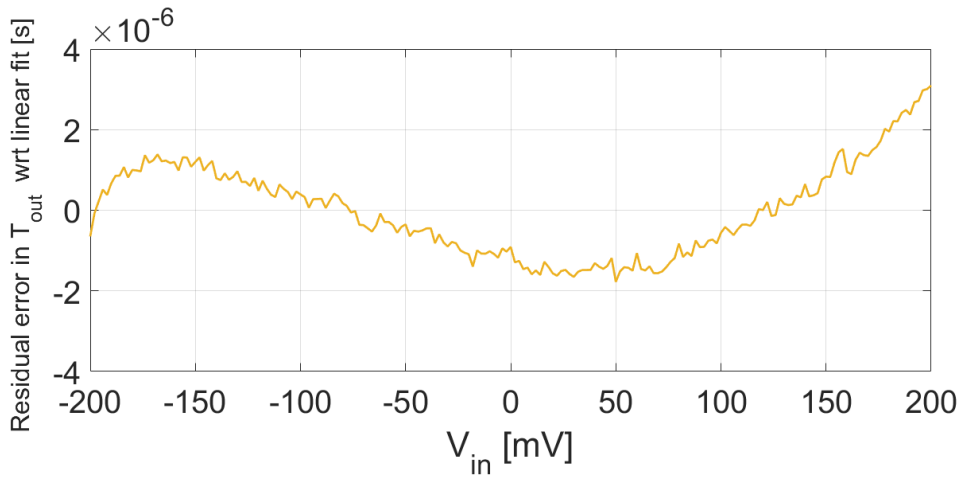


*Figure 4.6: Residual error in measured  $T_{out}$  with respect to linear fit.*

## 4.3 Heart-rate measurement interface

### 4.3.1 System architecture

The architecture of the heart-rate (HR) measurement interface which is developed based on the idea of the reset integrator is shown in Figure 4.9. The analogue front-end is integrated on foil using a-IGZO ESL TFT technology. It consists of an

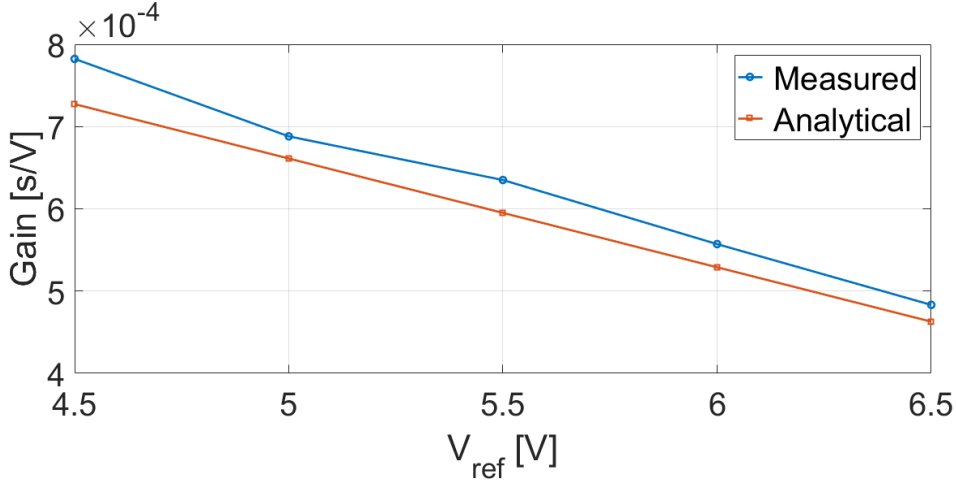


Figure 4.7: Variation of gain with  $V_{ref}$ .

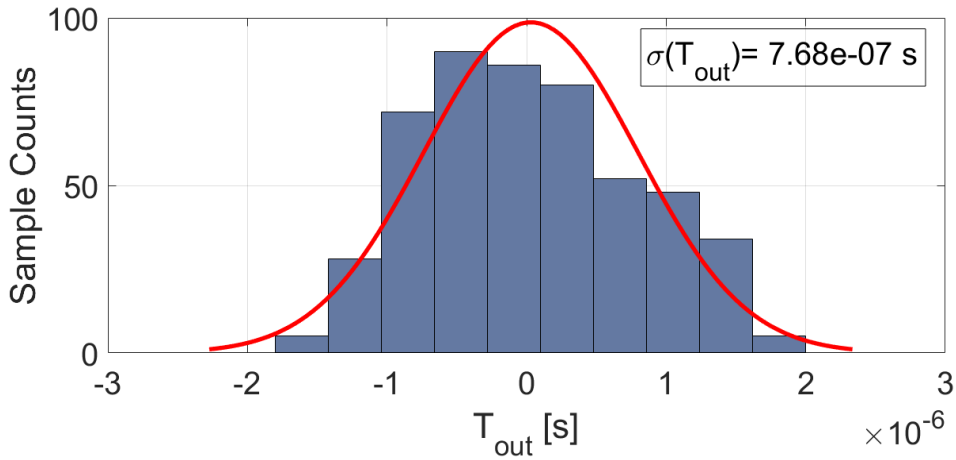


Figure 4.8: Measured output jitter.

input chopper, a 2-stage preamplifier featuring two cascaded diode-connected load differential gain stages and a reset integrator with de-chopper (Figure 4.9). The input signal of the conditioning chain is AC-coupled with discrete components before the input chopper ( $R_{in} = 1\text{ M}\Omega$  and  $C_{in} = 4.7\text{ }\mu\text{F}$ ). The output of the preamplifier is fed to the reset integrator, where the signal current discharges the load capacitors. The moments in which the integrator outputs are discharged below a given threshold  $V_{ref}$  is detected by two comparators. The time delay in threshold crossing between both branches of the integrator output,  $T_{out}$ , is proportional to the input

signal. The comparator outputs are then fed to an XOR to obtain a PWM output having a pulse width equal to  $T_{out}$  (and thus proportional to the differential input signal), with an additional sign bit, that provides information on which of the two signals crossed the reference voltage first.

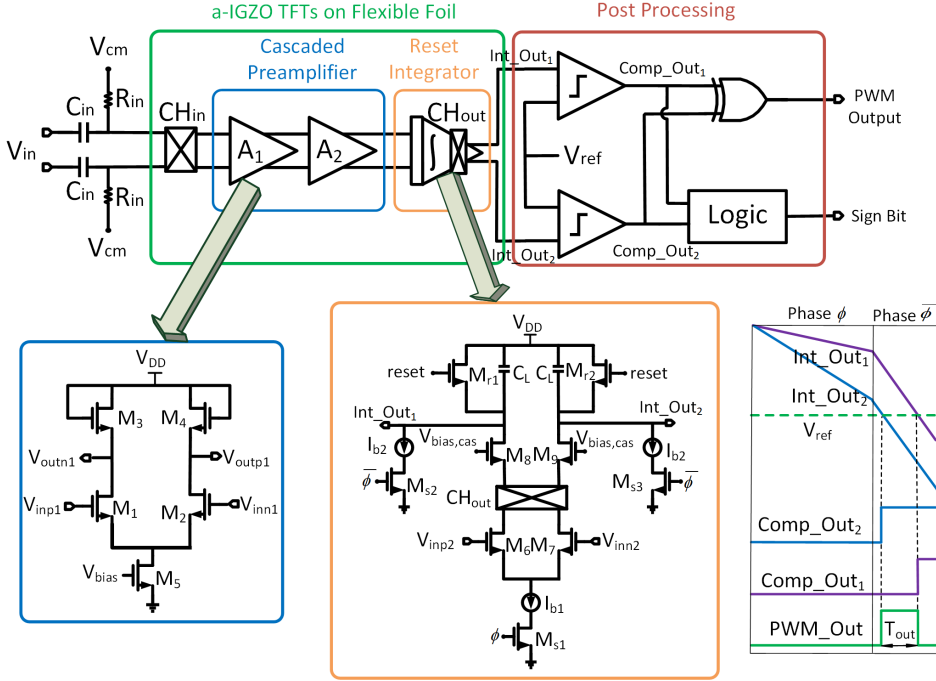
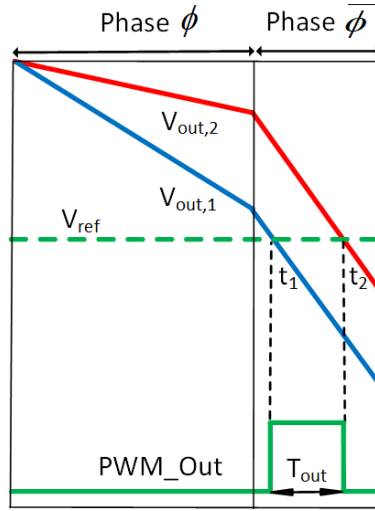


Figure 4.9: General system architecture.

### 4.3.2 Circuit design

The preamplifier is a conventional diode-connected load differential gain stage (Figure 4.9). Two stages are cascaded to obtain higher gain and lower input referred noise. The input TFTs in the preamplifier have large area ( $60000 \mu m^2$ ) to reduce the  $1/f$  noise. Chopping at 500 Hz is also used to mitigate the effect of  $1/f$  noise. The reset integrator (Figure 4.9) consists of a differential input pair, output chopper and load capacitors  $C_L$ , and includes cascode transistors to enable de-chopping on low-impedance nodes. In the first phase  $\phi$ , which will be called as the integration phase, a signal-dependent discharging of the output capacitors

occurs via the differential pair, while in the second phase  $\bar{\phi}$ , a constant current discharging takes place, as shown in Figure 4.9. If only an integration phase would be used for the voltage to pulse width conversion, then the comparator delay would be different for different input slopes, and this would result in non-linearity in the voltage to pulse width conversion. This effect is removed by adding the constant slope phase  $\bar{\phi}$ . The delay between the moments in which the two outputs reach the same voltage level (and thus the duration of the output pulse produced by the XOR,  $T_{out}$ ) is proportional to the differential input voltage. This technique has an obvious penalty of reduced gain due to lesser integration time. The relationship between  $T_{out}$  and input voltage can be derived, by inspection of Figure 4.10, as follows:



**Figure 4.10:** Principle of operation.

During the integration phase (phase  $\phi$ ):

$$v_{out1,\phi} = V_{DD} - \frac{\frac{I_{b1}}{2} + \frac{g_m v_{in}}{2}}{C_L} \phi \quad (4.11)$$

$$v_{out2,\phi} = V_{DD} - \frac{\frac{I_{b1}}{2} - \frac{g_m v_{in}}{2}}{C_L} \phi \quad (4.12)$$

During the constant current discharge phase (phase  $\bar{\phi}$ ):

$$\text{At } V_{ref} : v_{out_{1,\bar{\phi}}} = v_{out_{2,\bar{\phi}}} = V_{ref} \quad (4.13)$$

$$v_{out_{1,\bar{\phi}}} = v_{out_{1,\phi}} - \frac{I_{b2}t_1}{C_L} \quad (4.14)$$

Using value of  $v_{out_{1,\phi}}$  from Equation 4.11 in Equation 4.14, we obtain:

$$V_{ref} = V_{DD} - \frac{\frac{I_{b1}}{2} + \frac{g_m v_{in}}{2}}{C_L} \phi - \frac{I_{b2}t_1}{C_L} \quad (4.15)$$

$$\frac{I_{b2}t_1}{C_L} = V_{DD} - V_{ref} - \frac{\frac{I_{b1}}{2} + \frac{g_m v_{in}}{2}}{C_L} \phi \quad (4.16)$$

$$t_1 = \frac{C_L}{I_{b2}} \left[ V_{DD} - V_{ref} - \frac{\frac{I_{b1}}{2} + \frac{g_m v_{in}}{2}}{C_L} \phi \right] \quad (4.17)$$

Similarly, we can express  $t_2$  as:

$$t_2 = \frac{C_L}{I_{b2}} \left[ V_{DD} - V_{ref} - \frac{\frac{I_{b1}}{2} - \frac{g_m v_{in}}{2}}{C_L} \phi \right] \quad (4.18)$$

$$t_2 - t_1 = \frac{g_m v_{in}}{I_{b2}} \phi \quad (4.19)$$

$$\frac{T_{out}}{v_{in}} = \frac{g_m \phi}{I_{b2}} \quad [\text{s/V}] \quad (\text{where, } T_{out} = t_2 - t_1) \quad (4.20)$$

where  $T_{out}$  is the output pulse width,  $v_{in}$  is the differential input signal,  $g_m$  is the transconductance of the input transistor in the integrator,  $\phi$  is the integration period and  $I_{b2}$  is the discharging current during the phase  $\bar{\phi}$ .

The first design parameter to be chosen is the reset frequency, which is similar to the sampling frequency of an ADC, and is dictated by the application. Then, from

**Table 4.2:** Optimized design parameters of the system shown in Figure 4.9

Parameter	Value
$\left(\frac{W}{L}\right)_{\text{Input pair of } A_1} \left[\frac{\mu\text{m}}{\mu\text{m}}\right]$	$\frac{4000}{15}$
$\left(\frac{W}{L}\right)_{\text{Input pair of Integrator}} \left[\frac{\mu\text{m}}{\mu\text{m}}\right]$	$\frac{2000}{15}$
$V_{DD}$ [V]	10
$C_L$ [pF]	100
Reset frequency [Hz]	250
Reset duration [ $\mu\text{s}$ ]	200
Integration phase [ms]	1.8
Constant current discharge phase [ms]	1.8

Equation 4.20, we get the dependency of the other parameters. We would like to maximize the  $g_m/I_D$  ratio of the transistors in the integration phase, since the constant bias current in phase  $\phi$ ,  $I_{b1}$  does not carry information, while  $g_m$  amplifies the signal. So, it is a good choice to make  $W/L$  of these transistors large enough to bias them in subthreshold, resulting in  $W \gg L$ . In general, we would like to have the phase  $\phi$  (the integration phase) to last most of the time, but we need to make sure that during the phase  $\bar{\phi}$  (the constant current discharge phase), both the voltages cross the reference voltage  $V_{ref}$ . Then, the load capacitor (integrating capacitance),  $C_L$  is chosen in such a way to have the integration phase of the desired duration. In ideal conditions, the reset of the integrator should be instantaneous, as it does not bring any information, but since the switches have limited conductivity, the reset duration has to be chosen, so that the voltages settle to  $V_{DD}$ . The optimized design parameters are shown in Table 4.2.

### 4.3.3 Experimental results

#### Circuit characterization

Figure 4.11 shows the micrograph of the flexible foil integrating preamplifier and reset integrator. The total area of the circuits on foil is  $10.5 \text{ mm} \times 5 \text{ mm}$ . Figure 4.12

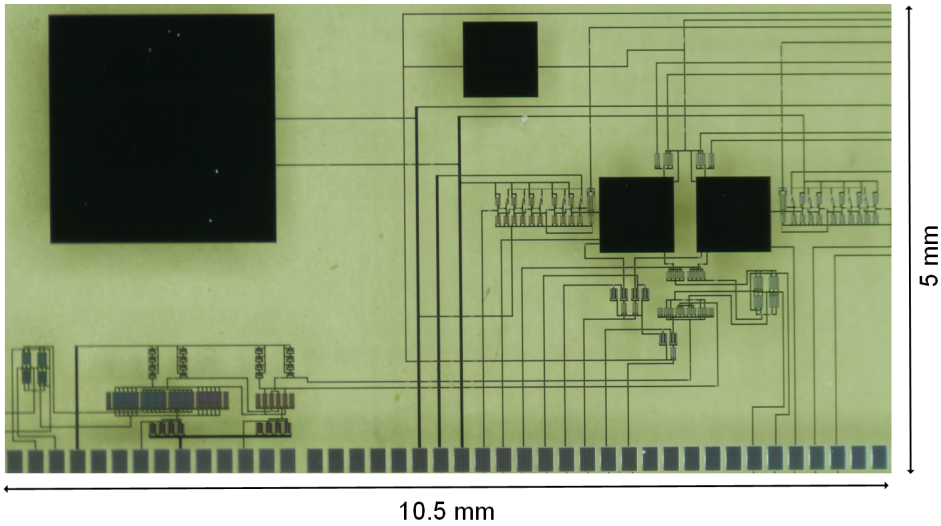


**Figure 4.11:** Micrograph of the preamplifier and reset Integrator on foil.

shows the measured frequency response of the cascaded preamplifier. It achieves a gain of 22 dB in a 3 kHz bandwidth with  $3.2 \mu\text{A}$  current consumption from a 10 V supply. The integrated input referred noise of the stand alone preamplifier is  $220.2 \mu\text{V}_{\text{rms}}$  without chopping and  $92.5 \mu\text{V}_{\text{rms}}$  with chopping at 500 Hz in a 1-200 Hz band. Figure 4.13 shows the CMRR of the cascaded preamplifier. The CMRR is 42 dB at 100 Hz with chopping at 500 Hz. Figure 4.14 shows the input impedance of the cascaded preamplifier. The input impedance is  $16.6 \text{ M}\Omega$  at 100 Hz without chopping and it reduces to  $6.6 \text{ M}\Omega$  at 100 Hz with chopping at 500 Hz. Figure 4.15 shows the transfer curve of the full chain, including the reset integrator. The low frequency gain is  $25 \text{ ms/V}$ . The notches appear at integer multiples of the inverse of the integration time. The integration period is 1.8 ms and hence the first notch appears at 555 Hz. Figure 4.16 shows the measured histogram of the output jitter for the full chain, in absence of an input signal. The total output rms jitter is  $4.79 \mu\text{s}$  while chopping at 500 Hz, which translates to  $186.3 \mu\text{V}_{\text{rms}}$  input referred noise for the full system. The increase in the input referred noise of the full system compared to the preamplifier can be explained by considering the effect of noise folding in the baseband due to periodic reset as well as the noise of the

reset integrator itself. The current consumption in the integrator during the first phase  $\phi$  is  $1 \mu A$  while in the phase  $\bar{\phi}$  it is  $1.5 \mu A$  in each branch. The total power consumption is  $52 \mu W$  with  $10 V$  supply voltage.

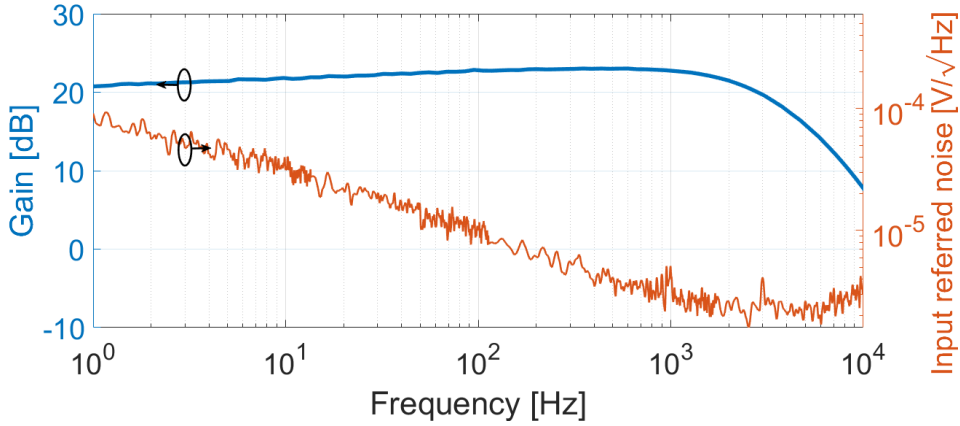


**Figure 4.12:** Measured preamplifier frequency response and input-referred noise.

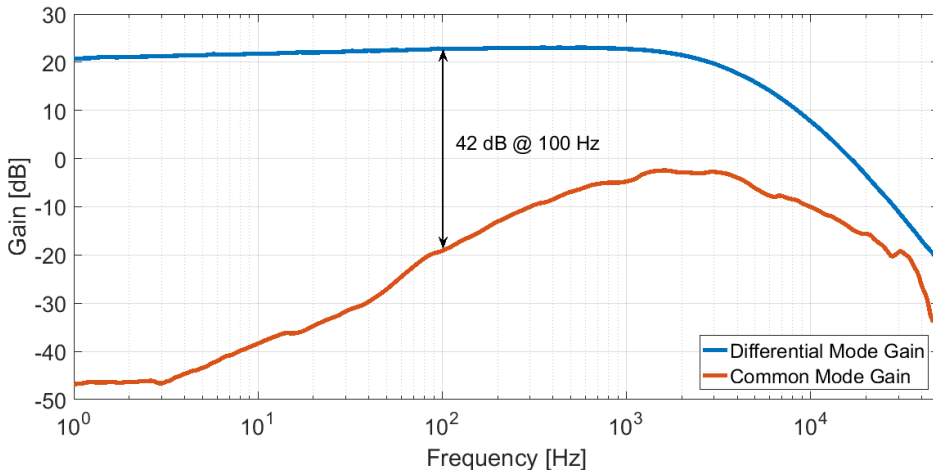


**Figure 4.13:** Measured CMRR of the preamplifier.

### Signal reconstruction

The signal is reconstructed in the voltage domain from the PWM output signal. The reset frequency and its harmonics are removed from the PWM output by low-pass filtering. Figure 4.17 shows the reconstruction of a  $20 mV_{pp}$  ECG signal applied

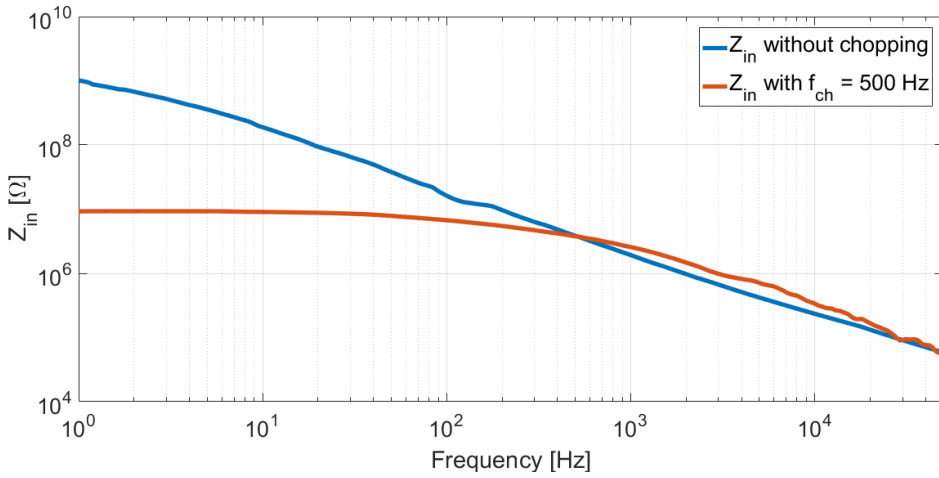


Figure 4.14: Measured input impedance of the preamplifier.

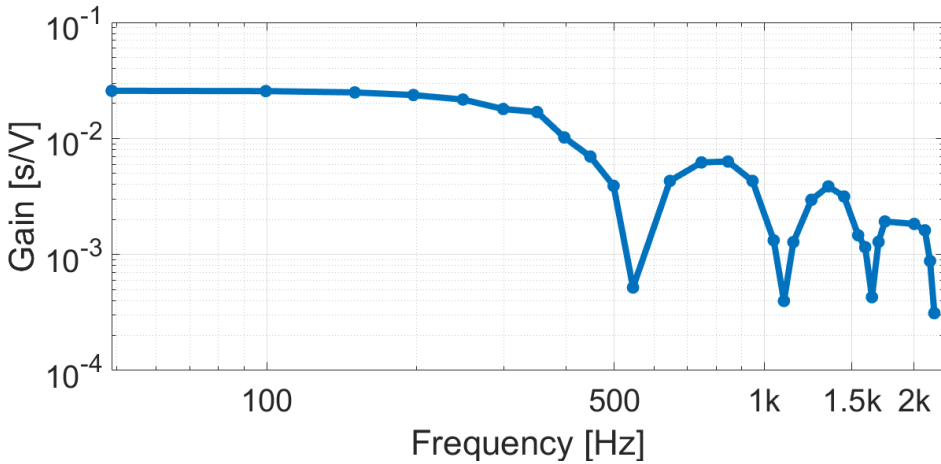
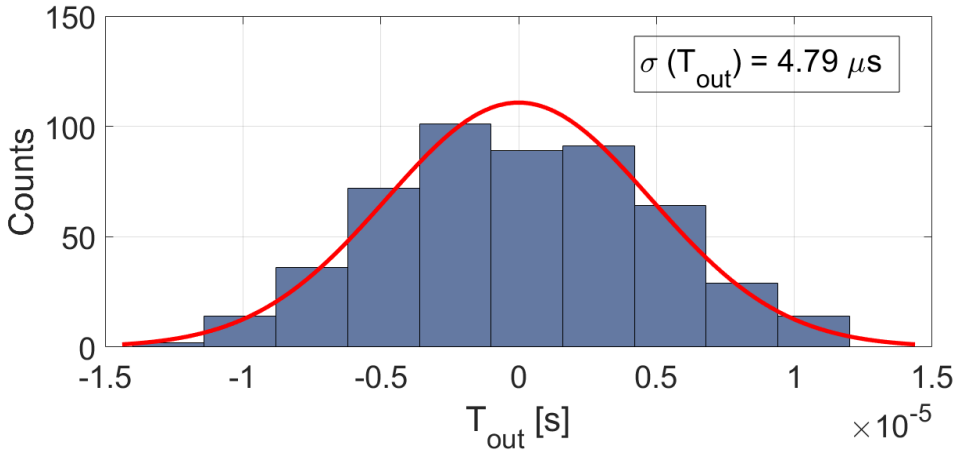


Figure 4.15: Measured frequency response of the full chain.

from a signal generator. A 200 Hz LPF is used to filter the reset frequency and its harmonics. As the amplitude of the input signal provided from the generator in this case is quite high, one can appreciate the QRS complex and PR and ST segments too, although corrupted by noise. However, to accurately measure ECG signals an integrated noise of  $20 \mu V_{rms}$  in 100 Hz bandwidth would be needed [16]. For this reason, the present circuit is only used to measure *in-vivo* heart-rate. For heart-rate, indeed, an SNR of even 6 dB is sufficient [17]. Assuming a typical cardiac signal amplitude of 1 mV, the SNR provided by this circuit is sufficient to measure



**Figure 4.16:** Measured output jitter in absence of an input signal.

HR. The signal bandwidth is further reduced to 10 Hz, to limit the in band noise and achieve sufficient SNR.

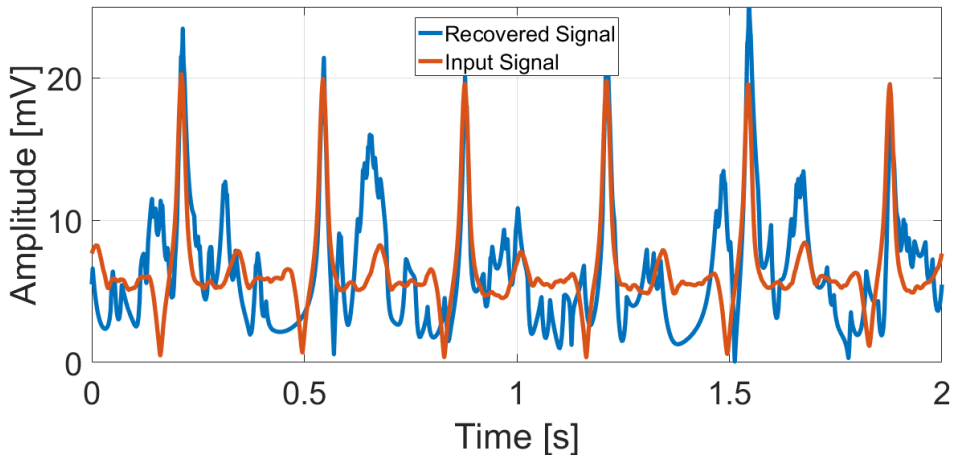


**Figure 4.17:** Response of the measurement interface to an ECG signal provided by a signal generator.

### ***In-vivo* measurement**

Figure 4.18 shows an *in-vivo* experiment measuring the heartbeat of a person, obtained by connecting our system to the test subject using standard wet electrodes (Kendall's H124SG) placed on the chest. The threshold crossing of the recovered

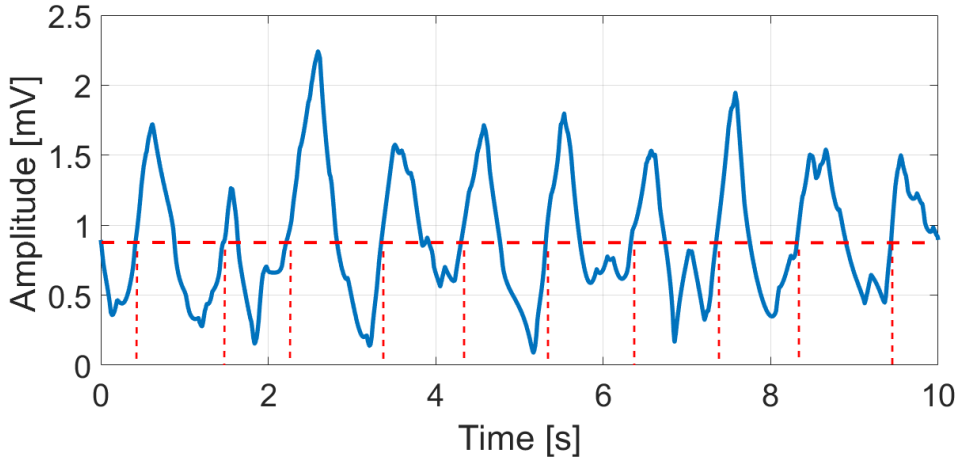


**Figure 4.18:** Reconstructed signal from PWM waveform showing heartbeat from in-vivo measurement.

signal shown in Figure 4.18 indicates the heartbeat rhythm. As discussed, a 10 Hz LPF is used to filter the reset frequency and its harmonics and to limit the in band noise. The detected heartbeat is 60 bpm which is well in the range of a normal heartbeat for a person at rest. In this case the shape of the output waveform is less recognizable, due to the strong low-pass filtering applied, but the peaks of the heart activity are clearly recognizable. An overview of the main circuit performance of our HR measurement interface and a comparison to prior-art is given in Table 4.3.

**Table 4.3:** Comparison to the state-of-the-art

	JSSC'17[4]	ISSCC'17[6]	HR Measurement Interface
Technology	a-Si	a-IGZO	a-IGZO
Architecture	Chopped Amplifier	ADSM	Chopped Amplifier + Reset Integrator
Input domain	Voltage	Current	Voltage
Output type	Analogue	PWM	PWM
Application	EEG	Temp. sensor	HR
Chopping frequency	5 kHz	-	500 Hz
Integrated noise [ $\mu V_{rms}$ ] (BW)	2.3 (100 Hz)	-	186.3 (200 Hz)
Current consumption [ $\mu A$ ]	200	100	5.2
Supply voltage [V]	55	20	10
Power dissipation [mW]	11	2	0.052
Area [mm <sup>2</sup> ]	-	27.9	52.5

## 4.4 Time based ECG interface

### 4.4.1 Improved system architecture

The integrated input noise in the system presented in Section 4.3.3 is  $186.3 \mu V_{rms}$  which is too high for ECG standards, thus, enabling only HR measurements. In this Section we present an improved version of the system with better noise performance, designed and simulated using DUGA TFT models. The improved system architecture is shown in Figure 4.19. The improved performance compared to the system shown in Figure 4.9 is due to better TFT technology, circuit improvements and correlated double sampling (CDS) at system level. The front-end consists of an input chopper, a 2-stage preamplifier consisting of cascaded diode-connected load differential amplifiers (Figure 4.20(a)), a reset integrator (Figure 4.20(b)) and additionally two pseudo CMOS inverters with controllable hysteresis to implement the comparators (Figure 4.20(c)).

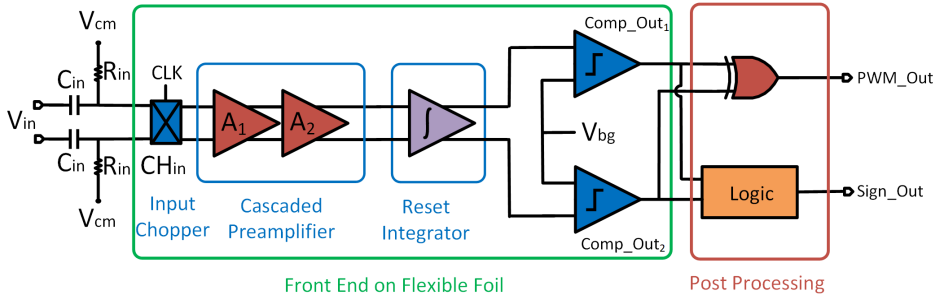


**Figure 4.19:** System architecture of the improved version of the system shown in Figure 4.9.

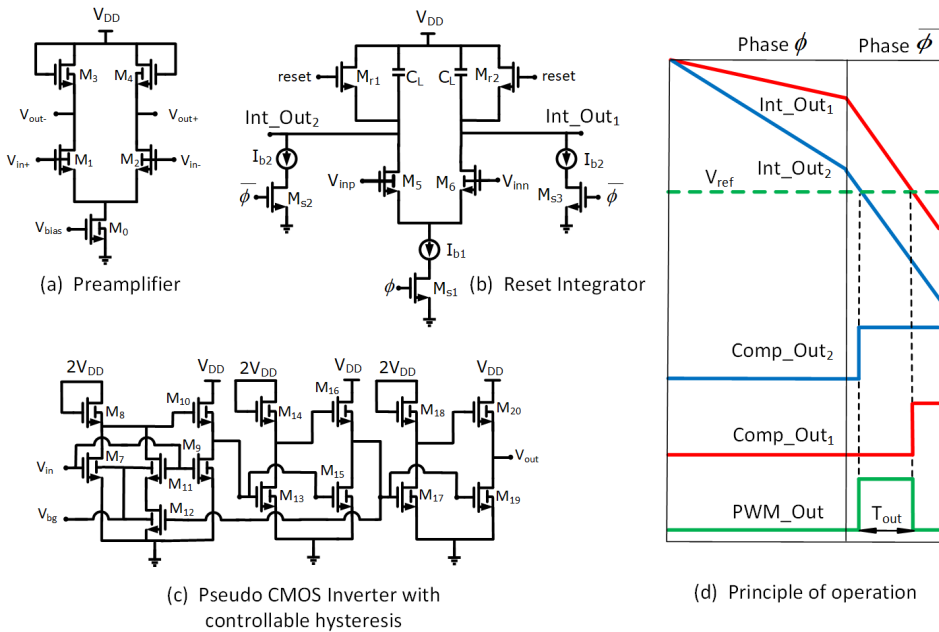


**Figure 4.20:** Schematics of (a) the preamplifier, (b) the reset integrator, (c) pseudo CMOS inverter and (d) working principle of the reset integrator.

#### 4.4.2 Principle of operation

The preamplifier consists of a diode-connected load differential amplifier (Figure 4.20(a)). The back gates of the current-source TFT  $M_0$  and the load TFTs  $M_{3,4}$  are connected to the source to increase the output resistance (Figure 4.20(a)). Moreover, the back gates of the input TFTs  $M_{1,2}$  are connected to the front gates to increase transconductance. The reset integrator (Figure 4.20(b)) consists of a differential input pair  $M_{5,6}$  and load capacitors  $C_L$ . The outputs of the integra-

tor are connected to comparators which consist of three pseudo CMOS inverters connected in cascade. The output of the second inverter (Figure 4.20(c)) in the cascade is also connected to the gate of  $M_{12}$  to provide positive feedback. This introduces hysteresis in the inverter, while the switching threshold of the inverter can be controlled through the back gate biasing  $V_{bg}$  of  $M_{7,11,12}$  as shown in the next Section. The hysteresis is beneficial to suppress kickback noise from the integrator outputs.

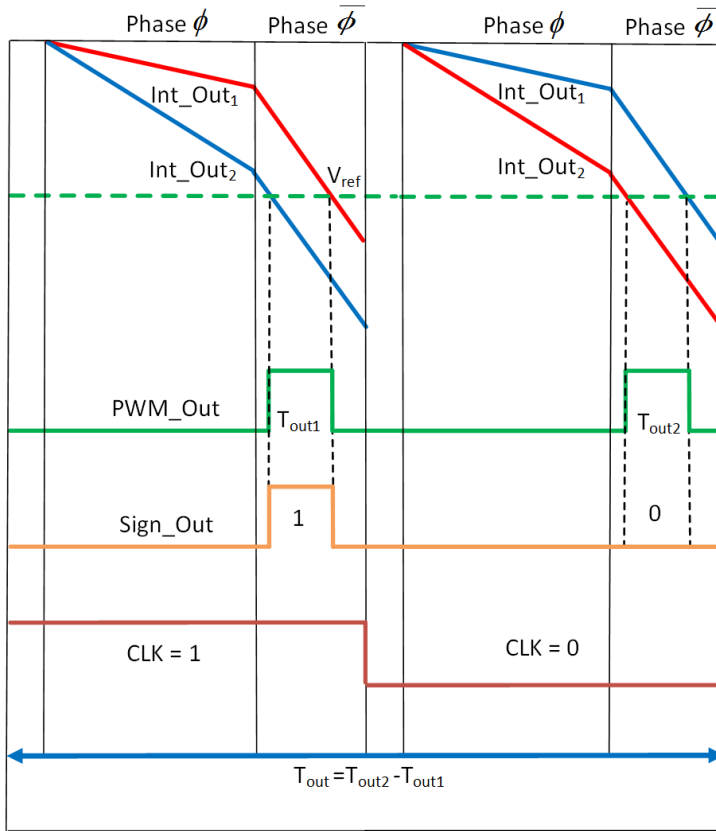


**Figure 4.21:** Principle of system level CDS.

The low-frequency noise is suppressed using CDS at system level. An input chopper ( $CH_{in}$ ) is used to alternate the connection between the inputs of the preamplifier periodically with a low frequency. The output signal is extracted by subtract-

ing in the digital domain two consecutive samples, while taking into account the sign bit, as shown in Figure 4.21. When CLK is high, the inputs of the preamplifier are connected in the usual way and a PWM output of pulse width  $T_{out1}$  is obtained. In the next phase, CLK goes low, the inputs of the preamplifier are reversed, and the PWM output of pulse width  $T_{out2}$  is obtained. By subtracting  $T_{out2}$  from  $T_{out1}$  (while keeping the sign bit in consideration), a final pulse  $T_{out}$  is obtained. This approach cancels the quantities that have high correlation between two consecutive samples, i.e. offset and flicker noise, while the signal is doubled.

### 4.4.3 Simulation results

#### Circuit characterization

The system is simulated using the a-IGZO DUGA TFT model, introduced in Chapter 2. Figure 4.22 shows the simulated frequency response of the cascaded preamplifier. It achieves a gain of 35.8 dB in 1.1 kHz bandwidth with 2  $\mu A$  current consumption from 10 V supply. Figure 4.23 shows the input referred noise spectrum of the system with and without system level CDS. The interface presented in this work achieves in simulation 52.5  $\mu V_{rms}$  integrated input referred noise in the 1-100 Hz band without application of CDS at system level. With 250 Hz system level CDS, an input referred noise of 18.3  $\mu V_{rms}$  is simulated in the 1-100 Hz band.

The current consumption in the integrator during the first phase is 250 nA while in the second phase, it is 500 nA in each branch. Fig. 6 shows the simulated DC transfer curve of the pseudo CMOS inverter. It can be seen from Figure 4.24 that the trip point of the inverter can be controlled through the back gate voltage  $V_{bg}$  applied to  $M_{7,11,12}$ .

#### Signal reconstruction

The reset frequency and its harmonics can be removed from the PWM output by low-pass filtering in a 100 Hz band, which passes only the input signal and thus

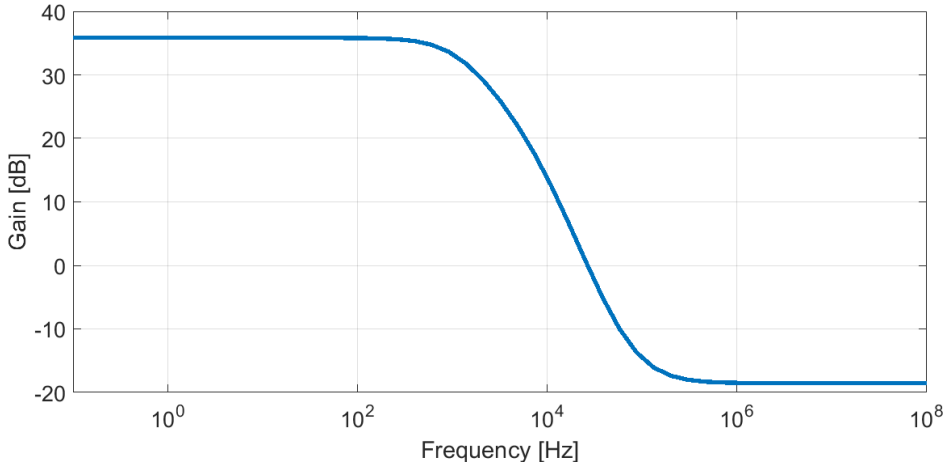


**Figure 4.22:** Simulated frequency response of the preamplifier.

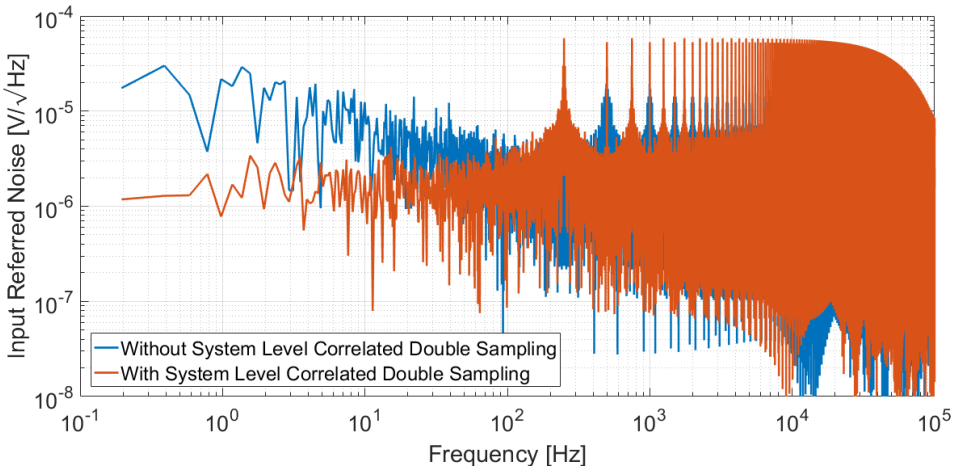


**Figure 4.23:** Simulated noise spectrum of the proposed system.

allows its reconstruction in the analogue domain. The reset frequency is 500 Hz while the CLK signal is half of the frequency of the reset signal. Figure 4.25 shows the reconstruction of a  $1\text{ mV}_{pp}$  ECG signal obtained in simulation using this method. The simulation includes a noise model including  $1/f$  noise as described in Chapter 2, and the ECG signal is still well recognizable.

An overview of the main circuit performance of our ECG interface and some relevant publications is given in Table 4.4. The better performance compared to the HR measurement interface described in the beginning of this Chapter [1], is

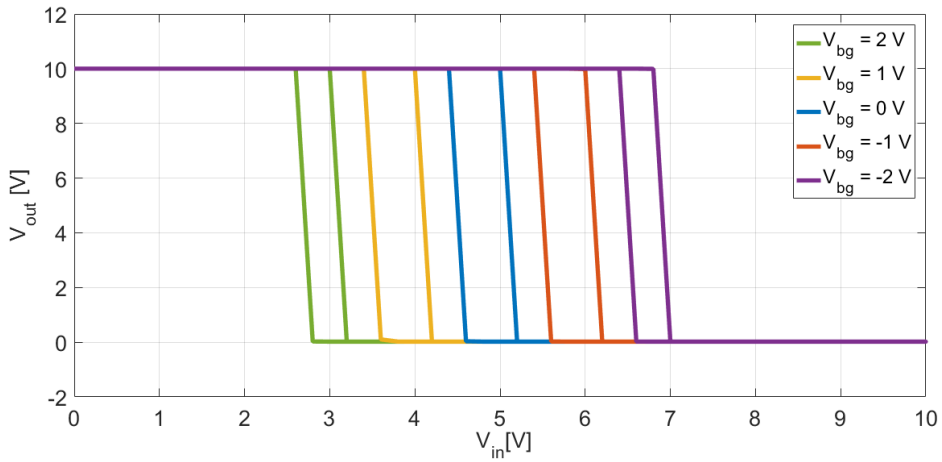


**Figure 4.24:** Simulated DC transfer curve of the inverter with cascading three pseudo-CMOS inverters.

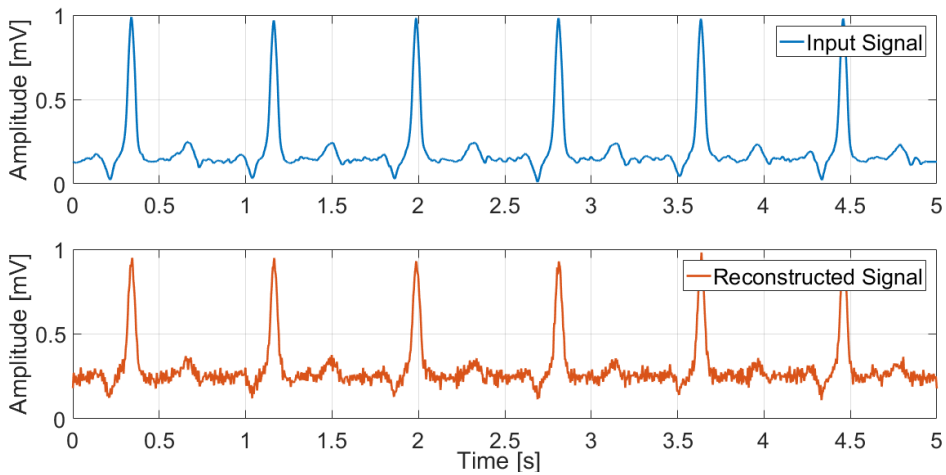


**Figure 4.25:** Simulated response of the full system to an ECG source signal.

due to both, better TFT technology and circuit improvements. From the technology perspective, the self-aligned a-IGZO technology used in this work has a Hooge factor which is significantly better than the a-IGZO technology used in [1] and thus contributes less  $1/f$  noise. From the circuit perspective, in this work a system level CDS has been used, which reduces the total input referred noise of the whole system. The conventional chopping used in [1], on the contrary, was only applied to the preamplifier and the input of the integrator. Besides, the higher amplifier gain

and larger input transconductance, both obtained thanks to the double gate TFT architecture, benefit the noise efficiency of the interface. The simulated noise with system level chopping results in a NEF of 115.12. The total power consumption is  $26.25 \mu W$  with 10 V supply voltage. This makes the simulated PEF of the presented interface  $6.64\times$  better than [4].

Table 4.4: Comparison to prior literature

	JSSC'17[4]	SSCL'18[18]	ESSCIRC'18[1]	ISSCC'17[6]	Time based ECG Interface <sup>a</sup>	
Technology	a-Si	a-IGZO	a-IGZO	a-IGZO	Dual Gate Self Aligned a-IGZO	
Architecture	Chopped Amplifier	Chopped Amplifier with Frequency Division Multiplexing	Chopped Amplifier + Reset Integrator	ADSM	Preamplifier + Reset Integrator + Pseudo CMOS Inverter	
Input domain	Voltage	Voltage	Voltage	Current	Voltage	
Output type	Analogue	Analogue	PWM	PWM	PWM	
Application	EEG	EMG	HR	Temp. Sensor	ECG	
Chopping frequency	5 kHz	5 kHz	500 Hz	-	-	250 Hz
Integrated noise (BW)	$2.3 \mu V_{rms}$ (100 Hz)	$125 \mu V_{rms}$ (500 Hz)	$186.3 \mu V_{rms}$ (200 Hz)	-	$52.5 \mu V_{rms}$ (100 Hz)	$18.3 \mu V_{rms}$ (100 Hz)
Current consumption [ $\mu A$ ]	200	50	5.2	100	2.6	
Supply voltage [V]	55	26	10	20	10	
Power dissipation [mW]	11	1.3	0.052	2	0.026	
NEF	126.29	1534.80	1166.4	-	330.26	115.12
PEF	$8.77 \times 10^5$	$6.12 \times 10^7$	$1.36 \times 10^7$	-	$1.09 \times 10^6$	$1.32 \times 10^5$
Area [ $mm^2$ ]	-	11.2	52.5	27.9	19.5	

<sup>a</sup>Simulated results.

## 4.5 Conclusions

This Chapter presents two time based interfaces for bio-signal acquisition systems for wearable applications developed with a-IGZO TFT technologies. The proposed time based interfaces perform a voltage to pulse width conversion. The proposed system architectures exploit conventional chopping and system level CDS to improve the noise performance, respectively.

The initial part of the Chapter presents an application scenario that requires a moderate SNR. A heart-rate measurement interface for wearable applications, fabricated on a flexible foil, is presented. The output is provided as a PWM representation. Voltage to pulse-width conversion is achieved with a simple and power minimalistic approach, using a reset integrator. The presented solution is compact, low cost and adds to user comfort, thanks to its mechanical flexibility. However, this approach achieves an SNR that is insufficient for most biomedical monitoring applications.

The approach presented in the first part of this Chapter is further improved for applications that require higher SNR. In the later part of this Chapter, the SNR is improved by applying CDS at system level to enable ECG monitoring using a low power flexible ECG interface. The improved performance compared to the system shown in Figure 4.9 is due to better TFT technology, circuit improvements and the CDS at system level. It can be concluded that for high SNR applications like ECG monitoring, DUGA a-IGZO TFT technology appears to be a promising solution.

## Bibliography

- [1] M. Zulqarnain, S. Stanzione, J.-L. P. V. D. Steen, G. H. Gelinck, K. Myny, S. Abdinia, and E. Cantatore, "A 52  $\mu$ W heart-rate measurement interface fabricated on a flexible foil with a-IGZO TFTs," in *ESSCIRC 2018 - 44th European Solid State Circuits Conference (ESSCIRC)*, pp. 222–225, IEEE, Sept. 2018.
- [2] M. Zulqarnain, S. Stanzione, J.-L. P. J. van der Steen, G. H. Gelinck, K. Myny, and E. Cantatore, "A low power time domain ECG interface based on flexible a-IGZO TFTs," in *2019 IEEE 8th International Workshop on Advances in Sensors and Interfaces (IWASI)*, pp. 205–209, IEEE, June 2019.
- [3] K. Myny, "The development of flexible integrated circuits based on thin-film transistors," *Nature Electronics*, vol. 1, pp. 30–39, Jan. 2018.
- [4] T. Moy, L. Huang, W. Rieutort-Louis, C. Wu, P. Cuff, S. Wagner, J. C. Sturm, and N. Verma, "An EEG acquisition and biomarker-extraction system using low-noise amplifier and compressive-sensing circuits based on flexible, thin-film electronics," *IEEE Journal of Solid-State Circuits*, vol. 52, pp. 309–321, Jan. 2017.
- [5] H. Fuketa, K. Yoshioka, Y. Shinozuka, K. Ishida, T. Yokota, N. Matsuhisa, Y. Inoue, M. Sekino, T. Sekitani, M. Takamiya, T. Someya, and T. Sakurai, "1  $\mu$ m-thickness ultra-flexible and high electrode-density surface electromyogram measurement sheet with 2 V organic transistors for prosthetic hand control," *IEEE Transactions on Biomedical Circuits and Systems*, vol. 8, pp. 824–833, Dec. 2014.
- [6] C. Garripoli, J.-L. P. J. van der Steen, E. Smits, G. H. Gelinck, A. H. M. V. Roermund, and E. Cantatore, "An a-IGZO asynchronous delta-sigma modulator on foil achieving up to 43 dB SNR and 40 dB SNDR in 300 Hz bandwidth," in *2017 IEEE International Solid-State Circuits Conference (ISSCC)*, pp. 260–261, IEEE, Feb. 2017.
- [7] S. Karvonen, T. Riley, S. Kurtti, and J. Kostamovaara, "A quadrature charge-domain sampler with embedded FIR and IIR filtering functions," *IEEE Journal of Solid-State Circuits*, vol. 41, pp. 507–515, Feb. 2006.
- [8] P. Calzolari, and S. Graffi, "Switched-Capacitor Concept for Analog Signal NMOS Am-

- plifiers,” in *ESSCIRC 1979 - 5th European Solid State Circuits Conference (ESSCIRC)*, pp. 134–135, Sept. 1979.
- [9] J. Lin, M. Miyahara, and A. Matsuzawa, “A 15.5 dB, wide signal swing, dynamic amplifier using a common-mode voltage detection technique,” in *2011 IEEE International Symposium of Circuits and Systems (ISCAS)*, pp. 21–24, IEEE, May 2011.
- [10] F. van der Goes, C. Ward, S. Astgimath, H. Yan, J. Riley, J. Mulder, S. Wang, and K. Bult, “A 1.5 mW 68 dB SNDR 80 MS/s 2x interleaved SAR-assisted pipelined ADC in 28 nm CMOS,” in *2014 IEEE International Solid-State Circuits Conference Digest of Technical Papers (ISSCC)*, pp. 200–201, IEEE, Feb. 2014.
- [11] B. Malki, B. Verbruggen, P. Wambacq, K. Deguchi, M. Iriguchi, and J. Craninckx, “A complementary dynamic residue amplifier for a 67 dB SNDR 1.36 mW 170 MS/s pipelined SAR ADC,” in *ESSCIRC 2014 - 40th European Solid State Circuits Conference (ESSCIRC)*, pp. 215–218, IEEE, Sept. 2014.
- [12] J. Lin, D. Paik, S. Lee, M. Miyahara, and A. Matsuzawa, “An ultra-low-voltage 160 MS/s 7 bit interpolated pipeline ADC using dynamic amplifiers,” *IEEE Journal of Solid-State Circuits*, vol. 50, pp. 1399–1411, June 2015.
- [13] C.-C. Liu and M.-C. Huang, “A 0.46 mW 5 MHz BW 79.7 dB SNDR noise-shaping SAR ADC with dynamic-amplifier-based FIR-IIR filter,” in *2017 IEEE International Solid-State Circuits Conference (ISSCC)*, pp. 466–467, IEEE, Feb. 2017.
- [14] M. Zhang, K. Noh, X. Fan, and E. Sanchez-Sinencio, “A 0.8–1.2 V 10–50 MS/s 13-bit subranging pipelined-SAR ADC using a temperature-insensitive time-based amplifier,” *IEEE Journal of Solid-State Circuits*, vol. 52, pp. 2991–3005, Nov. 2017.
- [15] M. S. Akter, K. A. A. Makinwa, and K. Bult, “A capacitively degenerated 100-dB linear 20–150 MS/s dynamic amplifier,” *IEEE Journal of Solid-State Circuits*, vol. 53, pp. 1115–1126, Apr. 2018.
- [16] AAMI, “Diagnostic electrocardiographic devices,” *ANSI/AAMI EC11. Association for the Advancement of Medical Instrumentation*, Arlington, VA, 2001.
- [17] U. J. Yoon, Y. S. Noh, Y. M. Han, M. Y. Kim, J. H. Jung, I. S. Hwang, H. R. Yoon, and I. C. Jeong, “Electrocardiogram signal processing method for exact heart rate

- detection in physical activity monitoring system: Wavelet approach,” in *2010 IEEE EMBS Conference on Biomedical Engineering and Sciences (IECBES)*, pp. 232–235, IEEE, Nov. 2010.
- [18] C. Garripoli, S. Abdinia, J.-L. J. P. van der Steen, G. H. Gelinck, and E. Cantatore, “A fully integrated 11.2 mm<sup>2</sup> a-IGZO EMG front-end circuit on flexible substrate achieving up to 41 dB SNR and 29 M $\Omega$  input impedance,” *IEEE Solid-State Circuits Letters*, vol. 1, pp. 142–145, June 2018.



# Chapter 5

## A Flexible ECG Patch Compatible with NFC RF Communication

*This Chapter presents a flexible ECG patch implemented on foil with self-aligned  $\alpha$ -IGZO TFTs, which is capable to acquire ECG signals, amplify them and convert them to a sequence of bits. The presented approach provides a digitization strategy using a time reference rather than a voltage reference, and is particularly attractive for implementation with  $\alpha$ -IGZO TFTs on foil. The analogue frontend has a measured input-referred noise of  $8 \mu V_{rms}$  in the 1-100 Hz band. The system achieves experimentally 67.4 dB CMRR, 58.9 dB PSRR and  $16.5 M\Omega$  input impedance at 50 Hz, while using 1 kHz chopping. The signal from the electrodes is transformed to a 105.9 kb/s Manchester encoded serial bit stream which could be sent wirelessly to a smart phone according to the Near Field Communication (NFC) standard for further post processing.*

*The contents of this Chapter have been published in Nature's npj Flexible Electronics [1].*

## 5.1 Introduction

As discussed in Chapter 1, wearable biomedical devices have witnessed a growing interest in recent years. Indeed, these devices allow long-term non-invasive monitoring of people in the comfort of their daily routine [2, 3, 4], providing information that is valuable to enable early diagnosis and effective treatment of patients, or that can be used to support a healthy lifestyle. Biomedical wearables typically aim at measuring vital signs or the bioelectric activity of different organs, such as the brain, the muscles and the heart. These signals will be named in the context of this Chapter as “bio-signals”.

Cardiovascular diseases are worldwide the first cause of death, causing 31% of all fatalities every year [5]. A valuable tool to diagnose these diseases is the electrocardiogram (ECG), a non-invasive surface measurement of the heart’s electrical potentials. Traditionally, to perform ECG measurements, patients are generally connected with wires to a bulky bio-potential acquisition system. This makes long-term monitoring impossible. More recently, portable and wearable ECG monitoring systems became available. These solutions are particularly valuable to diagnose various cardiovascular diseases in an early stage. For this reason, the focus of this work is on a wearable patch to measure ECG.

Continuous monitoring of physiological signals requires wearable devices to be conformable to the shape of the body, in order to improve the quality of physiological signal monitoring and to ensure maximum comfort of use. Advancements in fabrication techniques and new materials made it possible to build flexible and conformal electronics. Thus, these advancements are an important enabler to build wearables for biomedical applications [6, 7, 8].

In an effort to advance the state-of-the-art of wearable bio-signal monitoring devices exclusively based on flexible electronics, we report here for the first time

(to the best of the authors' knowledge) a flexible ECG sensor which exploits TFT-based circuits [9, 10, 11, 12, 13, 14, 15, 16] on flexible foil for the full chain of signal acquisition, amplification and digitization, and which is capable to measure ECG signals captured by a pair of electrodes with sufficient signal to noise ratio [17] (Figure 5.1). Additionally, the digital output is provided as a serial 105.9 kb/s Manchester encoded bit stream compatible with the NFC wireless transmission standard, so that the measured data could be sent to a smart phone for further elaboration and presentation. The absence of any rigid active component makes the system conformable to the human body and comfortable to use. Moreover, the implementation of the full system with flexible TFTs reduces the extra processing steps and the cost required for the integration of rigid and flexible electronic components, enabling a solution that could become compatible with single use.

The rest of the Chapter is organized as follows: Section 5.2 discusses the system architecture. In Section 5.3, circuit design of the implemented system is presented. The experimental measurement results including *in-vivo* characterization are shown in Section 5.4. Finally, Section 5.5 concludes the Chapter.

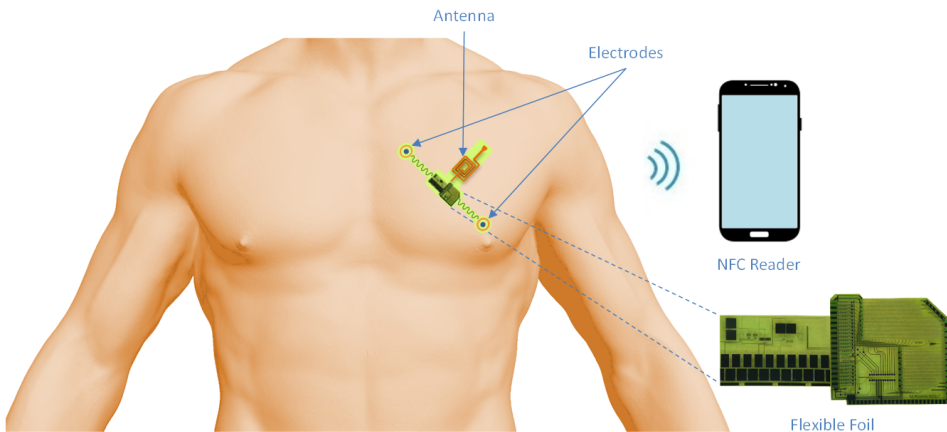


**Figure 5.1:** Representative application scenario of the presented ECG patch.

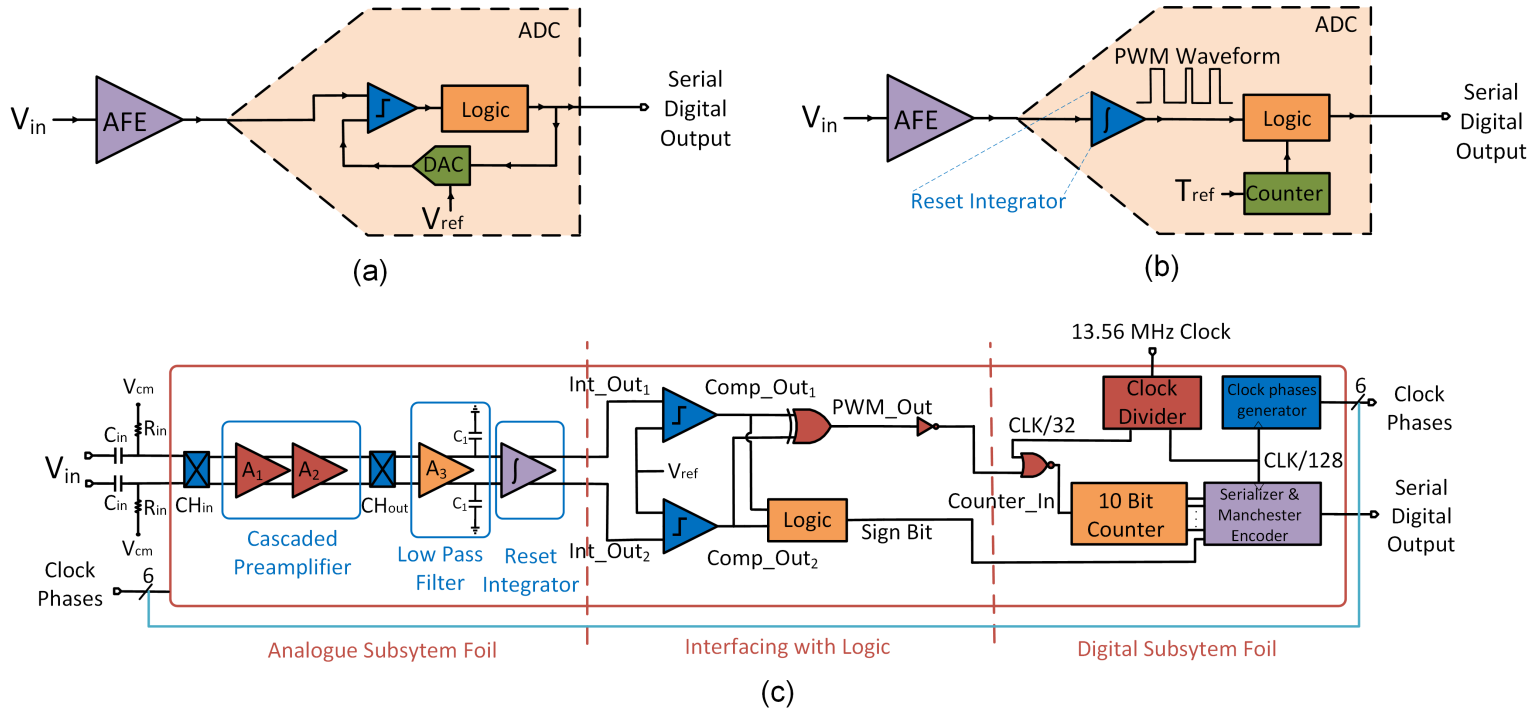


**Figure 5.2:** System architecture. (a) Conventional bio-potential acquisition system, (b) System-level diagram of the presented ECG acquisition system, (c) Detailed architecture of the presented system.

## 5.2 System architecture

A bio-potential acquisition system typically consists of two main blocks (Figure 5.2(a)): an analogue frontend (AFE) amplifies the signal while ensuring a suitable noise level, to preserve the shape of the signal, and provides sufficiently high impedance to enable reading the ECG signal with appropriate electrodes placed on the skin. An analogue to digital converter (ADC) follows, to convert the bio-potential signal to a digital representation, enabling robust wireless transmission and/or further signal processing. As shown in Figure 5.2(a), several ADC architectures consist typically of a comparator, a digital to analogue converter (DAC) and suitable logic. To minimize the influence of temperature and technology variability, both the AFE and the ADC are typically designed so that their signal transfer function is determined by the ratio of similar components (e.g. resistors). If variations affect all components proportionally to their value (e.g. the resistance per square increases by a given amount), these ratios tend to stay unchanged. Moreover, in typical Silicon designs, the DAC uses a reference voltage generator (Figure 5.2(a)). This reference voltage is very stable against process, supply and temperature (PVT) variations. The DAC uses this reference to produce output voltages that are also stable against PVT. At the state-of-the-art, it is difficult to make a voltage reference in a-IGZO, because the main components used for this purpose (diodes and bipolar junction transistors) are not available in a-IGZO processes.

For this reason, the design presented in this Chapter takes a radically different approach, and digitizes the input data in the time domain. The concept is shown in Figure 5.2(b). After the AFE, a reset integrator (as presented in Chapter 4) is used to transform the signal amplitude in duty cycle information (Pulse-Width Modulated, i.e. PWM representation). This means that the duty cycle of the signal produced by the reset integrator is proportional to the input signal. Digitization is then simply achieved by counting, for how many clock cycles the integrator output is high every period. In this case a time reference is needed for digitization, as

**Table 5.1:** Specifications of ECG recording systems as dictated by the ANSI AAMI standard

Electrical Parameter	ANSI AAMI EC11 Standard
Input Dynamic Range	$\pm 5$ mV
Input Referred Noise	$< 20 \mu V_{rms}$ (100 Hz)
Input Impedance	$> 2.5 M\Omega$
CMRR	$> 60$ dB

shown in Figure 5.2(b). A time reference can be easily generated in our system, which is meant to communicate to a smart phone via NFC, by using the 13.56 MHz NFC carrier as time reference, after suitable division in the digital domain [18]. The approach described here, provides a digitization strategy, without the need for a voltage reference, and thus, is particularly suited to implementation with a-IGZO TFTs on foil.

### 5.3 Circuit design

The electrical performance specifications of systems dedicated to ECG recording applications are regulated by the ANSI-AAMI standard [19]. Table 5.1 presents the target specifications according to this ECG standard. The input referred noise should be less than  $20 \mu V_{rms}$  in a bandwidth of 100 Hz. The input impedance should be greater than  $2.5 M\Omega$ . The common mode rejection should be at least 60 dB.

A more detailed schematic of the proposed flexible patch is provided in Figure 5.2(c). The system consists of two plastic foils (Figure 5.1) on which a-IGZO TFTs are fabricated. The first foil (analogue subsystem) is connected to the electrodes. The AFE captures the ECG signals, and the reset integrator transforms them to a PWM representation. The second foil (digital subsystem), connected to the first foil (analogue subsystem), digitizes the PWM signal and serializes the output bits, so that they can be sent to a receiver using radiofrequency (RF) NFC communication. The system is divided in two foils for yield optimization. Technically, at the

state-of-the-art, it is possible to have the full system on a single foil. Essentially, the middle part shown in Figure 5.2(c) (interfacing with logic) is designed on the foil, but in practice for the measurements shown in Section 5.4, it is implemented with discrete components due to some functionality issues.

The analogue frontend (AFE) consists of an input chopper (Figure 5.2(c),  $CH_{in}$ ), a 2-stage cascaded diode connected load preamplifier (Figure 5.2(c)), a de-chopper (Figure 5.2(c),  $CH_{out}$ ), and a low pass filter (Figure 5.2(c), LPF). The input signal is AC-coupled before the input chopper, to cancel the large DC electrode offsets. Due to the low frequency bio-signals, chopping is used to suppress the amplifier flicker noise and offset. The chopping frequency is chosen as a trade-off between noise, preamplifier bandwidth (which has an impact on power consumption) and input impedance. The preamplifiers are designed to have a bandwidth larger than the target chopping frequency, which is 1 kHz. They are built using diode-connected load TFTs, so that their gain is mainly dependent on the ratio of the transconductance of input and load devices, improving the robustness to process variations. The detailed schematic of each preamplifier is shown in Figure 5.3(a). The input TFTs  $M_{1,2}$  in  $A_1$  have a large area ( $15000 \mu m^2$ ) to bring the  $1/f$  noise corner close to the chopping frequency. For the diode-connected load transistors  $M_3$  and  $M_4$  (Figure 5.2(a)), the back gates are connected to the output nodes to increase the output resistance, while the input transistors  $M_1$  and  $M_2$  have back gates connected to their front gates to increase transconductance and improve noise efficiency. The second amplifier,  $A_2$ , has the same topology as  $A_1$ , with different aspect ratios of the input pair. To avoid excessive noise aliasing, the output after the chopper is low-pass filtered by another differential amplifier with diode connected load, with a 100 pF load capacitor, which has a nominal 100 Hz bandwidth.

The AFE is followed by the reset integrator (Figure 5.3(b)). The latter consists of a differential input pair  $M_{5,6}$  with load capacitors  $C_L$ . The principle of operation

is similar as explained in Chapter 4: a two-phase integration is used, where in the first phase  $\phi$ , the capacitor discharge is signal-dependent, and in the second phase  $\bar{\phi}$ , the capacitors are discharged by a constant current (Figure 5.3(c)). The instants at which the integrator outputs are discharged below a given threshold  $V_{ref}$  is detected by two external comparators. Thanks to the constant slope observed in phase  $\bar{\phi}$ , the time walk difference between the two comparators is minimized and the linearity of the voltage to duty-cycle transformation is improved. The time delay in threshold crossing between the two branches of the integrator output,  $T_{out}$ , is proportional to the input signal (Figure 5.3(c)). The comparator outputs are then fed to a XOR gate to obtain a PWM representation of the input signal with an additional sign bit. The entire analogue subsystem is extremely minimalistic in terms of transistor count, which benefits to the circuit yield and to the power consumption.

In the digital subsystem (Figure 5.2(c)), a clock divider is used to generate timing signals from a 13.56 MHz source (CLK). The PWM output is clock gated (and thus quantized in time) with a clock of frequency CLK/32 and then fed to an asynchronous counter which creates a digital multi-bit representation of the PWM output.

A 10 bit counter is required by the design constraints as shown below: The relation between output jitter and counter frequency can be given as:

$$\Delta t_{rms}^2 = \frac{1}{12f_c^2} \quad (5.1)$$

where,  $\Delta t_{rms}$  is the quantization effect (in the time domain) of the counter. The above Equation 5.1 can be translated to input referred noise as:

$$v_{in,rms}^2 > \frac{1}{12f_c^2 G^2} \quad (5.2)$$

where,  $v_{in,rms}$  is the rms input referred quantization noise and G is the gain of the full chain. The targeted input referred noise is less than  $20 \mu V_{rms}$  and the gain is

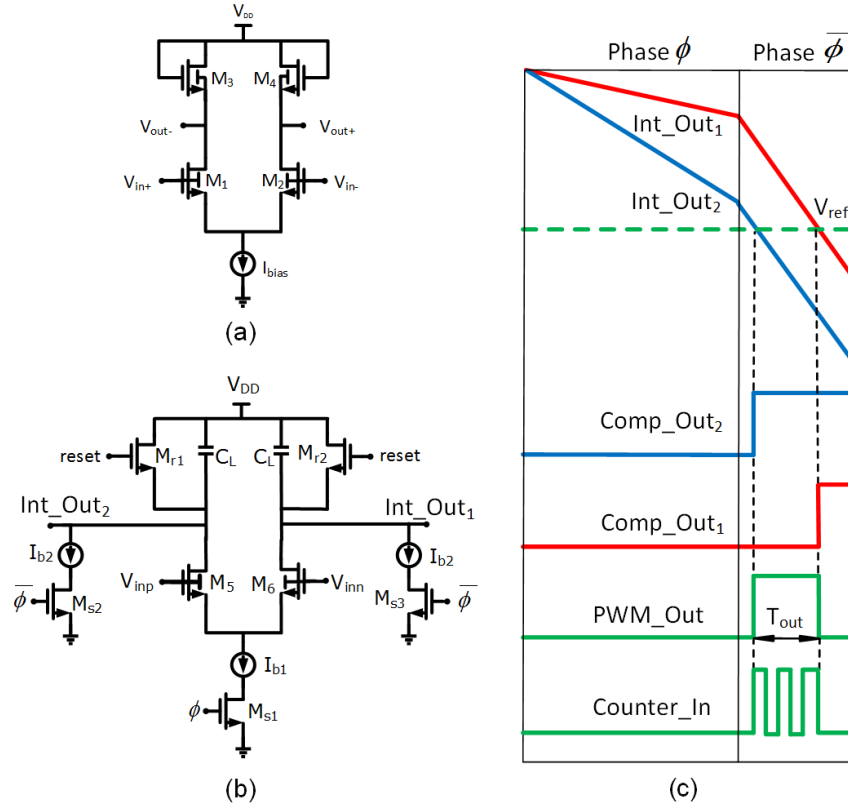


**Figure 5.3:** Circuit schematics and working principle. (a) Schematic of each of the two cascaded diode-load amplifiers in the preamplifier; (b) Reset integrator; (c) Reset integrator working principle.

35 ms/V. Substituting these values in Equation 5.2 results in  $f_c > 412.4 \text{ kHz}$ . The chosen  $f_c$  is:

$$f_c = \frac{13.56 \text{ MHz}}{32} = 423.75 \text{ kHz} \quad (5.3)$$

$$t_c = \frac{1}{f_c} = 2.36 \mu s = t_{\min} \quad (5.4)$$

The maximum period which has to be counted by the counter is  $\bar{\phi}$  (the constant current discharge phase) i.e.:

$$\bar{\phi} = 1.8 \text{ ms} = t_{\max} \quad (5.5)$$

The number of bits ( $n$ ) of the counter can be obtained as:

$$2^n = \frac{t_{\max}}{t_{\min}} \quad (5.6)$$

Equation 5.6 results in  $n > 9$  and hence a 10 bit counter has been selected for our first prototype. The counter outputs are then serialized and Manchester encoded, generating a 32 bit serial stream including a 12 bit preamble, 10 counter bits and other fixed payload. The serializer and Manchester encoder are driven with a clock of frequency  $\text{CLK}/128$ , to provide the 105.9 kb/s output bit stream which is compatible with NFC RF transmission. The clock phases needed to drive the analogue subsystem are also generated on foil (Clock Phase Generator). The timing diagram of the clock phases is shown in Figure 5.4. It can be seen from Figure 5.4, that the reset period is 4 ms (indicated by  $T_4$ ), phase  $\phi$  (the integration phase) is 1.8 ms (indicated by  $T_2 - T_1$ ), phase  $\bar{\phi}$  (the constant current discharge phase) is 1.8 ms (indicated by  $T_3$ ) and the chopping period is 1 ms. The digital subsystem is designed by the imec Leuven team led by Kris Myny.

## 5.4 Measurement results

### 5.4.1 Electrical characterization

To characterize the preamplifier (Figure 5.5), this circuit has been connected via a suitable mechanical connector (Yokowo DS CCNL-050-47-FRC) to off-the-shelf voltage buffers (TI OPA445AP), followed by an instrumentation amplifier (TI INA-111AP) for differential to single ended conversion. The output of the instrumentation amplifier is connected to the HP35670A Dynamic Signal Analyser to measure the frequency response and the output noise. A  $10 \text{ mV}_{p-p}$  sine wave with 5 V DC bias, and a 5 V DC reference were applied to the positive input ( $V_{in+}$ ) and negative input ( $V_{in-}$ ) of the preamplifier (Figure 5.3(a)), respectively. The supply voltage is 10 V. Figure 5.5 shows the measured transfer curve of the cascaded preamplifier. It

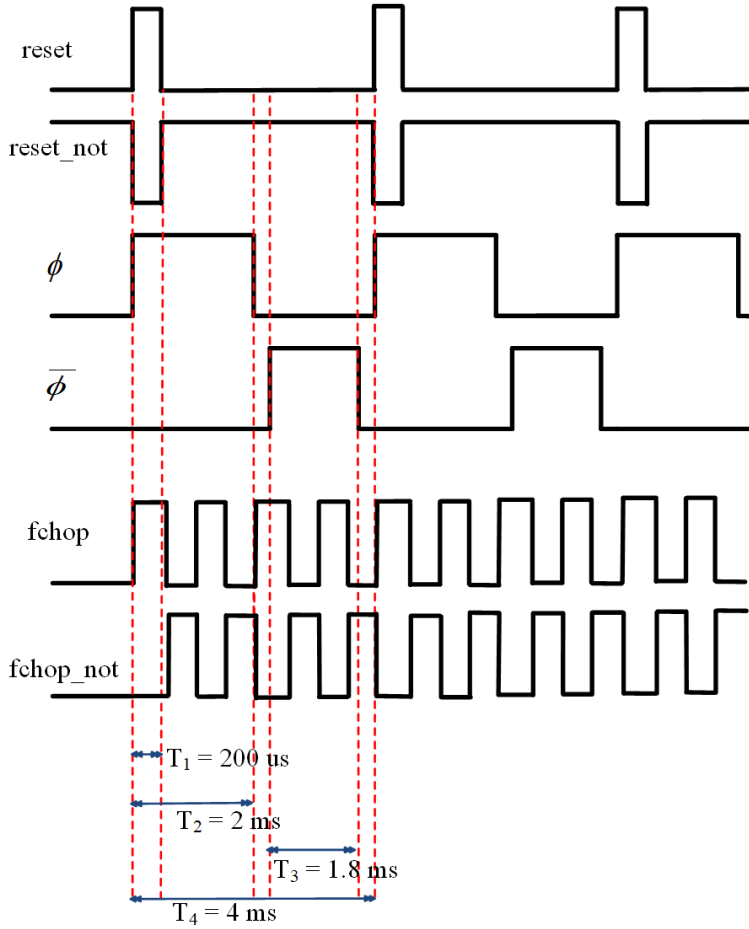


**Figure 5.4:** Timing diagram of the clock phases.

achieves a gain of 23.5 dB in a 3.7 kHz bandwidth with  $12.5 \mu\text{A}$  current consumption from 10 V supply. The integrated input-referred noise in the 1-100 Hz BW is  $8 \mu\text{V}_{\text{rms}}$  with a chopping frequency of 1 kHz. For the full analogue chain characterization (Figure 5.6), a  $10 \text{ mV}_{\text{p-p}}$  sine wave with varying frequency was applied to the input of the system and the output PWM was observed. The output data are acquired using a Digilent® Analog Discovery 2 board. The ratio between the fundamental harmonic of the of the filtered output PWM and the applied input signal has been calculated for each point of the frequency response recorded from the full analogue chain (from input to output PWM). Figure 5.6 shows the measured

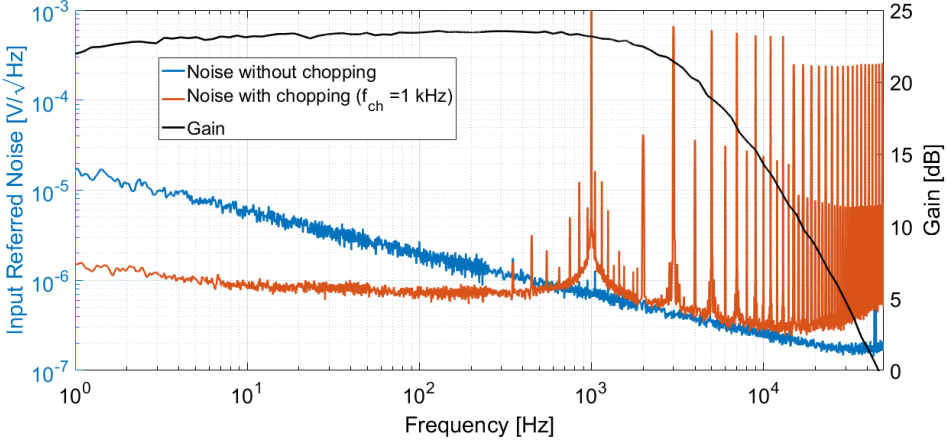


**Figure 5.5:** Measured frequency response and input-referred noise of the cascaded preamplifier.

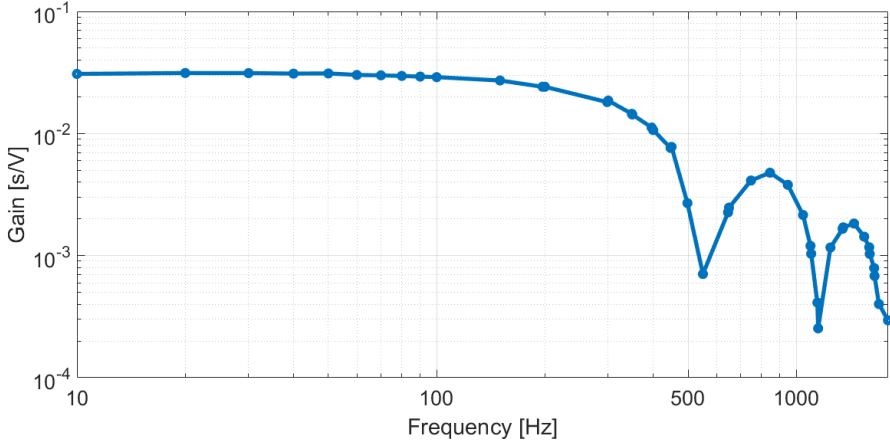


**Figure 5.6:** Measured transfer function of the full analogue chain (from input to output PWM).

transfer curve of the full analogue chain, including the reset integrator and PWM generation. The low frequency gain is 31.3 ms/V. Notice that the notches are, as expected, at multiples of the inverse of the integration period ( $\frac{1}{1.8 \text{ ms}} = 555.5 \text{ Hz}$ ) and thus do not affect the target signal bandwidth. The total power consumption of the analogue subsystem is 280  $\mu\text{W}$  from a 10 V supply. The digital subsystem consumes 15.4 mW from a 5 V supply. The system achieves experimentally 67.4 dB CMRR, 58.9 dB PSRR and 16.5  $M\Omega$  input impedance at 50 Hz with 1 kHz chopping.

### 5.4.2 *In-vivo* characterization

The *in-vivo* measurements are performed connecting our system to the test subject using wet electrodes (Kendall's H124SG) placed on the chest with a spacing of about 5 cm. A third body electrode acts as the ground electrode (which for simplicity is not shown in Figure 5.1). The output data are acquired using a Digilent® Analog Discovery 2 board for a period of 10 s. The output spectrum is filtered using MATLAB® with a Butterworth filter in the band 1-100 Hz. The ECG signal is reconstructed by dividing the output signal by the previously recorded full chain gain, to obtain the input referred ECG signal. Figure 5.7 (top panel in blue) shows an *in-vivo* experiment measuring the cardiac activity of a person. These data in the PWM output format is stored and is given as input to the digital subsystem. Figure 5.7 (bottom panel in red) shows the reconstructed signal obtained by the Manchester encoded serial digital output.

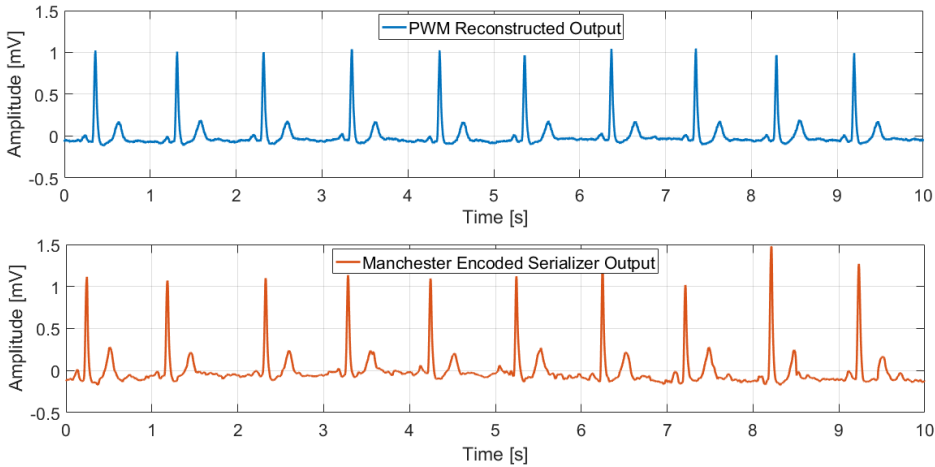


**Figure 5.7:** (Top panel) *In-vivo* ECG measured signal reconstructed from the output PWM, (Bottom panel) *In-vivo* ECG measured signal reconstructed from Manchester encoded output.

In Figure 5.8, a segment of the 105.9 kb/s Manchester encoded bit stream corresponding to the *in-vivo* measurement is displayed. The bit stream corresponding to the digitization of one sample is repeated three times in order to reduce errors in the NFC transmission. The sampling frequency of the input signal is 250 Hz,

while the Manchester encoded bit stream is generated at 105.9 kb/s, hence, there is sufficient time to repeat each sampled value three times. Figure 5.9 shows the foil micrograph of the presented system. The total area of the foil is 123.4 mm<sup>2</sup>.



**Figure 5.8:** Manchester encoded output corresponding to three samples of the in-vivo measurement and a zoom-in of the Manchester encoding of the output bits.

Table 5.2 provides a performance summary and comparison to prior literature. This work is the first reported circuit on foil to date capable to convert a bio-potential input signal to the digital domain. Additionally, it generates a 105.9 kb/s Manchester encoded bit stream compatible with the NFC standard. Some of the initial steps taken in the direction of bio-signal acquisition systems using flexible TFT technologies have been published in literature for EEG [20], EMG [21, 22], ECG [23] and Heart-Rate (HR) [24] measurements. Comparing our contribution to existing literature on flexible TFTs circuits, in references [20, 21, 22, 23] the signal is not digitized. A recently published frontend [23] is able to acquire ECG

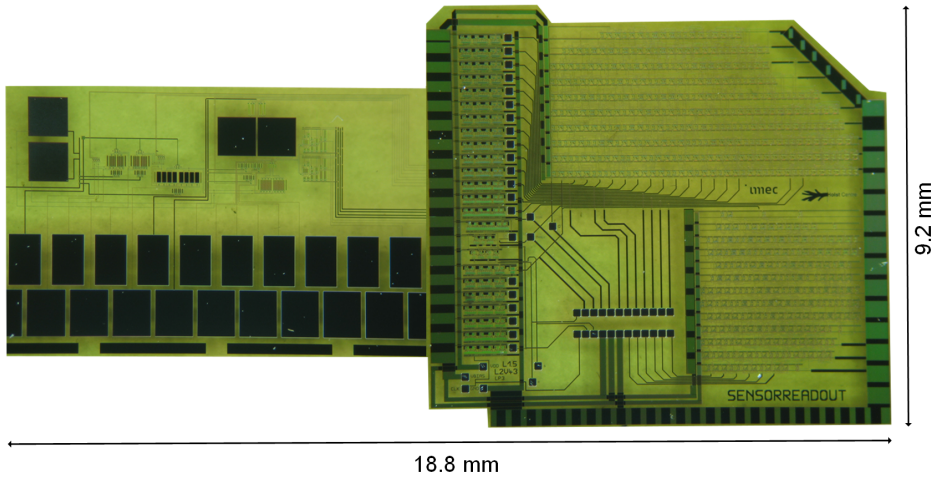


*Figure 5.9: Foil micrograph of the presented system.*

using a flexible TFT based amplifier, but it also does not digitize the signal. An HR readout on flexible foil [24] was able to convert the signal to binary levels, encoding it in the transition times (i.e. PWM output representation), but was lacking a time-sampled digital output representation (i.e. in bits), which is needed to be compatible with most modern wireless transmission systems. Compared to [24] (described in Chapter 4), we have included in this work a digital subsystem (consisting of a 10 bit counter, serializer with Manchester encoder, clock divider and digital phase generator) which transforms the PWM to a time-sampled digital format. The digital clock signals needed to operate the full system are also generated on the foil. Apart from this, the integrated input referred noise in [24] is  $186.3 \mu V_{rms}$ , which is too high to perform ECG measurements, enabling only HR measurements. Within the analogue frontend we have, thus, implemented in the present work a low pass filter after the cascaded preamplifier, which limits in band noise and noise aliasing, and enables  $8 \mu V_{rms}$  input equivalent noise in the 1-100 Hz bandwidth: a performance that is now compatible with ECG measurements. The input signal is transformed to PWM without digitalization in [25] too, and that circuit does not provide a voltage, but rather a current input, making it unsuited to measure bio-potential signals. The flexible ECG patch described in this

Chapter achieves experimentally NEF and PEF equal to 109.81 and  $1.20 \times 10^5$  respectively. These figures provide an improvement of 13% and 86% in NEF and PEF respectively, compared to the best NEF and PEF reported for previous bio-signal acquisition front-ends implemented using flexible TFTs [20]. These advancements are obtained due to both, a better TFT technology and circuit improvements. The self-aligned a-IGZO technology used in this work has indeed a better Hooge factor, thus providing less  $1/f$  noise. Besides, the larger input transconductance obtained, thanks to the use of the double gate TFT architecture, benefits the noise and power efficiency of the front-end.

## 5.5 Conclusions

This Chapter presents the first, fundamental steps to demonstrate intelligent plasters for biomedical applications based on flexible electronics which are compatible with the NFC standard. The presented approach provides a digitization strategy using a time reference, without the need for a voltage reference, and thus is particularly suited to implementation with a-IGZO TFTs on foil. The analogue frontend has a measured input-referred noise of  $8 \mu V_{rms}$  in the 1-100 Hz band, which is the lowest input-referred noise reported in a-IGZO TFT circuits so far [6, 7, 8, 22, 24, 25, 26]. The system achieves experimentally 67.4 dB CMRR, 58.9 dB PSRR and  $16.5 M\Omega$  input impedance at 50 Hz with 1 kHz chopping. The output is transformed to the digital domain and provided as a 105.9 kb/s Manchester-encoded serial bit stream. To the best of authors' knowledge, this is the first demonstrated ECG acquisition system in flexible a-IGZO TFTs on foil providing a digital serial output bit stream compatible with the NFC standard [6, 7, 8, 20, 21, 22, 23, 24, 25, 26]. The power consumption is 15.4 mW for the digital and  $280 \mu W$  for the analogue part. The NEF and PEF are 109.81 and  $1.20 \times 10^5$  respectively, which are the best values reported in literature for a-IGZO TFT circuits to date [6, 7, 8, 20, 21, 22, 23, 24, 25, 26].

Table 5.2: Comparison with the state-of-the-art

	JSSC'17[20]	ISSCC'17[25]	ESSCIRC'18[24]	SSCL'18[22]	Nature Electronics'19[23]	Flexible ECG Patch
Technology	a-Si	a-IGZO	a-IGZO	a-IGZO	DNTT	Dual Gate Self Aligned a- IGZO Chopped Amplifier + Low Pass Filter + Reset Integrator + 10 Bit Counter + Serializer + Manchester Encoder + Clock Divider + Digital Phase Generator
Architecture	Chopped Amplifier	Asynchronous Sigma Delta Modulator	Chopped Amplifier + Reset Integrator	Chopped Amplifier with Frequency Division Multiplexing	Amplifier with AC Coupled Load	1.5
Minimum Channel Length [ $\mu m$ ]	6	15	15	15	10	Voltage
Input Domain	Voltage	Current	Voltage	Voltage	Voltage	Digital
Output Type	Analogue	PWM	PWM	Analogue	Analogue	ECG
Application	EEG	Temp. Sensor	HR	EMG	ECG	1
Chopping Frequency [kHz]	5	-	0.5	5	-	8 (100 Hz)
Integrated Noise [ $\mu V_{rms}$ ](BW)	2.3 (100 Hz)	-	186.3 (200 Hz)	125 (500 Hz)	-	67.4 @ 50 Hz
CMRR [dB]	<50 @ 50 Hz	-	-	-	44 @ 50 Hz	58.9 @ 50 Hz
PSRR [dB]	-	-	-	-	-	16.5 @ 50 Hz
Input Impedance [ $M\Omega$ ]	-	-	-	29	-	109.81
NEF (Frontend)	126.29	-	454.29	1534.80	-	1.20x10 <sup>5</sup>
PEF (Frontend)	8.77x10 <sup>5</sup>	-	2.06x10 <sup>6</sup>	6.12x10 <sup>7</sup>	-	10 <sup>a</sup> 5 <sup>d</sup>
Supply Voltage [V]	55	20	10	26	4	0.28 <sup>a</sup> 15.4 <sup>d</sup>
Power Dissipation [mW]	11	2	0.052	1.3	-	24 <sup>a</sup> 99.3 <sup>d</sup>
Area [ $mm^2$ ]	-	27.9	52.5	11.2	-	

<sup>a</sup> Analogue <sup>d</sup> Digital

## Bibliography

- [1] M. Zulqarnain, S. Stanzione, G. Rathinavel, S. Smout, M. Willegems, K. Myny, and E. Cantatore, "A flexible ECG patch compatible with NFC RF communication," *npj Flexible Electronics*, vol. 4, pp. 1–8, July 2020.
- [2] S. Park and S. Jayaraman, "Enhancing the quality of life through wearable technology," *Engineering in Medicine and Biology Magazine, IEEE*, vol. 22, pp. 41 – 48, 06 2003.
- [3] A. Pantelopoulos and N. Bourbakis, "A survey on wearable sensor-based systems for health monitoring and prognosis," *IEEE Transactions on Systems, Man, and Cybernetics, Part C (Applications and Reviews)*, vol. 40, pp. 1–12, Jan. 2010.
- [4] N. V. Helleputte, M. Konijnenburg, H. Kim, J. Pettine, D.-W. Jee, A. Breeschoten, A. Morgado, T. Torfs, H. de Groot, C. V. Hoof, and R. F. Yazicioglu, "A multi-parameter signal-acquisition SoC for connected personal health applications," in *2014 IEEE International Solid-State Circuits Conference Digest of Technical Papers (ISSCC)*, pp. 314–315, IEEE, Feb. 2014.
- [5] W.H.O., "Cardiovascular Diseases," [https://www.who.int/health-topics/cardiovascular-diseases/#tab=tab\\_1](https://www.who.int/health-topics/cardiovascular-diseases/#tab=tab_1), 2017. [Online; accessed 28-August-2019].
- [6] Y. Khan, A. E. Ostfeld, C. M. Lochner, A. Pierre, and A. C. Arias, "Monitoring of vital signs with flexible and wearable medical devices," *Advanced Materials*, vol. 28, no. 22, pp. 4373–4395, 2016.
- [7] Y. Khan, M. Garg, Q. Gui, M. Schadt, A. Gaikwad, D. Han, N. A. D. Yamamoto, P. Hart, R. Welte, W. Wilson, S. Czarnecki, M. Poliks, Z. Jin, K. Ghose, F. Egitto, J. Turner, and A. C. Arias, "Flexible hybrid electronics: Direct interfacing of soft and hard electronics for wearable health monitoring," *Advanced Functional Materials*, vol. 26, no. 47, pp. 8764–8775, 2016.
- [8] J. C. Costa, F. Spina, P. Lugoda, L. Garcia-Garcia, D. Roggen, and N. Münzenrieder, "Flexible sensors—from materials to applications," *Technologies*, vol. 7, p. 35, Apr. 2019.

- [9] T. Sekitani, T. Yokota, K. Kuribara, M. Kaltenbrunner, T. Fukushima, Y. Inoue, M. Sekino, T. Isoyama, Y. Abe, H. Onodera, and T. Someya, "Ultraflexible organic amplifier with biocompatible gel electrodes," *Nature Communications*, vol. 7, p. 11425, Apr. 2016.
- [10] Y. Wang, Y. Qiu, S. K. Ameri, H. Jang, Z. Dai, Y. Huang, and N. Lu, "Low-cost,  $\mu\text{m}$ -thick, tape-free electronic tattoo sensors with minimized motion and sweat artifacts," *npj Flexible Electronics*, vol. 2, p. 6, Feb. 2018.
- [11] J. H. Koo, S. Jeong, H. J. Shim, D. Son, J. Kim, D. C. Kim, S. Choi, J.-I. Hong, and D.-H. Kim, "Wearable electrocardiogram monitor using Carbon nanotube electronics and color-tunable organic light-emitting diodes," *ACS Nano*, vol. 11, pp. 10032–10041, Oct. 2017.
- [12] J. Kim, M. Lee, H. J. Shim, R. Ghaffari, H. R. Cho, D. Son, Y. H. Jung, M. Soh, C. Choi, S. Jung, K. Chu, D. Jeon, S.-T. Lee, J. H. Kim, S. H. Choi, T. Hyeon, and D.-H. Kim, "Stretchable Silicon nanoribbon electronics for skin prosthesis," *Nature Communications*, vol. 5, p. 5747, Dec. 2014.
- [13] D. Khodagholy, T. Doublet, P. Quilichini, M. Gurfinkel, P. Leleux, A. Ghestem, E. Ismailova, T. Hervé, S. Sanaur, C. Bernard, and G. G. Malliaras, "In vivo recordings of brain activity using organic transistors," *Nature Communications*, vol. 4, p. 1575, Mar. 2013.
- [14] X. Wang, Y. Gu, Z. Xiong, Z. Cui, and T. Zhang, "Silk-molded flexible, ultrasensitive, and highly stable electronic skin for monitoring human physiological signals," *Advanced Materials*, vol. 26, no. 9, pp. 1336–1342, 2014.
- [15] S. Wang, J. Xu, W. Wang, G.-J. N. Wang, R. Rastak, F. Molina-Lopez, J. W. Chung, S. Niu, V. R. Feig, J. Lopez, T. Lei, S.-K. Kwon, Y. Kim, A. M. Foudéh, A. Ehrlich, A. Gasperini, Y. Yun, B. Murmann, J. B.-H. Tok, and Z. Bao, "Skin electronics from scalable fabrication of an intrinsically stretchable transistor array," *Nature*, vol. 555, pp. 83–88, Mar. 2018.
- [16] W.-H. Yeo, Y.-S. Kim, J. Lee, A. Ameen, L. Shi, M. Li, S. Wang, R. Ma, S. H. Jin,

- Z. Kang, Y. Huang, and J. A. Rogers, "Multifunctional epidermal electronics printed directly onto the skin," *Advanced Materials*, vol. 25, no. 20, pp. 2773–2778, 2013.
- [17] J. G. Webster, *Medical Instrumentation: Application and Design*. John Wiley & Sons, 2009.
- [18] K. Myny, Y.-C. Lai, N. Papadopoulos, F. D. Roose, M. Ameys, M. Willegems, S. Smout, S. Steudel, W. Dehaene, and J. Genoe, "A flexible ISO14443-a compliant 7.5 mW 128b metal-oxide NFC barcode tag with direct clock division circuit from 13.56 MHz carrier," in *2017 IEEE International Solid-State Circuits Conference (ISSCC)*, pp. 258–259, IEEE, Feb. 2017.
- [19] AAMI, "Diagnostic electrocardiographic devices," *ANSI/AAMI EC11. Association for the Advancement of Medical Instrumentation*, Arlington, VA, 2001.
- [20] T. Moy, L. Huang, W. Rieutort-Louis, C. Wu, P. Cuff, S. Wagner, J. C. Sturm, and N. Verma, "An EEG acquisition and biomarker-extraction system using low-noise amplifier and compressive-sensing circuits based on flexible, thin-film electronics," *IEEE Journal of Solid-State Circuits*, vol. 52, pp. 309–321, Jan. 2017.
- [21] H. Fuketa, K. Yoshioka, Y. Shinozuka, K. Ishida, T. Yokota, N. Matsuhisa, Y. Inoue, M. Sekino, T. Sekitani, M. Takamiya, T. Someya, and T. Sakurai, "1  $\mu\text{m}$ -thickness ultra-flexible and high electrode-density surface electromyogram measurement sheet with 2 V organic transistors for prosthetic hand control," *IEEE Transactions on Biomedical Circuits and Systems*, vol. 8, pp. 824–833, Dec. 2014.
- [22] C. Garripoli, S. Abdinia, J.-L. J. P. van der Steen, G. H. Gelinck, and E. Cantatore, "A fully integrated 11.2 mm<sup>2</sup> a-IGZO EMG front-end circuit on flexible substrate achieving up to 41 dB SNR and 29 M $\Omega$  input impedance," *IEEE Solid-State Circuits Letters*, vol. 1, pp. 142–145, June 2018.
- [23] M. Sugiyama, T. Uemura, M. Kondo, M. Akiyama, N. Namba, S. Yoshimoto, Y. Noda, T. Araki, and T. Sekitani, "An ultraflexible organic differential amplifier for recording electrocardiograms," *Nature Electronics*, vol. 2, pp. 351–360, Aug. 2019.
- [24] M. Zulqarnain, S. Stanzione, J.-L. P. V. D. Steen, G. H. Gelinck, K. Myny, S. Abdinia, and E. Cantatore, "A 52  $\mu\text{W}$  heart-rate measurement interface fabricated on a flexible

- foil with a-IGZO TFTs,” in *ESSCIRC 2018 - 44th European Solid State Circuits Conference (ESSCIRC)*, pp. 222–225, IEEE, Sept. 2018.
- [25] C. Garripoli, J.-L. P. J. van der Steen, E. Smits, G. H. Gelinck, A. H. M. V. Roermund, and E. Cantatore, “An a-IGZO asynchronous delta-sigma modulator on foil achieving up to 43 dB SNR and 40 dB SNDR in 300 Hz bandwidth,” in *2017 IEEE International Solid-State Circuits Conference (ISSCC)*, pp. 260–261, IEEE, Feb. 2017.
- [26] K. Myny, “The development of flexible integrated circuits based on thin-film transistors,” *Nature Electronics*, vol. 1, pp. 30–39, Jan. 2018.



# Chapter 6

## A Multichannel EOG Acquisition System based on Flexible TFTs and CMOS Technologies

*This Chapter demonstrates a fully integrated 8 channel Electro-oculography (EOG) acquisition system that exploits a front-end in a-IGZO technology, interfaced with a custom Si IC that supports the frontend and provides conversion of the acquired signals to the digital domain. In this way the low cost, flexible form factor and the large area character of the flexible TFT technology are leveraged, while exploiting the accuracy, computational capability and energy efficiency of the Si IC. More specifically, the Si IC controls a high pass filter, which is implemented with TFTs, providing a very low high-pass frequency. Also, the Si IC enables conversion to the digital domain with much higher efficiency compared to the TFT solution previously discussed in Chapter 5. Thus, from the circuit perspective, we have enabled an integrated high pass filter, while from the system perspective, we explore the combination of TFT and Si technologies to decrease power consumption.*

## 6.1 Introduction

Wearable devices using flexible technologies for health monitoring have become a topic of growing research interest, with applications including Electroencephalography (EEG) [1], Electromyography (EMG) [2, 3, 4] and Electrocardiography (ECG) [5]. This Chapter presents a multichannel Electro-oculography (EOG) acquisition system based on a-IGZO TFTs and Si IC Technology.

The flexible form factor of TFTs can be used to improve interfacing with the human body, resulting in better signal-to-noise ratio and improved user comfort. However, the inherently poor device performance of flexible TFT technologies results in limited electronic functionality. On the other hand, Si ICs can provide superior computational functionality at a comparatively lower power than flexible electronic devices. Hence, conventional Si ICs are well suited for the signal processing and data transmission. Thus, to optimize the performance of bio-signal acquisition systems, the flexibility, conformability and large area character of the flexible devices should be combined with the better signal processing capability and higher efficiency of conventional Si ICs to realize flexible hybrid electronics (FHE) systems.

FHE systems are especially well suited for applications where large area coverage or high channel count for signal acquisition is required, such as in EEG and EMG acquisition systems. If these applications are implemented using only Si ICs, the bond pad area for input connections to the electrodes can dominate the total chip area. Thus, implementation of a large number of channels leads to higher costs. Using TFTs for the front-end allows concentration of the signals from many channels on a small number of interconnects and thus enables smaller Si ICs. The added cost of TFT electronics is typically negligible, given the very low price per unit area that these technologies offer. Therefore, a hybrid solution combining flexible and rigid electronics is attractive in terms of patient comfort, performance and cost, where flexible devices are used for soft interfaces and hard electronics are used for computation, signal processing, and data transmission as shown in

a representative scenario depicted in Figure 6.1. One point to be taken into consideration while dealing with FHE systems is that they might not offer the lowest cost solution compared to flexible only systems, but they provide a very interesting tradeoff between performance and cost.

This Chapter presents a fully integrated 8 channel FHE EOG acquisition system based on double gate self aligned a-IGZO technology, interfaced with a custom Si IC used for backend operations.

EOG is a well known approach of non-invasively monitoring eye movement activity [6]. The EOG measurements are based on electrical signals that are generated due to cornea-retina dipole when the eye moves. These bio-signals can be acquired by attaching pairs of electrodes across the eyes. The primary applications of EOG are related to ophthalmological diagnosis and eye movement recording. The EOG acquisition systems can be further used for various applications e.g. cognitive and perception studies in neuroscience [7], mental health monitoring [8], quantitative evaluation of neurodegenerative diseases [9], sleep studies [10], human-computer interaction (HCI) [11] etc.

The rest of the Chapter is organized as follows: Section 6.2 discusses the system architecture and circuit design of the implemented system. The experimental measurement results are shown in Section 6.3. Finally, Section 6.4 concludes the Chapter.

## 6.2 System architecture

The specifications of systems dedicated to EOG recording applications are regulated by the ISCEV standard [12]. In human beings, the EOG signal ranges from 0.05 mV to 3.5 mV, with a typical bandwidth of DC to 50 Hz [6]. However, the main signal bandwidth of eye movement is located in the range of 0.1 Hz to 30 Hz. In practice, the high cut off frequency should be preferably above 70 Hz to acquire all the signal details [13]. For a 30° eye movement, the typical EOG ampli-

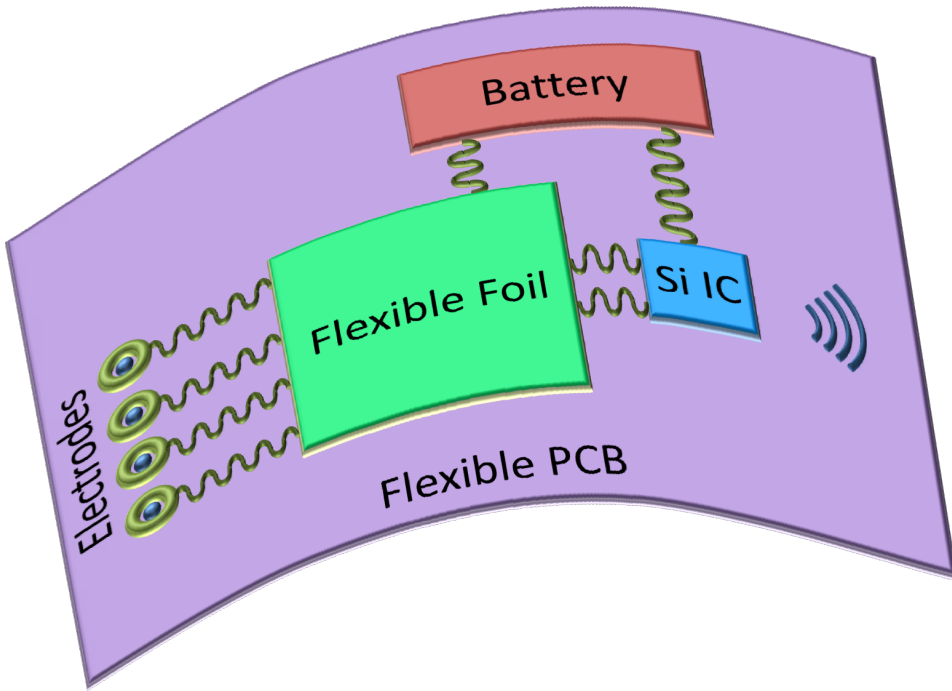


*Figure 6.1: Representative integration of the flexible hybrid system.*

tude is between  $250 \mu V$  and  $1000 \mu V$ , with an essential frequency content in the band 0.1–30 Hz. The electrode–skin contact impedances should be below  $5 k\Omega$  as measured between 20 and 40 Hz [12].

The full system architecture is shown in Figure 6.2. It consists of 8 channels for signal acquisition. Each channel of the analogue frontend (AFE) consists of an input chopper ( $CH_{in}$ ), a 2-stage cascaded diode connected load preamplifier ( $A_{1,2}$ ), a de-chopper ( $CH_{out}$ ), and a low pass filter,  $A_3$ , loaded by  $C_i$ . The channels are AC coupled through a tunable hybrid high pass filter (HPF). All the channels are time-multiplexed through a multiplexer (MUX) to a reset integrator. The outputs of the reset integrator are fed to the gates of TFTs which act as transconductors. The output currents of these TFTs along with a reference current, are interfaced to the Si backend. The clock phases required for the analogue subsystem functional-

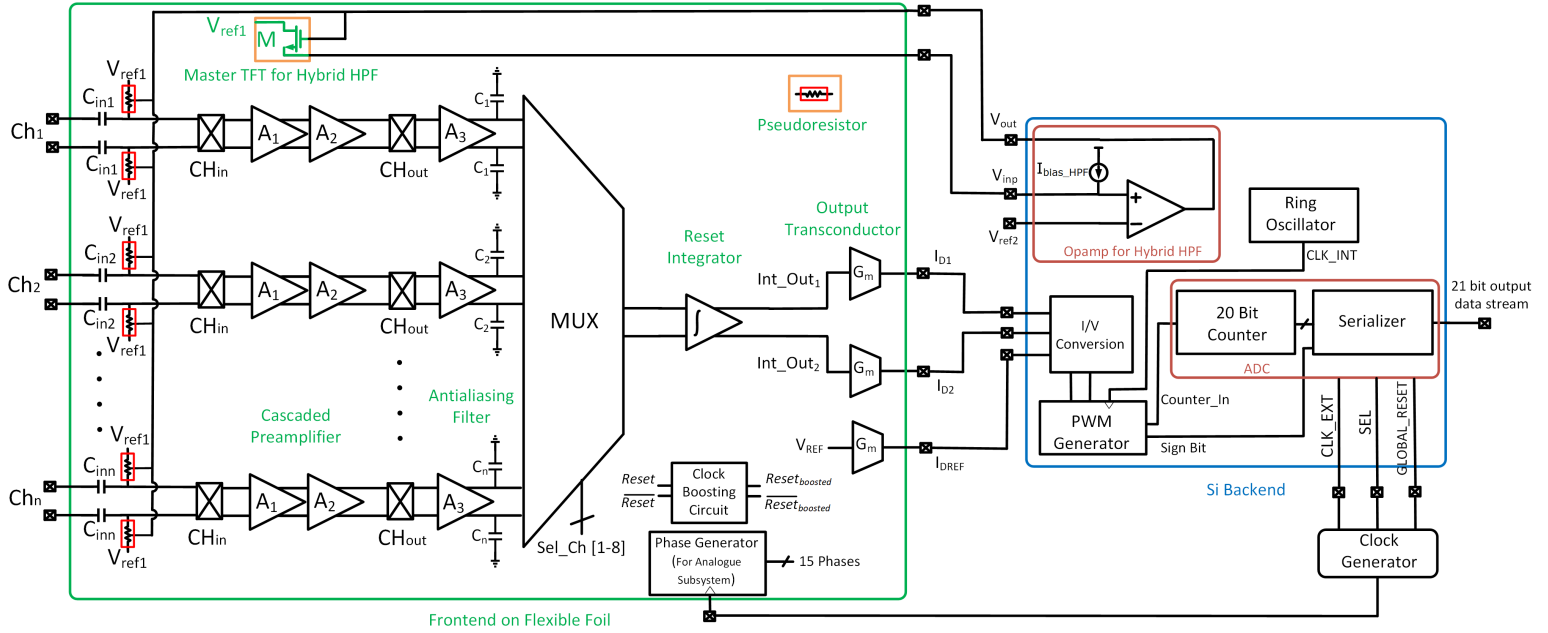


Figure 6.2: System architecture of the flexible hybrid system.

ity are generated on the foil by a Phase Generator, while a Clock Boosting circuit provides voltage boosted reset signals ( $0 - \sim 2V_{DD}$ ) for the integrator reset. The Si backend input consists of an I/V conversion block to interface the TFT and Si subsystems. There is basically only one differential signal and a reference interconnect ( $I_{D1}, I_{D2}$  and  $I_{DREF}$ ) required between TFT and Si subsystems, which reduces the area needed for interconnections on the Si chip, and thus cost. After conversion to the voltage domain in the Si IC, the output is fed to a PWM Generator where a PWM representation of each channel (PWM\_Out) is generated with an additional Sign Bit. The result of an AND between the internal clock (CLK\_INT) and PWM\_Out, called Counter\_In, is used as input for a 20 bit Counter. The output bits of the Counter along with the Sign Bit are serialized to generate a 21 bit digital serial output bit stream. More details on the main sub-blocks are provided in the following Sections.

### 6.2.1 Hybrid high pass filter

In biomedical applications, HPF at the input of the signal processing chain are typically used to reject the electrode offset and provide a suitable signal filtering. Due to the very large times constants required, these filters are often implemented with capacitors and pseudoresistors. This is even more the case in TFT technologies, where no highly resistive layer is typically available, and capacitors have a low capacitance per unit area. The problem of pseudoresistors, however, is their high sensitivity to process variations, and the lack of a simple way to tune their value. To solve these problems, we propose here a novel approach that exploits the presence of Si components in the system.

The proposed hybrid HPF consists of TFT based pseudoresistors and integrated on-foil capacitors with a feedback loop, using a CMOS based op-amp in the Si IC, to tune the gate voltages of the pseudoresistors as shown in Figure 6.3. An on-chip bias current  $I_{bias\_HPF}$ , generated using the current reference described in Section

6.2.3, flows through the master TFT consisting of  $M$  TFTs  $T_{m\_1-M}$  in parallel. The output of the op-amp tunes the gate voltages of the master TFTs, which in turn are used to tune the gate voltages of the pseudoresistors used in the signal chain, consisting of  $N$  TFTs  $T_{chi\_p/n\_s\_1-N}$  in series. The op-amp is implemented with a standard folded cascode topology. The equivalent resistance of the pseudoresistor is given by:

$$R_{eq} = \frac{(V_{ref2} - V_{ref1})}{I_{bias\_HPF}} \cdot M \cdot N \quad (6.1)$$

where  $V_{ref2} - V_{ref1}$  is the voltage difference across the master TFT,  $I_{bias\_HPF}$  is the on-chip bias current,  $M$  is the number of parallel TFTs in the master TFT, while  $N$  is the number of TFTs in series in the pseudoresistor. For illustration, if  $V_{ref2} - V_{ref1}$  is chosen to be 100 mV,  $I_{bias\_HPF}$  is 1 nA,  $M$  is 10 and  $N$  is 10,  $R_{eq}$  of 10  $G\Omega$  is achieved.

The obvious advantage of the hybrid HPF with tunable pseudoresistor is its robustness to parameter variations. A CMOS based op-amp is more robust compared to its TFT counterparts under variations due to process, supply voltage and temperature (PVT). The feedback loop will tune the gate voltages of the TFT based pseudoresistors across a wide range of parameter variations to match the desired value. Obviously, a residual cause of variability will be the mismatch between the unity elements of the pseudoresistors. In order to counteract this final variability source, the backgate voltages of the master TFTs ( $V_{BG0}$ ) and pseudoresistors ( $V_{BG\_chi\_p/n}$ ) are individually tunable.

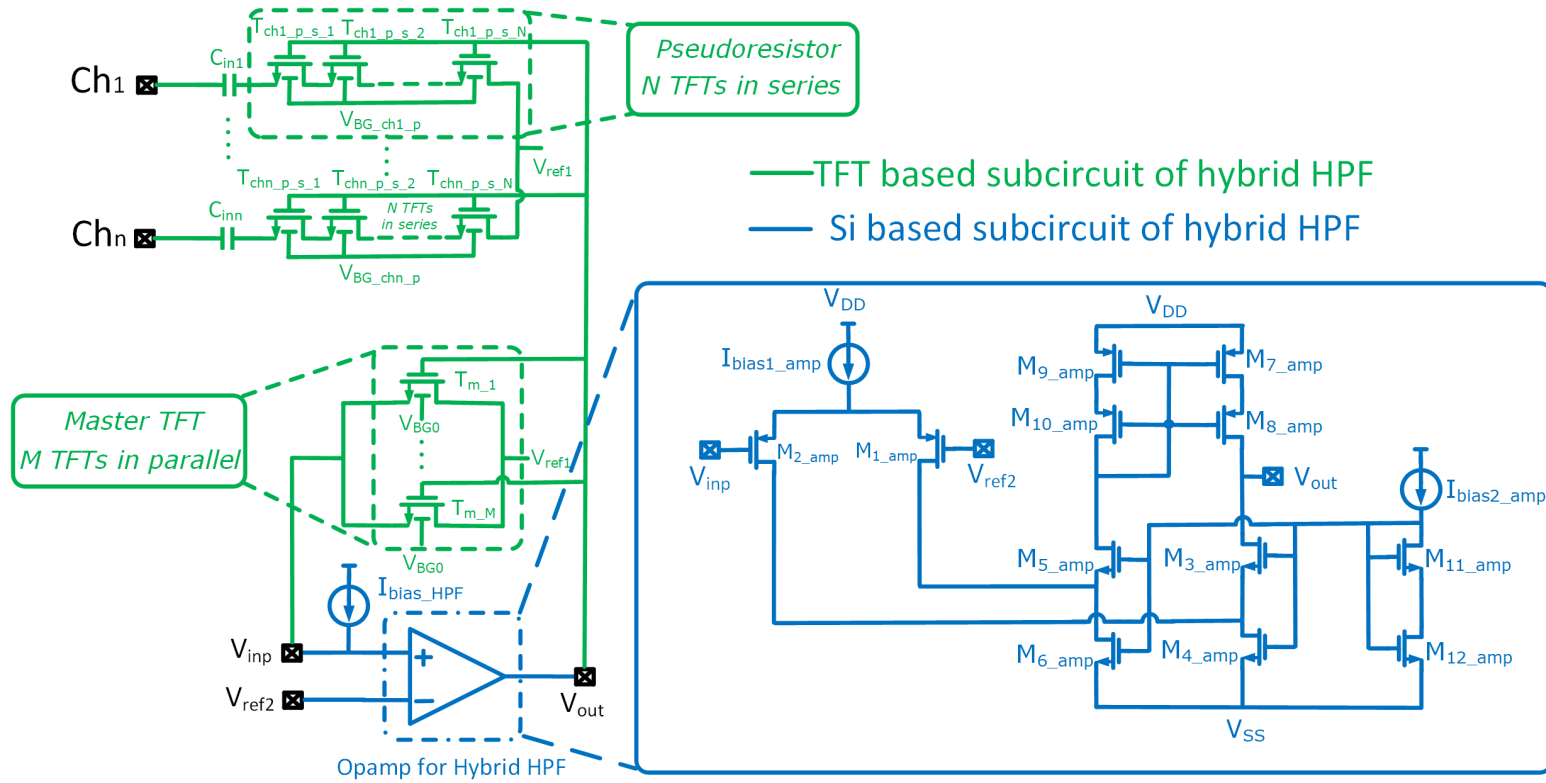
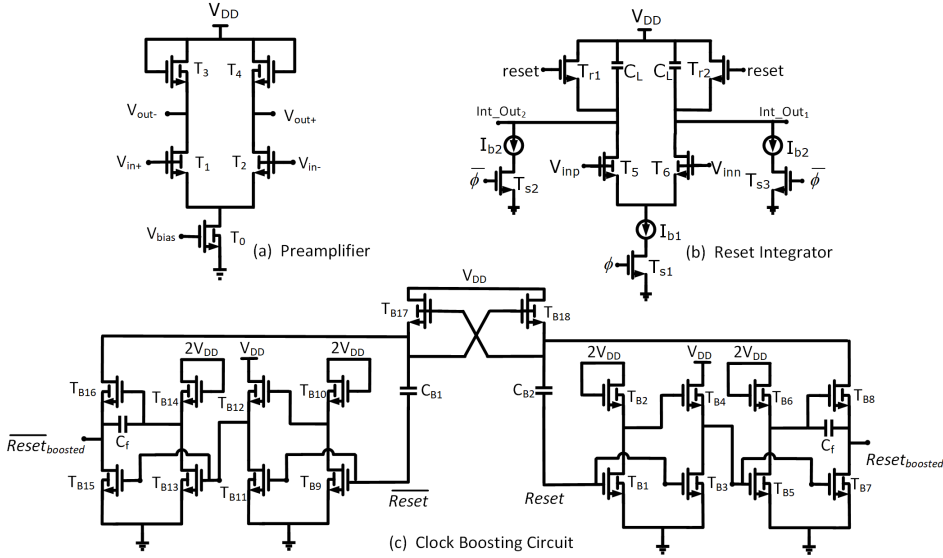


Figure 6.3: Architecture of the flexible hybrid HPF.

### 6.2.2 Frontend on flexible foil



**Figure 6.4:** Circuit schematic of analogue frontend (a) Schematic of the diode-connected load amplifier; (b) Reset integrator; (c) Clock boosting circuit.

The preamplifier is a 2-stage cascaded diode-connected load preamplifier, built using diode-connected load TFTs, as shown in Figure 6.4(a). The input TFTs  $T_{1,2}$  in  $A_1$  have a large area to reduce  $1/f$  noise. The second amplifier  $A_2$  has the same topology as  $A_1$  with different aspect ratios of the input pair. The output after the de-chopper is low-pass filtered by another differential amplifier,  $A_3$ , with diode connected load, which includes load capacitors to limit the bandwidth and noise folding in the reset integrator. All the 8 channels in the AFE are time multiplexed using a MUX, followed by the reset integrator (Figure 6.4(b)). The principle of operation of the reset integrator is the same as explained in Chapter 4. The integrator outputs are fed to gates of TFTs, functioning as transconductors ( $G_m$ ) (Figure 6.2). The output currents ( $I_{D1,2}$ ) from the integrator outputs along with a reference current ( $I_{DREF}$ ) are interfaced to the Si backend. Circuits consisting of TFTs generally require a high supply voltage due to thicker dielectrics used in flexible TFTs, while Silicon based circuits are operated at lower supply voltages. This inherent difference in supply voltage domains makes interfacing (especially in voltage domain)

of flexible circuits with Silicon based circuits in hybrid systems quite challenging. Hence, the interfacing between TFT and Si IC in this system has been implemented in the current domain.

The reset switches ( $T_{r1,2}$ ) in the reset integrator (Figure 6.4(b)) need to pull  $Int\_Out_{1,2}$  nodes to  $V_{DD}$ . As these are NMOS TFTs, they need to be switched on by clocks higher than  $V_{DD}$ . For this reason, these clocks are generated by the Phase Generator and then fed to the Clock Boosting circuit to get output voltage boosted clocks. The schematic of the Clock Boosting circuit is shown in Figure 6.4(c). This circuit uses two clock phases  $Reset$  and  $\overline{Reset}$  and operates as follows: during the on time of  $\overline{Reset}$ , TFT  $T_{B18}$  turns on and capacitor  $C_{B2}$  charges to  $V_{DD}$ . During  $Reset$ , TFT  $T_{B17}$  turns on and capacitor  $C_{B1}$  charges to  $V_{DD}$ . Capacitor  $C_{B2}$ , which was charged to  $V_{DD}$  during the previous clock phase, is now connected between  $V_{DD}$  and the drain of TFT  $T_{B8}$ , lifting the voltage at drain of TFT  $T_{B8}$  to  $2V_{DD}$ . Thus, the output pulse ( $Reset_{boosted}$ ) at the source of TFT  $T_{B8}$  is between  $V_{SS} - \sim 2V_{DD}$ .

The clock phases required for the functionality of the analogue frontend are also generated on-foil using the Phase Generator. The timing diagram for the frontend functionality is shown in Figure 6.5. It can be seen from Figure 6.5, that the reset period is  $500 \mu s$  (indicated by  $T_4$ ), phase  $\phi$  (the integration phase) is  $245 \mu s$  (indicated by  $T_2 - T_1$ ) and phase  $\bar{\phi}$  (the constant current discharge phase) is  $245 \mu s$  (indicated by  $T_3$ ). Each channel is active for  $495 \mu s$  and after one complete cycle (when all channels have been multiplexed), the  $Ch1\_flag$  signal is activated to indicate the start of a new acquisition cycle. The Phase Generator block is designed by the imec Leuven team leaded by Kris Myny.

### 6.2.3 Silicon backend

#### Current reference

The current reference is a standard beta multiplier reference circuit, as shown in Figure 6.6. It consists of a current mirror composed of  $M_{1,2}$  and  $M_{3,4}$ . The start up circuit consists of  $M_{5-7}$  with  $M_{pc,nc}$  acting as MOS capacitors to  $V_{DD}$  and  $V_{SS}$

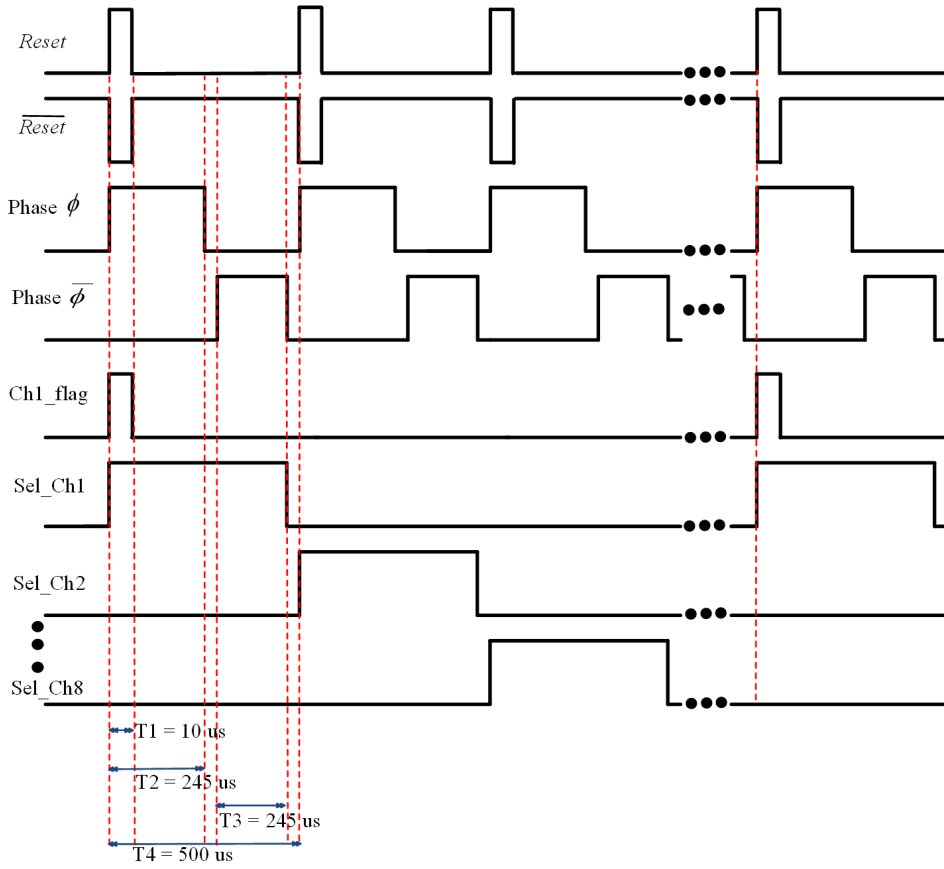


**Figure 6.5:** Timing diagram of the frontend on flexible foil.

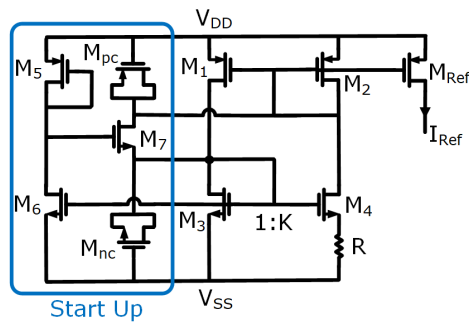


**Figure 6.6:** Circuit schematic of the current reference.

respectively. The reference current  $I_{Ref}$  can be written as:

$$I_{Ref} = \frac{V_t \ln K}{R} \quad (6.2)$$

where  $V_t$  is  $kT/q$ ,  $R = 1.06 \text{ M}\Omega$ ,  $K = 50$ , which results in a nominal  $I_{Ref} = 100 \text{ nA}$ .

### **I/V conversion for TFT-Si interface**

Figure 6.7a shows the circuit diagram of the current to voltage conversion block used at the TFT-Si interface. The PMOS based current mirrors  $M_{Is\_1,2}$  and  $M_{Is\_3,4}$  copy the TFT output currents  $I_{D1,2}$  (which are periodically reset ramp signals) and  $I_{DREF}$  inside the Si IC. The NMOS based current mirror formed by  $M_{Is\_5,6}$ , then performs a current comparison between  $I_{D1,2}$  and  $I_{DREF}$ , and a conversion to the voltage domain at its output. An over-voltage protection is provided at the TFT-Si interface terminals in the Si IC, to avoid potential over-voltages generated on the TFT side. This signal is then fed to 3 cascaded current-starved inverters, followed by inverters with gradually increased sizes. The input and output of the last stage inverter are finally fed to a latch to get the rail to rail outputs  $V_{OUT1}$  and  $V_{OUT2}$ . The delay time of the starved inverters is controlled by the bias current ( $I_{bias\_LS}$ ). This op-amp-less current to voltage conversion architecture is chosen for its power efficiency. Indeed, its simulated power consumption, for operation with TFT outputs at the nominal frequencies, is  $69.3 \mu\text{W}$ .

### **Ring oscillator**

Figure 6.7b shows the simplified circuit diagram of the ring oscillator. It comprises of an odd number of current-starved inverter stages followed by inverters with gradually increased sizes to drive the connected the feedback loop. The propagation delay time of a single inverter stage is controlled by the bias current ( $I_{bias\_RO}$ ). The ring oscillator is designed to provide a nominal clock frequency (CLK\_INT) of 10 MHz.

### **PWM generator**

The block diagram of the PWM Generator and 20 bit Counter and Serializer is shown in Figure 6.8. The PWM Generator consists of two D flip flops clocked by

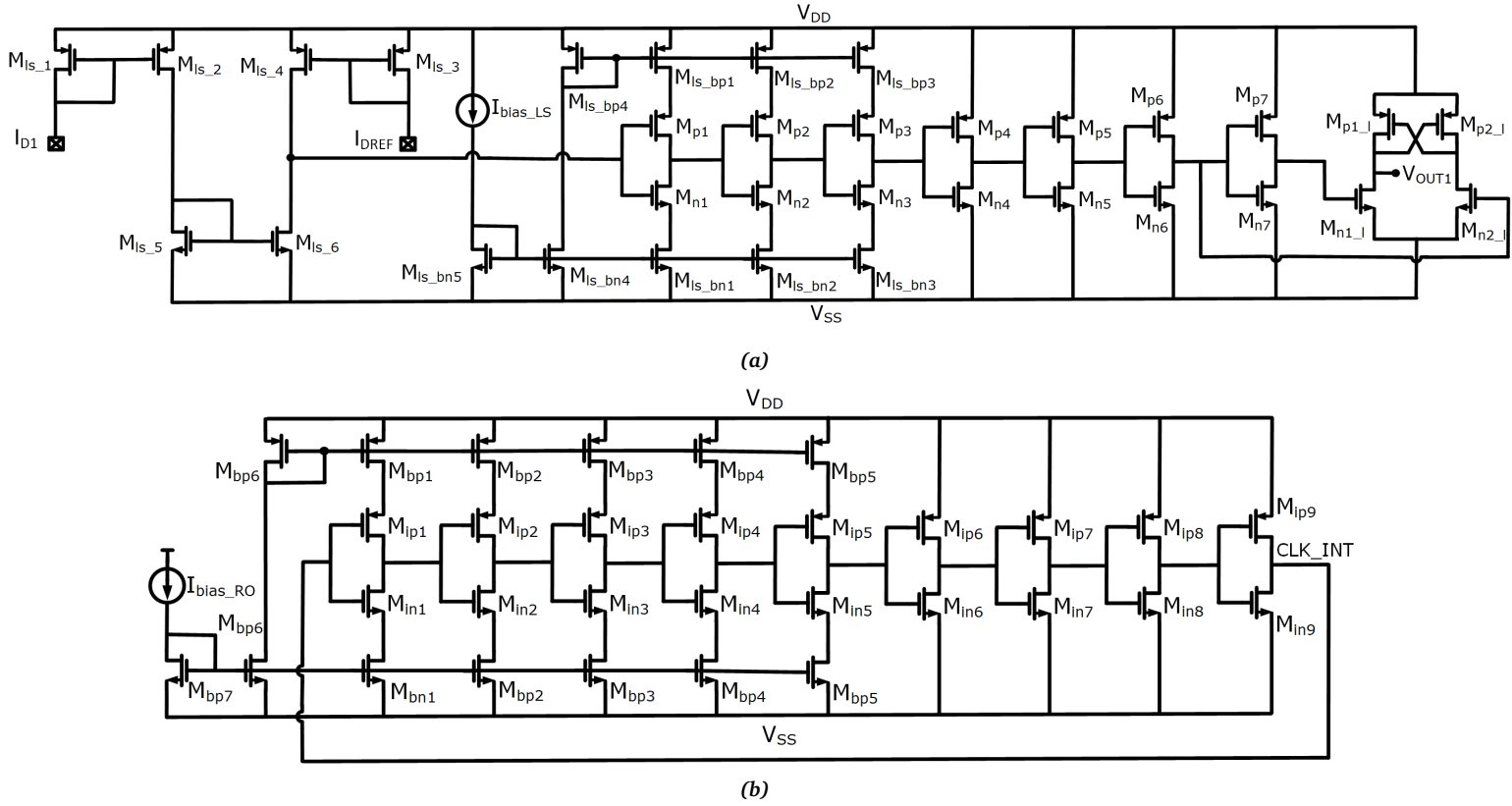


Figure 6.7: (a) Circuit schematic of the I/V conversion (single ended version shown for illustration), (b) Circuit schematic of the ring oscillator.

$V_{OUT1}$  and  $V_{OUT2}$ . The outputs of both the flip flops are Ored to get PWM\_Out (as shown in Figure 6.9) which is ANDed with CLK\_INT to finally get Counter\_In. GLOBAL\_RESET is used to periodically reset both the flip flops.

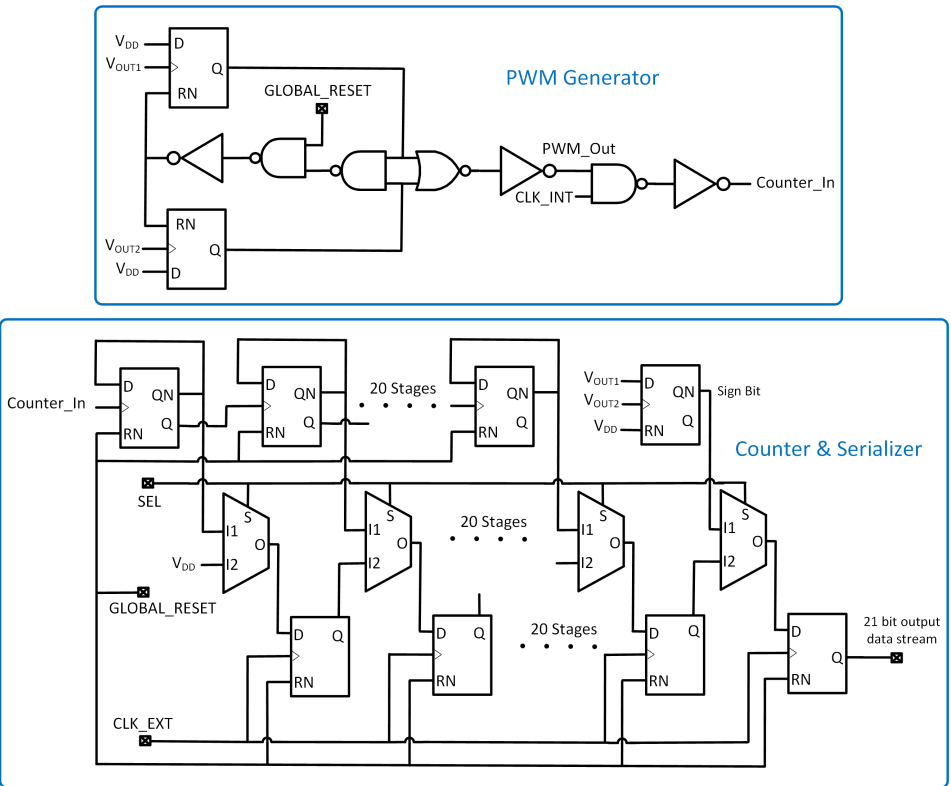
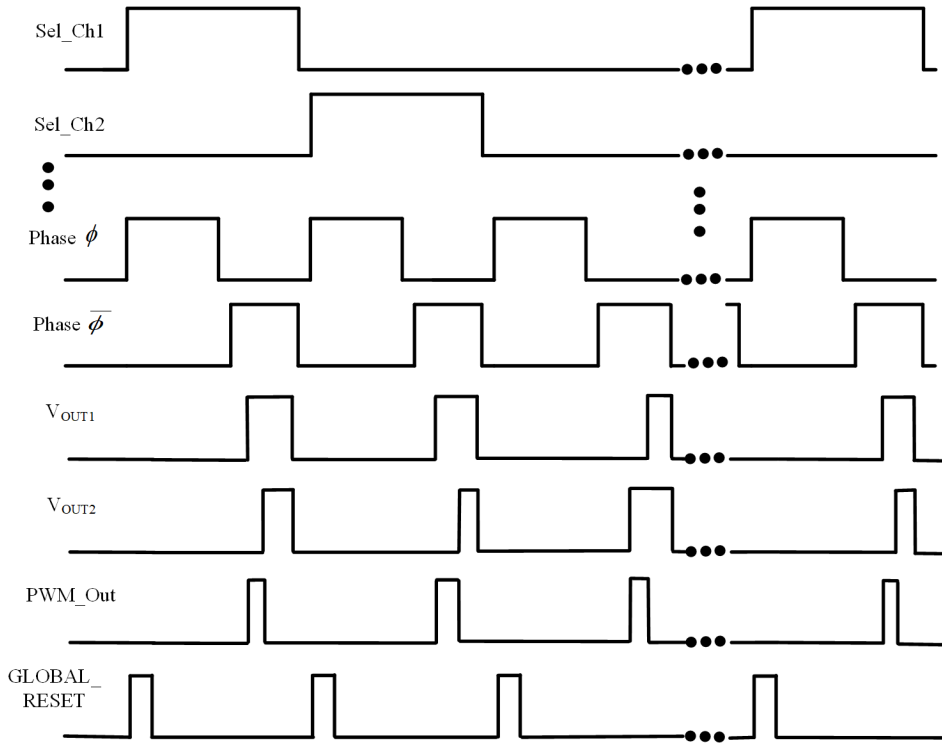


Figure 6.8: Circuit schematics of the PWM generator, counter and serializer.

### Counter and serializer

The output of the PWM Generator, Counter\_In is used as input to a 20 bit asynchronous ripple counter based on D flip flops. The SEL signal passes the counter output bits and additional Sign Bit to the Serializer to obtain a 21 bit output data stream. The Counter and Serializer are also periodically reset by the GLOBAL\_RESET.

The main timing waveforms of the Si backend are shown in Figure 6.10. After a channel is selected by Sel\_Chi signal, a PWM waveform (PWM\_Out) is generated as



*Figure 6.9: Timing diagram for the PWM generator block.*

explained in Figure 6.9, which in turn is clock gated to get Counter\_In, which goes to a counter. After the constant current discharge phase in the reset integrator (as explained in Chapter 4) for each channel, the SEL signal gets activated to push the bits stored in the counter to the serializer and obtain the serial output bit stream. Once a single channel is read out, the GLOBAL\_RESET signal gets activated to reset all the flip flops.

## 6.3 Measurement results

The frontend on flexible foil is fabricated using dual gate self aligned a-IGZO TFT technology from imec, Leuven while the Si backend is fabricated with a standard commercial 180 nm CMOS technology. The system micrograph is shown in Figure 6.11. The total area of the frontend on flexible foil is  $602.7 \text{ mm}^2$  ( $24.4 \text{ mm} \times$

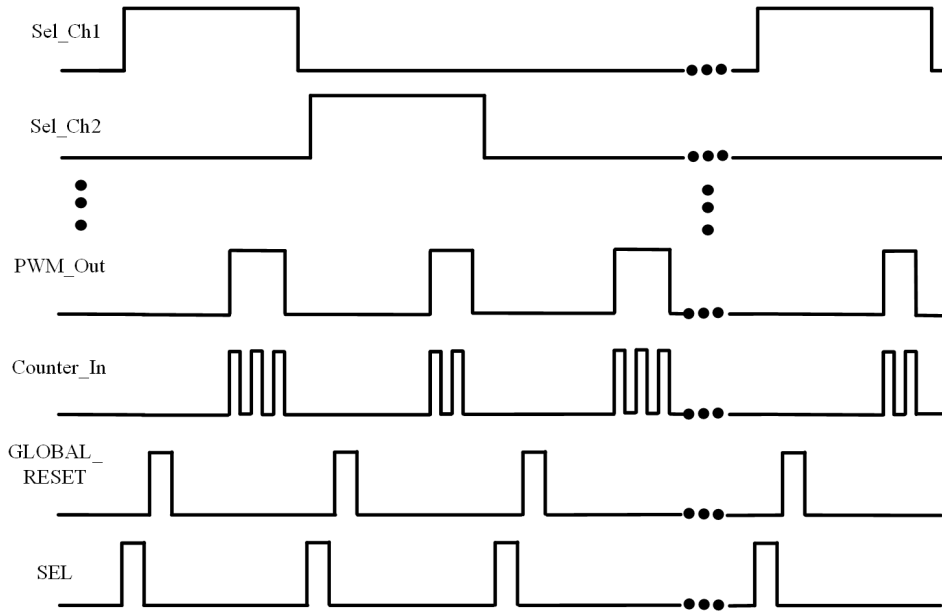


*Figure 6.10: Timing diagram for the Silicon backend.*

24.7 mm), while the Si backend takes  $1.44 \text{ mm}^2$  ( $1.2 \text{ mm} \times 1.2 \text{ mm}$ ) of area.

### 6.3.1 Preamplifier chain characterization

The preamplifier chain ( $A_{1-3}$ ) along with chopper and de-chopper has been characterized first stand-alone, connecting its output to voltage buffers (TI OPA445AP), followed by an instrumentation amplifier (TI INA111AP) for differential to single ended conversion. The supply voltage is 10 V. Figure 6.12 shows the measured transfer curve of the cascaded preamplifier  $A_{1-3}$ . It achieves a gain of 23.3 dB in a 510 Hz bandwidth with  $3.1 \mu\text{A}$  current consumption from 10 V supply. It should be emphasized here, that for this measurement, the capacitors at the output of  $A_3$  are 120 pF each, which results in rather large bandwidth. For the full system architecture, the  $A_3$  stage has been loaded with much higher capacitors to reduce the bandwidth and prevent aliasing in the reset integrator. From this measurement, the integrated input-referred noise in the 1-30 Hz signal BW is  $5.8 \mu\text{V}_{rms}$  with a chopping frequency of 1 kHz. The preamplifier chain achieves experimentally 70.6

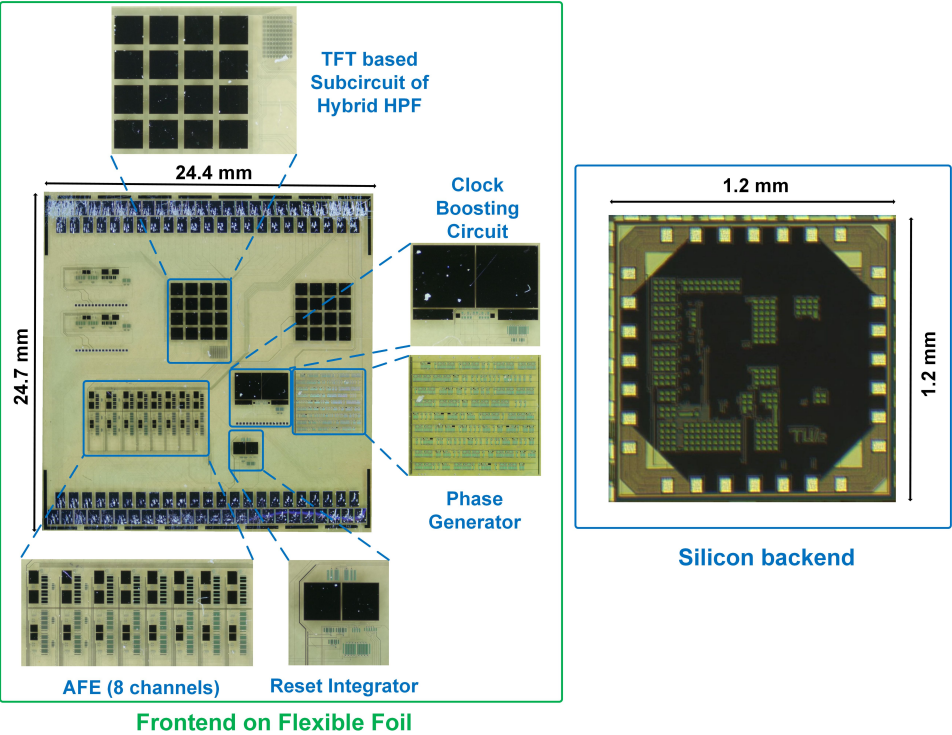


Figure 6.11: Micrograph of the full system including frontend on flexible foil and Silicon backend.

dB CMRR and 68.5 dB PSRR with 1 kHz chopping.

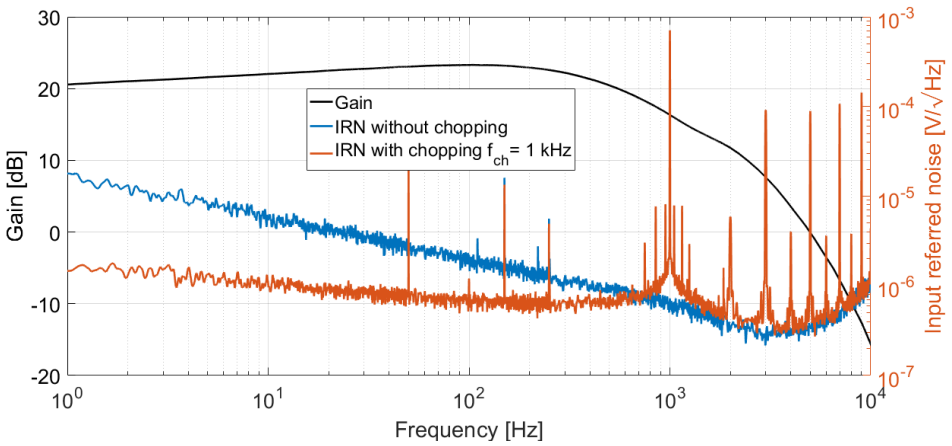


Figure 6.12: Measured frequency response and input-referred noise of the preamplifier chain ( $A_{1-3}$ ).

### 6.3.2 Full system characterization

The supply voltage ( $V_{DD}$ ) for the TFT based subsystem is 10 V w.r.t.  $V_{SS}$  of 0 V. The supply voltage ( $V_{DD}$ ) for the Si backend is 8.3 V w.r.t.  $V_{SS}$  of 5 V (i.e. 3.3 V operation). A 3.3 V Si technology (which has higher threshold voltage) has been chosen due to increased reliability and robustness required for interfacing with high voltage TFT technology. The  $V_{SS}$  of the Si IC has been selected to be equal to the half-rail voltage of the TFT foil ( $V_{ref1}$ ), to enable direct connection of the HPF control voltages generated on the Si IC to the TFT circuitry, avoiding any level shifting.

For the full system characterization, a  $5\text{ mV}_{p-p}$  sine wave with varying frequency was applied to the input of a single channel of the system and the output digital bit stream was observed. The output capacitors on the  $A_3$  stage in the full system are increased to 675 pF each on-foil, to reduce the signal bandwidth before the reset integrator. The midband gain is 25.9 ms/V with 0.035-75 Hz bandwidth as shown in Figure 6.13. The integrated input referred noise for the full system in 1-30 Hz BW is  $6.45\text{ }\mu\text{V}_{rms}$  with a chopping frequency of 1 kHz as shown in Figure 6.14. Figure 6.15 shows the measured channel crosstalk, when a  $5\text{ mV}_{p-p}$  10 Hz sine wave input is applied to channel 1. The outputs of channels 2-8 at the signal frequency are between 26.7 dB and 35.9 dB below the output of Channel 1.

It can be seen from the measurement in Figure 6.13 that the lower cut off frequency is as low as 0.035 Hz, thanks to the pseudoresistor and its control loop, including the Si IC. The integrated on-foil input capacitor  $C_{in}$  in hybrid HPF in each channel is 520 pF, which results in a pseudoresistor impedance of  $17.5\text{ G}\Omega$  at 0.035 Hz. Indeed, the input impedance of the system is dominated by the impedance of pseudoresistor. The power consumption for the frontend on flexible foil is 352  $\mu\text{W}$  (including all channels) from a supply voltage of 10 V, while the Si backend consumes 321.5  $\mu\text{W}$  from 3.3 V. Thus, the resulting total power consumption per channel is 84  $\mu\text{W}$ .

Table 6.1 presents a comparison between the FHE EOG system in this Chapter

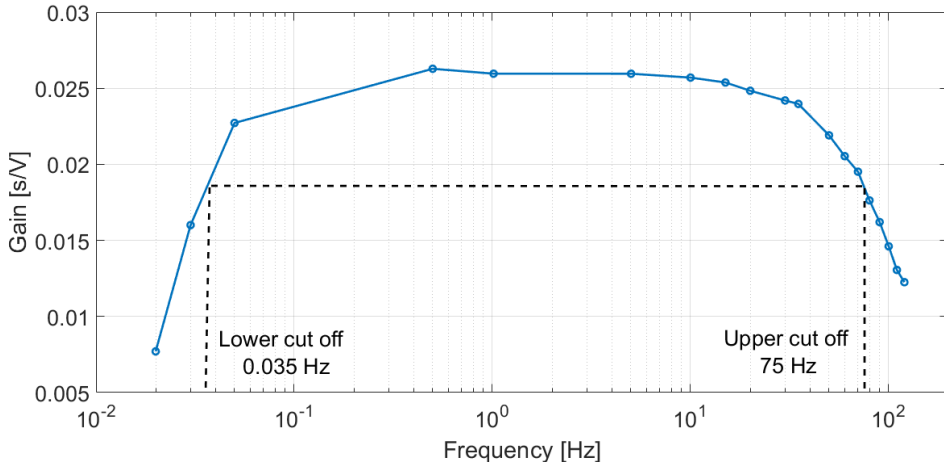


**Figure 6.13:** Measured transfer function of the full system.

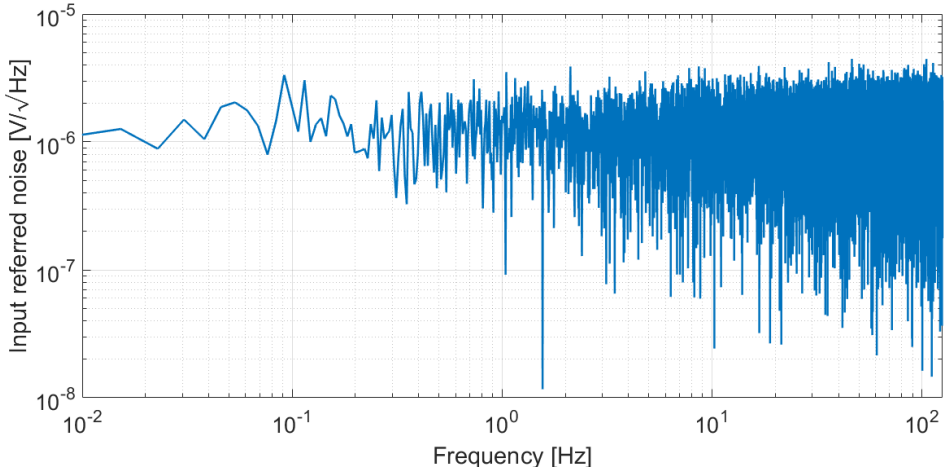


**Figure 6.14:** Measured input referred noise of the full system.

with previous state-of-the-art systems in flexible technologies. In [1, 2, 3, 4] digital signal processing is not performed on the chip. [5] has digital signal processing on flexible foil which increases the overall power dissipation of the system. Moreover, [5] presents a single channel system which does not fully leverage the large area character of flexible technologies. In [1], external discrete components are used to realize the HPF and the power dissipation of the flexible system is higher than other works. The system presented in [2] has still a large power consumption, needed to provide high input impedance. The system in [3], provides a rather low input

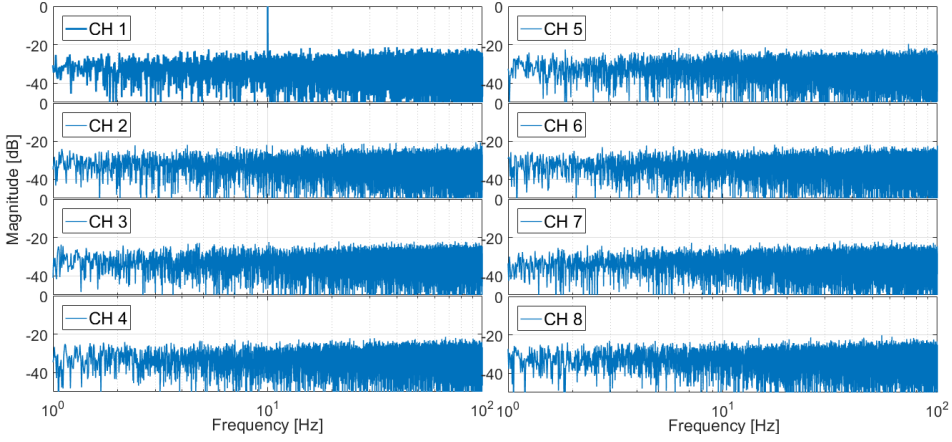


**Figure 6.15:** Measured crosstalk of the full system.

impedance, which can cause problems when using actual electrodes to capture signals. In our system, the frontend on flexible foil is integrated with a minimum number of interconnections with a Si IC for backend computation, which results in low cost, enhanced user comfort, better computational capability and low power dissipation.

## 6.4 Conclusions

We demonstrate a fully integrated 8 channel FHE EOG acquisition system fabricated in a-IGZO technology, interfaced with a custom Si IC used for backend operations. In this way the low cost, flexible form factor and large area character of the flexible TFT technology are leveraged, while exploiting at the same time the complex computational capabilities of Si ICs with low power dissipation. A tunable hybrid HPF has been integrated in the system which is used to block DC electrode offset and results in low high-pass cut-off frequency. The EOG signals can be acquired from multiple channels using time division multiplexing. The acquired signals are converted to PWM using a reset integrator which is interfaced to a Si IC in the current domain. The current domain interface enables the functionality of the full system, where both the subsystems use very different supply voltages. The

custom Si IC is used to quantize the PWM and provide output as a serial digital output bit stream. The use of a custom Si IC reduces total system power considerably compared to previously published flexible counterparts.

**Table 6.1:** Comparison with the state-of-the-art

	[1]	[2]	[3]	[4]	[5]	EOG Acquisition System
Technology	a-Si	a-IGZO	DNTT	a-IGZO	a-IGZO	a-IGZO + 180 nm CMOS Hybrid High Pass Filter
Architecture	Chopped Amplifier	Chopped Amplifier with Frequency Division Multiplexing	Amplifier with AC Coupled Load	Amplifier with Diode Connected Load	Chopped Amplifier + Low Pass Filter + Reset Integrator + DSP on foil	+ Chopped Amplifier + Low Pass Filter + Multiplexer + Reset Integrator + DSP using Si IC
Integrated DSP	No	No	No	No	Yes (DSP on foil)	Yes (DSP on Si IC)
Output Type	Analogue	Analogue	Analogue	Analogue	Digital	Digital
Number of Channels	7	4 x 4	8 x 8 (16 Amplifiers in sharing)	16 (Single Ended)	1	8
Application	EEG	EMG	EMG	EMG	ECG	EOG
Chopping Frequency [kHz]	5	5	-	-	1	1
Integrated Noise [ $\mu V_{rms}$ ](BW)	2.3 (100 Hz)	125 (500 Hz)	-	-	8 (100 Hz)	6.45 (30 Hz)
CMRR [dB]	<50 @ 50 Hz	-	-	-	67.4 @ 50 Hz	70.6 @ 30 Hz
PSRR [dB]	-	-	-	-	58.9 @ 50 Hz	68.5 @ 30 Hz
Input Impedance [ $M\Omega$ ]	0.26	29.6	0.032 @ 100 Hz	2500 <sup>a</sup>	16.5 @ 50 Hz	17500 @ 0.035 Hz
Supply Voltage [V]	55	26	2	5	10 & 5	10 & 3.3
Power Dissipation/Channel [mW]	11	1.3	0.03	0.008	0.28 + 15.4	0.044 <sup>b</sup> + 0.040
Total Area [ $mm^2$ ]	5776	205.4	1800	900 <sup>c</sup>	24 + 99.3	602.7 + 1.44

<sup>a</sup> Capacitive impedance is given without mentioning frequency.

<sup>b</sup> Phase generation block not included.

<sup>c</sup> Estimated.

## Bibliography

- [1] T. Moy, L. Huang, W. Rieutort-Louis, C. Wu, P. Cuff, S. Wagner, J. C. Sturm, and N. Verma, "An EEG acquisition and biomarker-extraction system using low-noise amplifier and compressive-sensing circuits based on flexible, thin-film electronics," *IEEE Journal of Solid-State Circuits*, vol. 52, pp. 309–321, Jan. 2017.
- [2] C. Garripoli, S. Abdinia, J.-L. J. P. van der Steen, G. H. Gelinck, and E. Cantatore, "A fully integrated 11.2 mm<sup>2</sup> a-IGZO EMG front-end circuit on flexible substrate achieving up to 41 dB SNR and 29 M $\Omega$  input impedance," *IEEE Solid-State Circuits Letters*, vol. 1, pp. 142–145, June 2018.
- [3] H. Fuketa, K. Yoshioka, Y. Shinozuka, K. Ishida, T. Yokota, N. Matsuhisa, Y. Inoue, M. Sekino, T. Sekitani, M. Takamiya, T. Someya, and T. Sakurai, "1  $\mu$ m-thickness ultra-flexible and high electrode-density surface electromyogram measurement sheet with 2 V organic transistors for prosthetic hand control," *IEEE Transactions on Biomedical Circuits and Systems*, vol. 8, pp. 824–833, Dec. 2014.
- [4] S. Mao, J. Li, A. Guo, T. Zhao, and J. Zhang, "An active multielectrode array for collecting surface electromyogram signals using a-IGZO TFT technology on polyimide substrate," *IEEE Transactions on Electron Devices*, pp. 1–6, Apr. 2020.
- [5] M. Zulqarnain, S. Stanzione, G. Rathinavel, S. Smout, M. Willegems, K. Myny, and E. Cantatore, "A flexible ECG patch compatible with NFC RF communication," *npj Flexible Electronics*, vol. 4, pp. 1–8, July 2020.
- [6] J. G. Webster, *Medical Instrumentation: Application and Design*. New York: John Wiley & Sons, 4th ed., 2009.
- [7] A. Bulling, J. A. Ward, H. Gellersen, and G. Tröster, "Eye movement analysis for activity recognition using electrooculography," *IEEE Transactions on Pattern Analysis and Machine Intelligence*, vol. 33, pp. 741–753, Apr. 2011.
- [8] M. Vidal, J. Turner, A. Bulling, and H. Gellersen, "Wearable eye tracking for mental health monitoring," *Computer Communications*, vol. 35, pp. 1306–1311, June 2012.

- [9] G. Saavedra-Pena, H.-Y. Lai, V. Sze, and T. Heldt, "Determination of saccade latency distributions using video recordings from consumer-grade devices," in *2018 40th Annual International Conference of the IEEE Engineering in Medicine and Biology Society (EMBC)*, IEEE, July 2018.
- [10] S.-F. Liang, C.-E. Kuo, Y.-C. Lee, W.-C. Lin, Y.-C. Liu, P.-Y. Chen, F.-Y. Cherng, and F.-Z. Shaw, "Development of an EOG-based automatic sleep-monitoring eye mask," *IEEE Transactions on Instrumentation and Measurement*, vol. 64, pp. 2977–2985, Nov. 2015.
- [11] E. Iáñez, J. M. Azorin, and C. Perez-Vidal, "Using eye movement to control a computer: A design for a lightweight electro-oculogram electrode array and computer interface," *PLoS ONE*, vol. 8, p. e67099, July 2013.
- [12] P. A. Constable, , M. Bach, L. J. Frishman, B. G. Jeffrey, and A. G. Robson, "ISCEV standard for clinical electro-oculography (2017 update)," *Documenta Ophthalmologica*, vol. 134, pp. 1–9, Jan. 2017.
- [13] E. Stålberg, B. Falck, A. Gilai, J. Jabre, M. Sonoo, and K. Todnem, "Recommendations for the practice of clinical neurophysiology: Guidelines of the international federation of clinical physiology (EEG suppl 52)," Elsevier Science B.V., 1999.

# Chapter 7

## A Digitally Assisted Tunable High Pass Filter

*This Chapter presents a method to build a digitally assisted tunable high pass filter for biomedical applications. The principle is tested in simulations, using a circuit designed with unipolar  $\alpha$ -IGZO TFTs. The presented approach is useful not only for setting a sub Hz cut off frequency, but it is also shown to be effective in counteracting parameter and supply voltage variations. The method presented in this Chapter can also be applied to Silicon-based circuits.*

*The contents of this Chapter have been published in ISCAS 2020 [1] conference proceedings.*

## 7.1 Introduction

High pass filters are widely used in bio-signal acquisition systems to block electrode DC offset. The cut off frequency of these filters is typically in sub Hz range, needing large resistor and/or capacitor values that are difficult and expensive to implement in integrated circuits due to the large area required. This high-pass pole is, thus, generally implemented with pseudo-resistors [2, 3, 4, 5], that suffer from very large variations due to process, supply voltage and temperature (PVT). While temperature is not a major concern in wearables, due to the close contact with the constant-temperature human body, TFT technologies are typically characterized by large transistor variations, which make even more compelling the need for TFT parameter-insensitive solutions to implement the high-pass filter. This issue is addressed here presenting a novel idea to implement a tunable high pass filter, which ensures good robustness to process and supply variations and can be applied to a-IGZO as well as to Silicon-based circuits.

The rest of the Chapter is organized as follows: The system architecture is discussed in Section 7.2, while Section 7.3 discusses the circuit principle. Simulation results are presented in Section 7.4 and Section 7.5 concludes the Chapter.

## 7.2 System architecture

The general architecture of master-slave [6, 7, 8, 9] digitally assisted filters is shown in Figure 7.1a. The master filter is a replica of the slave filter. In this scheme a reference voltage signal  $V_{ref}$  (a sinusoid digitally synthesized locally with the help of a digital to analogue converter) is applied to the master filter. The output response of the master filter is applied to the control circuitry, which generates a control signal that is fed back to the master filter, tuning it towards the desired frequency response. The control signal is applied to the slave filter too. After some

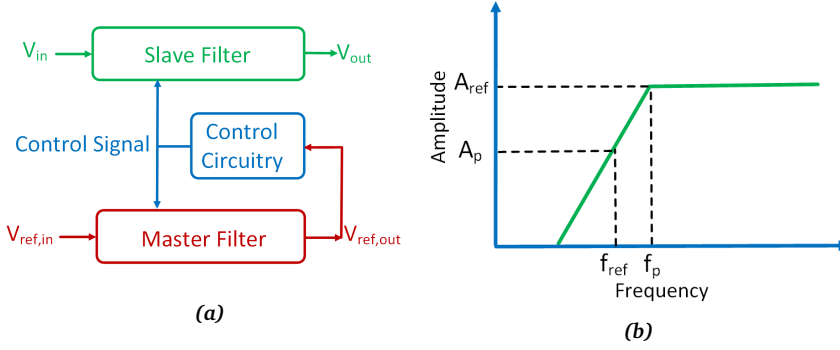


**Figure 7.1:** (a) General system architecture and (b) General high pass filter response.

iterations, the loop locks to the desired tuning point. Once the loop has stabilized, the control circuitry and the reference generator can be turned off to save power and avoid any digital switching on the foil, minimizing interference. However, this part of the system can be turned on periodically to recalibrate the slave filter. One of the factors which affects accuracy in this approach is matching between master and slave filters. Nevertheless, layout matching techniques can be used to mitigate this problem.

### 7.3 Circuit principle

The approach proposed in this Chapter exploits the attenuation that a reference sinusoidal signal experiences when its frequency is lower than the cut off of a high pass filter. If a sinusoidal signal,  $V_{ref}$ , with amplitude  $A_{ref}$  and frequency  $f_{ref}$  is applied to a first-order high pass filter, having a cut off frequency  $f_p$  higher than  $f_{ref}$ , then (as shown in Figure 7.1b) the attenuated filter output amplitude  $A_p$  and the passband frequency  $f_p$  are related by the expression:

$$f_p = \frac{f_{ref} A_{ref}}{A_p} \quad (7.1)$$

which is valid as long as  $f_{ref} \ll f_p$  (and  $A_p \ll A_{ref}$ ). In this way, for a given amplitude  $A_{ref}$  and frequency  $f_{ref}$ , monitoring the attenuated signal,  $A_p$ , at the output of the high pass filter can be used to tune the high pass filter for a desired passband frequency  $f_p$ .

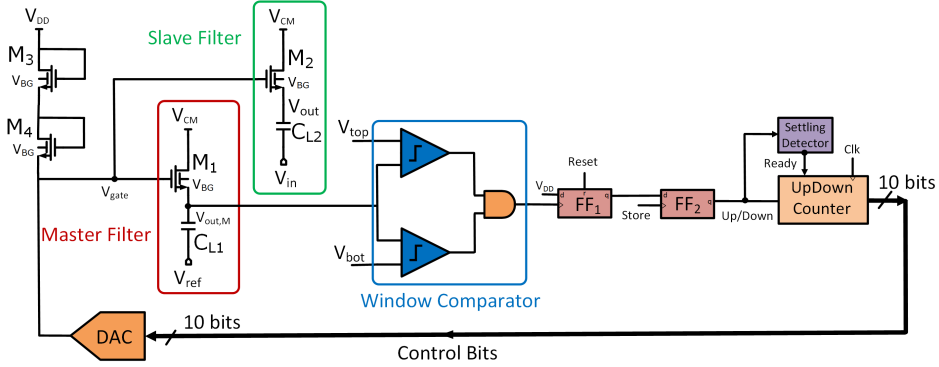


**Figure 7.2:** Circuit schematic of the proposed system.

A high-level circuit schematic of the proposed approach is shown in Figure 7.2, while Figure 7.3 shows the voltage waveforms at the most relevant nodes. The master filter consists of TFT  $M_1$  and capacitor  $C_{L1}$ , while the slave filter consists of TFT  $M_2$  and capacitor  $C_{L2}$ . Both TFTs are driven in deep subthreshold to implement very large small-signal equivalent resistances in the linear regime. The input of the master filter is fed with a sinusoidal signal having frequency  $f_{ref}$  and amplitude  $A_{ref}$ . The attenuated output of the master filter ( $V_{out,M}$ ) is monitored by a window comparator (having  $V_{top}$  and  $V_{bot}$  as the upper and lower threshold for the window, so that  $V_{top} - V_{bot} = 2 \times A_p$ ). A Reset signal consisting of short pulses at frequency equal to half  $f_{ref}$  is generated, so that the flip-flop  $FF_1$  observes the output of the window comparator for about two periods of the input sinusoidal signal. If the output filter amplitude exceeds the target size  $A_p$  during this time  $FF_1$  is set, otherwise it remains reset. The state of  $FF_1$  is stored in  $FF_2$  just before resetting the first flip-flop. The output of  $FF_2$  (Up/Down) controls the counting direction of a 10 bit up/down counter, which generates control bits for the current-domain digital

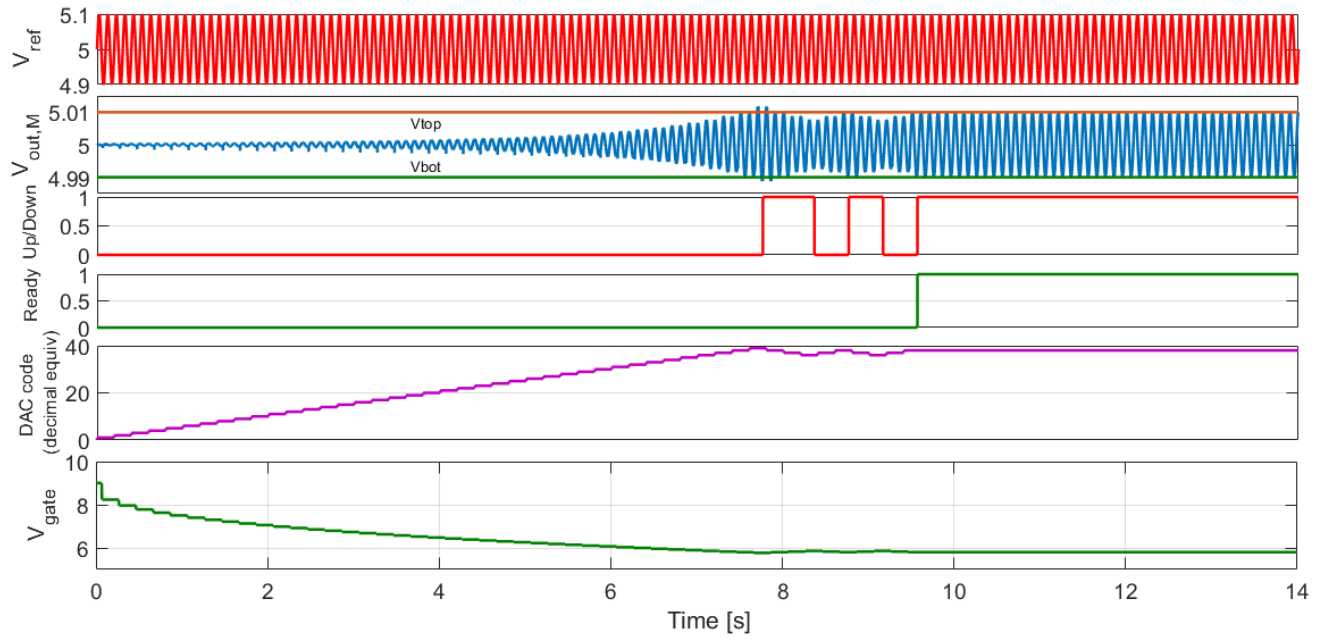


**Figure 7.3:** Waveforms at different nodes of the system depicting operation of the system. To show more clearly how the system works, an 8 bit counter and DAC are used to generate this figure.

to analog converter (DAC). If  $FF_2$  is in reset state the counter goes up, otherwise it counts down. The output current of the DAC flows in the diode connected TFTs  $M_3$  and  $M_4$ , controlling the gate biasing of the transistors  $M_1$  and  $M_2$  to achieve the desired passband frequency of the filter and the target attenuated amplitude  $A_p$ . After convergence of the feedback loop, the system would continue toggling the amplitude of the master filter output around the value of  $A_p$  determined by the threshold voltages of the window comparator. This is not needed, thus a settling detector can be used to monitor the settling behaviour of the loop. Once the output of  $FF_2$  has toggled a certain number of times, the filter bias point has settled to the desired value, and a ready flag can be generated (Ready) to freeze the counter and the DAC output to the target code value. At this instant the DAC code can be preserved in a register, while the controlling circuitry and the reference generator could be turned off to reduce power dissipation.

The design Equation 7.1 can be further modified by incorporating scaling factors between the master and slave filters as shown below:

$$f_p = \frac{f_{ref} A_{ref}}{n_1 n_2 A_p} \quad (7.2)$$

where,  $n_1 = \frac{C_{L2}}{C_{L1}}$  and  $n_2 = \frac{(W/L)_{M1}}{(W/L)_{M2}}$ .

Hence, a wide tuning range of  $f_p$  can be achieved by appropriately choosing the parameters shown in Equation 7.2.

## 7.4 Simulation results

The system is simulated using models of the a-IGZO TFTs provided by the TFT foundry for the filters and the DAC, together with behavioural models of the other building blocks in the control circuitry. To show a proof of the concept introduced in the previous section, a high pass filter for a passband frequency of 0.5 Hz has been designed. The optimized design parameters are  $f_{ref} = 10$  Hz,  $n_1 = 10$ ,  $n_2 = 20$  and  $A_{ref}/A_p = 10$ . One of the most variable parameters in TFT circuit design

is the threshold voltage,  $V_T$ . The threshold voltage varies from wafer to wafer and also changes with TFT bias stress or aging. If no tuning scheme would be applied, the sensitivity to threshold variations in the proposed filter circuit would be especially strong, as the transistors  $M_1$  and  $M_2$  are driven in subthreshold to realize large time constants.

Figure 7.4 shows the relative error in passband frequency obtained from sim-

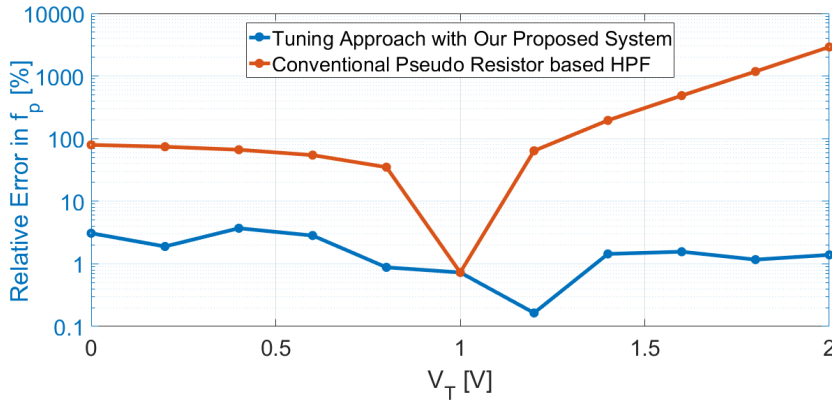


**Figure 7.4:** The effect of threshold voltage variation on the relative error in  $f_p$ .

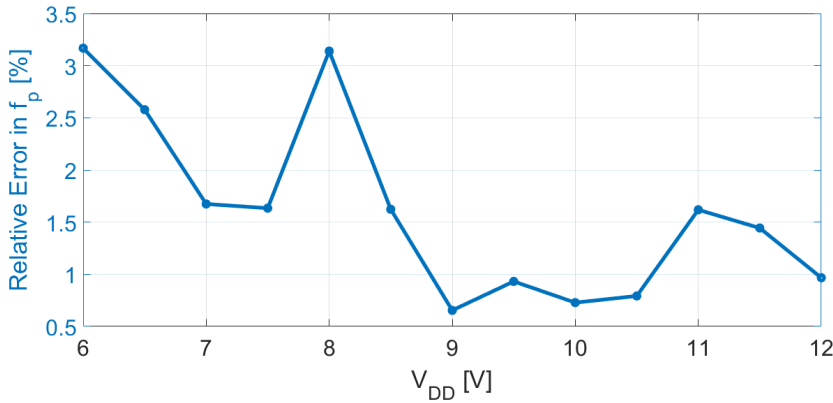


**Figure 7.5:** The effect of  $V_{DD}$  variation on the relative error in  $f_p$ .

ulations with respect to the value obtained from Equation 7.2, when varying  $V_T$  by 2 V and using the proposed tuning approach. Results are also compared to a conventional high pass filter based on pseudo-resistors. It can be seen that the rel-

active error in the realized passband frequency using the proposed tuning scheme is within 4%, while the error is very large for the conventional pseudo-resistor approach. Figure 7.5 shows the effect of  $V_{DD}$  variation on the relative error in  $f_p$ . It can be seen from the plot that  $f_p$  remains within 3.5% of its theoretical value for a  $V_{DD}$  variation as large as 6 V, confirming a good robustness of the proposed approach to supply voltage variations. Figure 7.6 shows the behaviour of  $f_p$  and of the relative error in  $f_p$  when changing  $f_{ref}$  from 1 Hz to 100 Hz. It can be seen from the plot that a tuning range of  $f_p$  spanning two decades from 0.05 Hz to 5 Hz can be achieved while keeping a maximum 1% relative error. Figure 7.7 shows the effect of  $A_{ref}/A_p$  ratio variation on  $f_p$  and the relative error in  $f_p$ . It can be observed that the relative error in  $f_p$  remains less than 3% for a wide range of  $A_{ref}/A_p$  ratios. Figure 7.8 shows the relative error in  $f_p$  when varying  $A_p$  while keeping  $A_{ref}/A_p = 10$ , to maintain the target passband frequency constant. It can be seen from the plot that the relative error in passband frequency increases linearly in a staircase pattern and remains less than 5% till 30 mV  $A_p$  amplitude, when the input reference amplitude is thus 300 mV. The fact that input signals of several hundreds of millivolt can still be tolerated shows the robustness of the proposed approach for the application to input filters (where typical signal amplitudes are small).

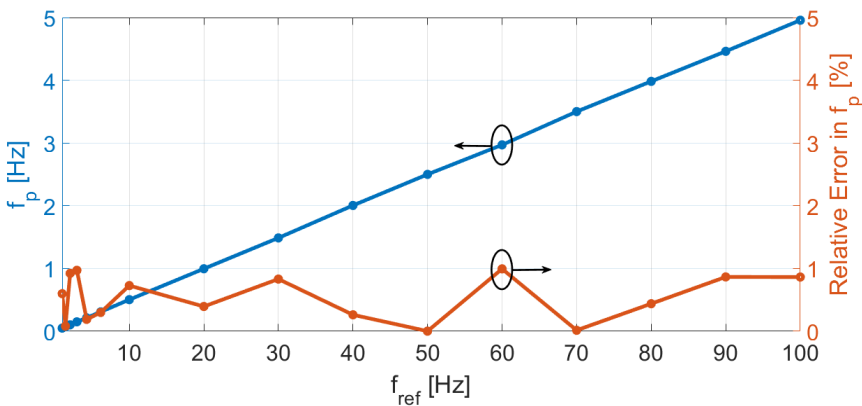


**Figure 7.6:** The effect of  $f_{ref}$  variation on  $f_p$  and the relative error in  $f_p$ .

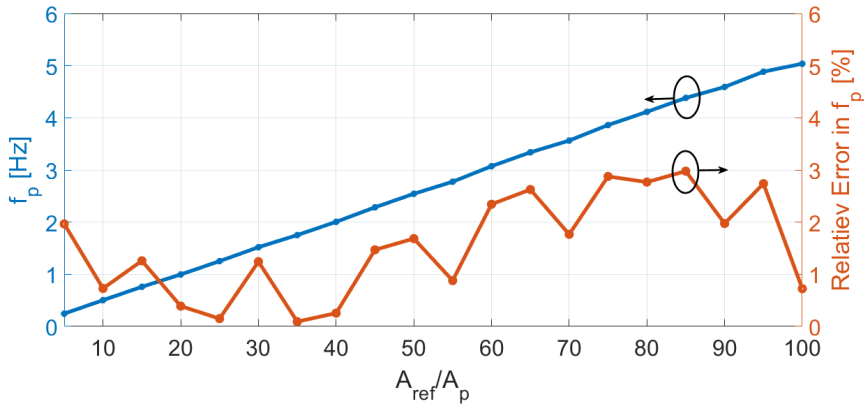


**Figure 7.7:** The effect of  $A_{ref}/A_p$  ratio variation on  $f_p$  and the relative error in  $f_p$ .

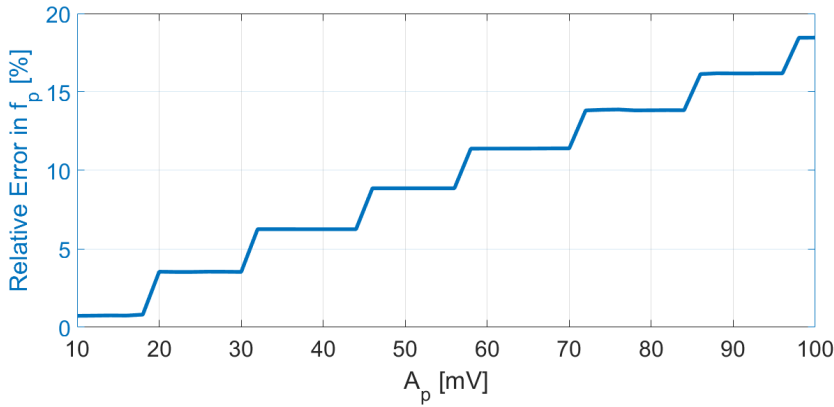


**Figure 7.8:** The effect of  $A_p$  variation in  $f_p$  (keeping the  $A_{ref}/A_p$  ratio constant).

It can be observed that the relative error in  $f_p$  is limited by the finite resolution of the DAC, the loop settling and matching of the master and slave filters. The inaccuracy in  $f_p$  caused by mismatch and scaling of the master and slave filters can be minimised by unary element layout.

## 7.5 Conclusions

A method to build a digitally assisted tunable high pass filter for biomedical applications is discussed in this Chapter, and is simulated using unipolar a-IGZO TFTs. The presented system leverages the signal attenuation by the high pass filter when

a reference sinusoidal signal with a frequency lower than the cut off frequency is applied, to tune a master-slave filter structure. The results presented in this Chapter show that sub Hz cut off frequencies can be obtained with less than 5% relative error in presence of large TFT parameter and supply variations. The proposed tuning scheme can be applied to improve the precision of high pass filters for biomedical applications implemented in a-IGZO and also in Silicon.

## Bibliography

- [1] M. Zulqarnain, S. Stanzione, and E. Cantatore, "A Digitally Assisted Tunable High Pass Filter Based on Flexible a-IGZO TFTs for Biomedical Applications," in *2020 IEEE International Symposium on Circuits and Systems*, pp. 1–5, IEEE, 2020.
- [2] A. Tajalli, Y. Leblebici, and E. Brauer, "Implementing ultra-high-value floating tunable CMOS resistors," *Electronics Letters*, vol. 44, no. 5, pp. 349–350, 2008.
- [3] M.-T. Shiue, K.-W. Yao, and C.-S. Gong, "Tunable high resistance voltage-controlled pseudo-resistor with wide input voltage swing capability," *Electronics Letters*, vol. 47, no. 6, pp. 377–378, 2011.
- [4] H. Kassiri, K. Abdelhalim, and R. Genov, "Low-distortion super-GOhm subthreshold-MOS resistors for CMOS neural amplifiers," in *2013 IEEE Biomedical Circuits and Systems Conference (BioCAS)*, pp. 270–273, IEEE, Oct. 2013.
- [5] R. Puddu, C. Carboni, L. Bioni, G. Barabino, D. Pani, L. Raffo, and M. Barbaro, "A precision pseudo resistor bias scheme for the design of very large time constant filters," *IEEE Transactions on Circuits and Systems II: Express Briefs*, vol. 64, pp. 762–766, July 2017.
- [6] Y. Tsvividis, "Self-tuned filters," *Electronics Letters*, vol. 17, no. 12, p. 406, 1981.
- [7] R. Schaumann and M. Tan, "The problem of on-chip automatic tuning in continuous-time integrated filters," in *IEEE International Symposium on Circuits and Systems*, pp. 106–109 vol.1, IEEE, 1989.
- [8] J. Silva-Martinez, M. Steyaert, and W. Sansen, "A novel approach for the automatic tuning of continuous time filters," in *IEEE International Symposium on Circuits and Systems*, pp. 1452–1455 vol.3, IEEE, 1991.
- [9] J. Osa, A. Carlosena, and A. Lopez-Martin, "MOSFET-C filter with on-chip tuning and wide programming range," *IEEE Transactions on Circuits and Systems II: Analog and Digital Signal Processing*, vol. 48, no. 10, pp. 944–951, 2001.



# Chapter 8

## Conclusions

## 8.1 Conclusions

This dissertation illustrates various circuit design and system level solutions to enable bio-signal monitoring on a flexible foil. The results presented in this thesis are the first steps towards building a low cost health patch with flexible electronics capable of monitoring vital signs.

After an introduction to a-IGZO TFT technology in Chapter 2, in Chapter 3, the key design trade-offs in bio-signal front-end architectures that are especially relevant to a-IGZO TFT circuits, are discussed. The diode-connected load amplifiers with cascaded stages offer a good compromise of performance and robustness. For this reason, they have been chosen as preamplifiers for the system architectures presented in this thesis.

Chapter 4 presents a voltage to pulse width conversion technique using a reset integrator with a switched capacitor load. This technique is especially suitable for unipolar technologies which do not offer complementary loads. Additionally, the input is transformed to the time domain which paves the way to a radically different analogue to digital conversion approach. The analogue to digital conversion for bio-signal acquisition systems is performed in two steps. In the first step, as presented in Chapter 4, the input signal is transformed to a binary pulse width modulated (PWM) representation, using a time based reset integrator. In the second step, the output PWM is quantised in time to get a digital representation (discussed in Chapter 5). The proposed technique is utilised to realize a time based heart-rate measurement interface, that requires a moderate SNR. The presented solution is compact, low cost and adds to user comfort, thanks to its mechanical flexibility. However, this approach achieves an SNR that is insufficient for most biomedical monitoring applications. It has been shown that SNR could be improved by applying CDS at system level to enable applications that are more demanding in terms of SNR, e.g. ECG monitoring. It can be concluded that the transformation of an input signal from the voltage domain to the time domain in a simple, minimalistic and energy efficient manner opens an arena of opportunities

in unipolar technologies, where high gain amplifiers are not easily available.

In Chapter 5, we present the fundamental steps to demonstrate intelligent plasters for biomedical applications based on flexible electronics which are compatible with the NFC standard. The presented approach provides a digitization strategy using a time reference, without the need for a voltage reference, and thus is particularly suited to implementation with a-IGZO TFTs on foil. The output is transformed to the digital domain and provided as a 105.9 kb/s Manchester encoded serial bit stream. To the best of author's knowledge, this is the first demonstrated ECG acquisition system in flexible a-IGZO TFTs on foil providing a digital serial output bit stream compatible with the NFC standard. The circuit improvements (e.g. implementation of anti-aliasing filtering before the reset integrator) and better TFT technology used for this design (the DUGA technology which is faster and has better  $1/f$  noise performance), results in the best NEF and PEF values reported in literature for a-IGZO TFT circuits to date.

In the context of the reset integrator, which has been the core circuit block used in this thesis, the following conclusions can be drawn:

- The single slope integrator is optimal in terms of gain but not linearity. Linearity can be improved by adding a constant current discharge phase that improves linearity at the cost of gain.
- The voltage to time conversion gain of a single reset integrator is not sufficient to use in practical applications. Hence, a gain stage is required in front of the reset integrator.
- In order to reduce noise folding, a low pass filter acting as an anti aliasing filter should be used in front of the reset integrator.

In Chapter 6, a multichannel hybrid flexible electronics system for EOG application is presented. The system, consisting of a multichannel frontend acquisition system based on a-IGZO TFTs manufactured on flexible substrate, is interfaced

with a Silicon-based custom IC for digitization of the acquired signal. In this way, low cost, flexible form factor and the large area character of the flexible technology are leveraged, while exploiting at the same time the complex computational capabilities and low power dissipation of Silicon ICs. The system is designed in a novel way to reduce the number of interconnects from the flexible system to the Silicon IC. A tunable hybrid HPF has been integrated in the system which is used to block DC electrode offset and results in low high-pass corner frequency. The use of a custom Si IC reduces the total system power considerably considering flexible counterparts.

In Chapter 7, a digitally assisted tunable high pass filter for biomedical applications is presented. We can conclude from the presented results that sub Hz cut off frequencies can be obtained with good accuracy in presence of large TFT parameter and supply variations. The proposed tuning scheme can be applied to improve the precision of high pass filters for biomedical applications implemented in a-IGZO and also in Silicon.

## 8.2 Future work

From the circuit design perspective, many innovations could be added to the core reset integrator circuit e.g. instead of adding a voltage gain stage in front of the reset integrator, a time domain gain stage can be added, which will result in energy efficient and completely time domain operation of the circuit.

From the technology perspective, DUGA a-IGZO TFT technology appears to be a promising solution to implement a wearable bio-signal acquisition system. However, scaling of the feature size would be required to not only reduce circuit footprint, but also to increase the transition frequency of the TFTs. Moreover, advancements of the technology process will be required to push the performance of the TFTs in terms of transconductance and  $1/f$  noise.

Although the models presented in Chapter 2 describe the TFT behaviour quite

well, a more sophisticated model is required to incorporate variability, mismatch and other second order effects such as a better description of the dynamic behavior, to design complex variability-insensitive circuits and systems.

The availability of a Process Design Kit (PDK), in order to design complex systems on foil is of uttermost importance. However, Electronic Design Automation (EDA) tools for flexible technologies are still in their nascent phase. Hence, in order to enable the design of complex systems on foil, a PDK specifically developed for flexible technologies is required.



## Summary

### **Integrated Circuits for Wearable Systems based on Flexible Electronics**

Electronics has witnessed a transformation in recent years, due to the rapid rise of wearables and ubiquitous sensors, fostering the advent of Internet of Things (IoT). There are applications which are not trivial to be implemented by traditional electronics such as displays, imagers, photovoltaic cells, near field communication (NFC) tags, wearable sensors for biomedical signals monitoring etc. These applications require a large surface to be covered with electronics and are difficult or costly to achieve with the conventional Silicon-based Integrated Circuits (ICs). However, advancements in the technology process of thin-film transistors (TFTs) have paved the way to fabricate devices over large areas and have opened the possibility to use plastic foils to provide mechanically flexible substrates. This type of devices not only result in electronics distributed over a large area, but also leads to lower cost per unit area compared to conventional ICs. The inherent flexible nature of the substrates has been leveraged in applications requiring conformability, bendability, foldability and stretchability. A specific category of applications that can strongly benefit from the flexible electronics is the domain of flexible and comfortable wearable devices for wellness and healthcare monitoring.

The aim of this thesis is to advance the state-of-the-art of flexible electronics with specific focus on wearable bio-signal measurement systems. A bottom-up design approach is used to design wearable bio-signal interfaces.

After an introduction to a-IGZO TFT technology in Chapter 2, in Chapter 3, we demonstrated the design of single stage and multi-stage amplifiers with different topologies to get an insight into performance trade-offs and maximum gain architecture in unipolar flexible technologies.

Moving up in the design approach, we present a novel voltage to pulse width conversion technique using a reset integrator with a switched capacitor load, exploiting a simple and power minimalistic implementation. This technique is especially advantageous in unipolar technologies, which do not offer complementary loads. Additionally, the signal can be easily transformed to a binary pulse width modulated (PWM) representation, paving the way to a radically different analogue to digital conversion (ADC) approach. Indeed, to perform ADC, the PWM signal is simply quantized in time and transformed to a digital word using a counter. The transformation of the input signal from voltage to time domain in a simple, minimalistic and energy efficient way enables a wide spectrum of opportunities in unipolar technologies, where high gain amplifiers cannot be easily implemented.

This proposed technique is used first to realize a time-based heart-rate measurement interface, presented in Chapter 4. Then, it has been shown that the signal to noise ratio (SNR) can be improved by applying correlated double sampling at system level, enabling applications that are more demanding in terms of SNR.

In Chapter 5, we report on a flexible electrocardiogram (ECG) sensor which exploits TFT-based circuits on flexible foil and the reset integrator approach to implement the full chain of signal acquisition, amplification and digitization and is capable to measure ECG signals for the first time on foil (to the best of the author's knowledge). The presented approach provides digitization using a time reference, with no need for a voltage reference, and thus, is particularly suited to implementation with a-IGZO TFTs in the framework of an NFC system, where a precise clock can be generated based on the received carrier. Additionally, a 105.9 kb/s Manchester encoded bit stream compatible with the NFC standard is generated at the output.

Further, Chapter 6 presents a multichannel EOG acquisition system based on flexible TFTs and CMOS technologies. The system, consisting of a frontend acquisition system based on a-IGZO TFTs manufactured on flexible substrate, is interfaced with a Silicon based custom IC for digitization of the acquired signal. In this way the low cost, flexible form factor and the large area character of flexible TFT technology are leveraged, while utilising at the same time the complex computational capabilities and low power dissipation of Silicon ICs. The system is designed in a novel way to reduce the number of interconnects from the flexible system to the Silicon IC. A tunable hybrid HPF has been integrated in the system which is used to block DC electrode offset and results in low high-pass corner frequency. The use of a custom Si IC reduces the total system power considerably compared to flexible counterparts.

Chapter 7 presents a digitally assisted tunable high pass filter for biomedical applications. HPFs are widely used in bio-signal acquisition systems to block electrode DC offset. The cut off frequency of these filters is typically in sub Hz range, needing large resistor and/or capacitor values that are difficult and expensive to implement in integrated circuits due to the large area required. The proposed architecture provides a solution to this issue. It is shown that accurate sub Hz cut off frequencies can be obtained in presence of large TFT parameter and supply variations. The proposed tuning scheme can be applied to improve the precision of high pass filters for biomedical applications implemented both in a-IGZO and in Silicon.



## List of publications

- (1) M. Zulqarnain, S. Stanzione, J.-L. P. J. van der Steen, G. H. Gelinck, K. Myny, S. Abdinia, and E. Cantatore, "A 52  $\mu$ W heart-rate measurement interface fabricated on a flexible foil with a-IGZO TFTs," in 2018 - 44th European Solid State Circuits Conference (ESSCIRC), pp. 222–225, IEEE, Sept. 2018.
- (2) M. Zulqarnain, S. Stanzione, J.-L. P. J. van der Steen, G. H. Gelinck, S. Abdinia, and E. Cantatore, "Design trade-offs in amorphous indium gallium zinc oxide thin film transistor based bio-signal sensing front-ends," *Flexible and Printed Electronics*, vol. 4, pp. 014001, Jan. 2019.
- (3) M. Zulqarnain, S. Stanzione, J.-L. P. J. van der Steen, G. H. Gelinck, K. Myny, and E. Cantatore, "A low power time domain ECG interface based on flexible a-IGZO TFTs," in 2019 IEEE 8th International Workshop on Advances in Sensors and Interfaces (IWASI), pp. 205–209, IEEE, June 2019.
- (4) M. Zulqarnain, S. Stanzione, G. Rathinavel, S. Smout, M. Willegems, K. Myny, and E. Cantatore, "A flexible ECG patch compatible with NFC RF communication," *npj Flexible Electronics*, vol. 4, pp. 1–8, July 2020.
- (5) M. Zulqarnain, S. Stanzione, and E. Cantatore, "A Digitally Assisted Tunable High Pass Filter Based on Flexible a-IGZO TFTs for Biomedical Applications", in 2020 IEEE International Symposium on Circuits and Systems (ISCAS), pp. 1-5, IEEE, Oct. 2020.
- (6) M. Zulqarnain, S. Stanzione, F. Tankut, K. Myny, P. Harpe, and E. Cantatore, "A Multichannel EOG Acquisition System based on flexible TFTs and CMOS technologies," manuscript in preparation.



---

## Acknowledgments

*They say the important thing in life isn't the destination, it's the journey. . .*

*The challenges you face along the way. . .*

*The unexpected twists and turns. . .*

*The disappointments you overcome. . .*

— *Modern Family* S3:E21

. . . So, here it goes. One of the finest journeys of my life comes to an end. During the last five years, I have had the opportunity to work with some of the smartest people around. Each of them has taught me something new, either directly or indirectly. This thesis would be incomplete without an expression of deep gratitude towards these people and others who have helped and supported me during the brightest and the darkest times. I would like to acknowledge as many of them as I can in the following paragraphs.

First and the foremost, I would like to thank Eugenio, my promotor, for his extremely valuable guidance and continuous support throughout my PhD. Dear Eugenio, it has been a pleasure working under your supervision. Over the last five years, I have matured both as a researcher and as a person, a big thanks to you. You have been my best critic and ultimately my biggest supporter. I learned a great deal from you, both at professional and personal level. You are a constant source of motivation and inspiration to me. I admire your passion for scientific research and your attention to detail. I truly appreciate your quality of leading by example. You have an elusive ability to relate information and experiences from disparate situations to solve issues and boil them down to simple insights everyone can understand. When things were not going right initially, which is the case with most of the PhDs in emerging technologies, you provided me your full support and motivation and showed the path of perseverance, which ultimately paid off. I learned from you not only the art of circuit design but also the art of technical writing. Your feedback greatly improved the quality of my research, be it

our papers or this thesis. Time and again, your advice and suggestions have helped me through tricky situations. I hope that they will continue to inspire me to do my best in my future endeavours. Thank you very much, for being an ideal, reasonable and friendly mentor, which one could imagine for.

Dear Stefano, it was a pleasure for me to have a mentor like you. You guided me through the process of what circuit design is all about, not found in books, in a very friendly and interactive manner, which improved my understanding of circuits, manifolds. I truly enjoyed all those long discussions, where genesis of many ideas presented in this thesis took place. Whenever I was stuck somewhere, whether it was circuit design or building measurement setup, you were always there to help, which made my life a lot easier. Many a times, I called you on your office phone or even on your mobile, to discuss issues arising in the lab during measurements, you used to listen to my long queries calmly and always suggested solutions that would work. You even came to TU/e many times to help in measurements. Thank you for your support. Your feedback and comments greatly improved the quality of this research. You not only provided me with a lot of valuable guidance on my research, but also gave me idea about fruitful communication in an organizational structure. I sincerely thank you for your guidance and help to make this journey memorable.

Dear Kris, thank you for your guidance and support in this project. I learned a lot from you. I am thankful to you for all the interesting brainstorming sessions about the technology, for your help during and after tape-outs and for your help in on-foil digital design presented in this thesis. Our collaboration has been incredibly fruitful and we will hopefully continue to collaborate in the years to come. I totally enjoyed my time in imec Leuven, where you also joined for measurements. I am truly thankful to you for your dedication and commitment, when you decided to perform measurements, due to an approaching deadline, instead of going with group members on a scheduled outing. It ultimately resulted in our Nature paper. Thank you for your wonderful efforts, guidance and support.

I am very grateful to the members of the doctoral committee, Prof. Genoe, Prof. Dehaene and Prof. Mischi for careful reading of the dissertation. Thanks to Prof. Heemstra de Groot for chairing the committee.

Dear Sahel, thank you for your guidance and support during mid part of my project. I thoroughly enjoyed working with you. Although you were not associated with my project for the entire duration, but your suggestions, advices and help were very crucial, needful and beneficial at that phase of my PhD. I totally enjoyed all the technical and non technical discussions, which we had. Thank you for your help and support.

Dear Pieter, I am thankful for all the useful discussions that we had over the years. Thank you for your help during measurements and FPGA programming. You took the time to read my thesis quite thoroughly, for which, I am very grateful. I also thank you for all your comments that have further helped me to improve the quality of my work.

Dear Marco (Fattori), we had a lot of pleasant and fruitful, technical and non technical discussions. I enjoyed them all. Thank you for your help in lab during measurements and PCB soldering. Thank you for reading my thesis and helping me to improve my work with your valuable and insightful comments.

I would also like to thank Prof. Mohd. Hasan from my previous lab at AMU, for developing my initial interest in analogue circuit design. I am thankful for his motivation and support, which opened the world to me. I am thankful to Dr. Ajmal Kafeel as well, with whom I started the journey of academic research. His valuable suggestions helped me to understand the basics of scientific writing.

I would like to thank all my colleagues and friends at the IC group for helping me out in many ways. Several colleagues shared office with me during these five years and created a friendly multicultural environment. Dear Bindi, Maoqianq, Zhe, Kuangyuan, Debashis, Wilfried, Pavlos, Marios, Yuting, Hanyue, Bas and Daan, thank you all for your wonderful company. Dear Carmine, thank you for all the discussions about this technology and help in the measurements in initial

days of my PhD. Dear Debashis (Dhar), we had many amazing euro trips, which became memorable. Especially, our Swiss and black forest trips were magnificently surreal, where we could admire the picturesque landscape of Europe. Thank you for being a fantastic travel buddy. Dear Debasish (Mitra), we had many friendly conversations over the last few years, I really enjoyed them. Dear Wilfried, it was a pleasure for me to share office with you not only in TU/e but in Holst Centre as well. Thank you for your help in matlab codes. I also would like to thank the rest of the group, starting from the former chair, Arthur van Roermund, to the current chair, Peter Baltus, and also all the staff members. Dear Rainier, thank you very much for your help and support in lab and other technical issues. Thank you dear Margot, for your prompt support in all administrative matters.

My thank also goes to the colleagues of the Holst Centre for all the amazing discussions. I would like to thank Samira, Richard, Chris, Roland, Salvatore, Hyunsoo, Jiawei, Najat, Nick, Rik and Mario for their support and help. While in Holst Centre, I shared office with Ganesh and Marco. Dear Ganesh, it was really nice to have amazing discussions with you related to professional and personal life. We had many amazing trips including our official Leuven trips and trip to Berlin and Prague. I enjoyed them all. Dear Marco (Mercuri), it was indeed a lively environment with you. Although we were office mates for a short period only, but I totally enjoyed it. Your intentional interruptions in discussions with Stefano would induce liveliness in the room and made the environment much more pleasant. Thank you for those lovely memories. Among the other people I have worked with, I would like to thank the design team from LAE group at imec, for their help in on-foil digital design. I am thankful to Nikolas and Olivier as well, for their help related to technology in DUGA tape-outs. I would like to thank Jan-Laurens for providing area, help and support in ESL technology.

I have been very fortunate to receive the kindness, friendship and help of many amazing people from the time I arrived in the Netherlands, and I would like to thank them all. Dear Vikas, you had been a perfect neighbour. Be it the Indian

political arena in the time of a paradigm shift or the latest trends in memes or the insurmountable difficulty of being a PhD scholar, we literally had discussions on all the topics and I enjoyed all those conversations to the fullest. Thank you for all those memories of Hemelrijken. Dear Zaid, we became close friends in a very short time, probably due to the fact that our roots originate from the same place. We have had many amazing discussions on as diverse topics as possible. We have talked about Sartre to Seneca, telescopes to constellations, aurora borealis to Van Allen belts, guitars to mouth organs, functioning of mosfets to aerodynamics of A380, cricket to basketball, bollywood to hollywood, psychology to gastroenterology, politics to religion, entrepreneurship to business acumen and the list goes on. All those discussions were very insightful and I totally enjoyed them. We had many fantastic road trips across The Netherlands, Belgium and Germany, along with Debashis. Thank you very much for the sharing of thoughts, discussions, and care. I appreciate it very much. Dear Lokesh, we spent a fantastic time in TU/e sports center. Our trip to Vienna was absolutely fantabulous. Thank you for your wonderful company.

I would like to mention all my friends from my school days, college days and later, for being always close to me, and making me feel that time has not passed. Dear Jibran, twenty years have passed since we met for the first time in City School, still it feels like we met just the day before. You are a friend on whom I can always count. Thank you for always being there, whenever I needed. We have shared the moments of successes and failures. We have seen each other grow from a school child to a matured man. With that being said, I am thankful to you, for all the memories we shared, for all the advices you gave, for everything which you have done for me and for everything which I learnt from you. I still utilize your fantastic understanding of human behavioral cues. Our friendship is continuously growing stronger, and I am so thankful for that. I am confident that there is a lot more awaiting for you, as having patience always gives you what you deserve. Dear Dr. Rafay, our friendship also started in City School two decades ago. We have shared

a lot of memories. Although, we changed our tracks when you chose medicine, but with each passing year our friendship has grown stronger. Thank you for being a wonderful friend. I would like to also thank Faizan, Aleem, Mirsab, Shadab, Obaid, Farhan, Arman, Abdullah and Asim bhai for the time we spent in AMU and specially at AMU *dhabas* (cafes). Whenever we meet even after years, it feels as if we met yesterday.

A special thank goes to my uncle Mr. Ateeq Ahmad, who has a profound impact in my life from my early childhood days. Words will never be enough to describe all that he has done for us and how appreciative I am of everything. I am extremely thankful to him. I am thankful to my grandmother (*naani*) for always keeping me in her prayers. I am thankful to all my near and dear ones for their emotional support throughout my life and especially in these years of being away from home.

Finally, I would like to express my gratitude towards my parents, to whom I owe all my achievements. I am thankful to you for what you taught me in my formative years, your unconditional support, trust and respect for my decisions. Thank you for always believing in me. You have always encouraged me to chase my dreams. I am grateful to you for all the sacrifices you have done for me. It has been five years since I left home and came here. Over the years, I have learned that 'home' is not a place, it's a feeling. Something I believe I will always have whenever I think of you and Aligarh. I am equally thankful to: my elder sister Dr. Eram, our brother-in-law Rashid bhai, our cute niece Yusra, my elder brother Khizarnain and younger brother Faisal. We share a bond that is very special. Although we are now far away from each other, but with time, the bond has grown even stronger regardless of distances. Thank you for bearing with my bizarre schedules. It was the best time of my life that we spent together that formed my ambitions. I look forward to a lot of moments of joy and memories with you all in the years to come.

## Curriculum Vitae

Mohammad Zulqarnain was born on 15-08-1990 in Aligarh, India. After finishing his senior secondary school in 2007, he enrolled in Bachelor of Technology (B.Tech) in Electronics Engineering at Zakir Husain College of Engineering and Technology, A.M.U., Aligarh. In 2015, he graduated in Master of Technology (M.Tech) with specialization in Electronic Circuits and System Design with University Medal for standing first in all branches of M.Tech. In October 2015, he started a PhD project at Eindhoven University of Technology, The Netherlands in collaboration with imec-NL/Holst Centre. The results from his research are presented in this thesis.